

REPORT DOCUMENTATION PAGE				Form Approved OMB No. 0704-0188	
<small>Public reporting burden for this collection of information is estimated to average 1 hour per response, including the time for reviewing instructions, searching data sources, gathering and maintaining the data needed, and completing and reviewing the collection of information. Send comments regarding this burden estimate or any other aspect of this collection of information, including suggestions for reducing this burden to Washington Headquarters Service, Directorate for Information Operations and Reports, 1215 Jefferson Davis Highway, Suite 1204, Arlington, VA 22202-4302, and to the Office of Management and Budget, Paperwork Reduction Project (0704-0188) Washington, DC 20503.</small>					
PLEASE DO NOT RETURN YOUR FORM TO THE ABOVE ADDRESS.					
1. REPORT DATE (DD-MM-YYYY) 02/01/2012		2. REPORT TYPE Final Report		3. DATES COVERED (From - To) 03/01/2009-11/30/2011	
4. TITLE AND SUBTITLE Snap-through and Continuation				5a. CONTRACT NUMBER	
				5b. GRANT NUMBER FA9550-09-1-0204	
				5c. PROGRAM ELEMENT NUMBER	
6. AUTHOR(S) Lawrence N. Virgin (Duke University) and Ilinca Stanciulescu (Rice University)				5d. PROJECT NUMBER	
				5e. TASK NUMBER	
				5f. WORK UNIT NUMBER	
7. PERFORMING ORGANIZATION NAME(S) AND ADDRESS(ES) Duke University (subcontract at Rice University) Dept. Mechanical Engineering, Hidson Hall, Duke Box 90300, Durham, NC 27708-0300.				8. PERFORMING ORGANIZATION REPORT NUMBER	
9. SPONSORING/MONITORING AGENCY NAME(S) AND ADDRESS(ES) Air Force Office of Scientific Research				10. SPONSOR/MONITOR'S ACRONYM(S) AFOSR	
				11. SPONSORING/MONITORING AGENCY REPORT NUMBER AFRL-OSR-VA-TR-2012-0723	
12. DISTRIBUTION AVAILABILITY STATEMENT Distribution A					
13. SUPPLEMENTARY NOTES This research was conducted in collaboration with researchers from the AFRL at WPAFB, Dayton, Ohio.					
14. ABSTRACT <p>This project has resulted in a solid improvement to the state of the art in nonlinear structural dynamics. The new insight gained, and the types of structural components analyzed, are directly applicable to the structural mechanics objectives of the US Air Force. In order to fully provide a test-bed for future hypersonics vehicular analysis (in particular) it is crucial to understand the nonlinear dynamical behavior of slender structural elements in extreme environments.</p> <p>The technical papers that form the appendices of this final report detail the achievements that have been made on both the experimental and computational fronts of this project.</p>					
15. SUBJECT TERMS Nonlinear structural dynamics, computations, experiments, snap-through boundaries					
16. SECURITY CLASSIFICATION OF:			17. LIMITATION OF ABSTRACT UU	18. NUMBER OF PAGES	19a. NAME OF RESPONSIBLE PERSON Dr. David Stargel
a. REPORT U	b. ABSTRACT U	c. THIS PAGE U			19b. TELEPHONE NUMBER (Include area code) (703) 696-6961

AFOSR Final Report: FA9550-09-1-0204

Period: 3 year total.

Name: Prof. VIRGIN

PI E-mail: L.VIRGIN@DUKE.EDU

Institution: DUKE UNIVERSITY

Business Office E-mail: SPONSOREDPROGRAMS@DUKE.EDU

Subcontract name: Prof. STANCIULESCU

Institution: RICE UNIVERSITY

Grant Title: SNAP-THROUGH AND CONTINUATION

Summary:

This project has resulted in a solid improvement to the state of the art knowledge in nonlinear structural dynamics. The new insight gained, and the types of structural components analyzed, are directly applicable to the structural mechanics objectives of the Air Force. In order to fully provide a test-bed for future hypersonics vehicular analysis (in particular) it is crucial to understand the nonlinear dynamical behavior of slender structural elements in extreme environments.

The technical papers that form the appendices of this final report detail the achievements that have been made on both the experimental and computational fronts of this project. Both PI's have spent extended periods at the AFRL in Dayton, Ohio interacting with Air Force personnel in this area (including during the summers of 2009, 2010 and 2011). A number of research assistants were supported on this project. Both PI's and the two of the graduate students spent time at AFRL in Dayton in the.

The Context of the Research:

In order to meet ever-increasing performance demands modern aircraft are being designed lighter than ever before. This weight efficiency usually comes at the expense of structural mass, leading to more slender structural components. Slender structures are however susceptible to vibration and instabilities, particularly buckling, which can occur well before strength limits are reached.

Snap-through buckling is a particular type of buckling where a structure snaps from one state to another remote state. Such large deflections pose a hazard since they can cause fatigue, and in the context of hypersonics, sonic fatigue due to boundary layer effects. Postbuckled snap-through occurs in axially loaded structures, where a structure snaps between the two (often) symmetric buckled states under some perturbation.

The two main thrusts of this research has concerned low-order experimental models, and high-order computational. Although the approaches and scale of these system approaches

are quite different, the resulting research discoveries illustrate the similarity in dynamic phenomena, and indeed, these approaches have mutually informed each other.

Summary of Experimental Results:

Figure 1(a) shows a photograph image of the experimental test-bed, built by the PI Prof. Virgin and his students at Duke University. A schematic of this system is shown in part (b). When this system is laterally excited, it is capable of exhibiting a sensitivity to initial conditions. Part (c) shows how the system can be randomly perturbed about, and between, various co-existing behaviors. That is, the system ‘snaps’ between various forms of behavior, and this of course is exactly the type of behavior that has such striking implications for sonic fatigue.

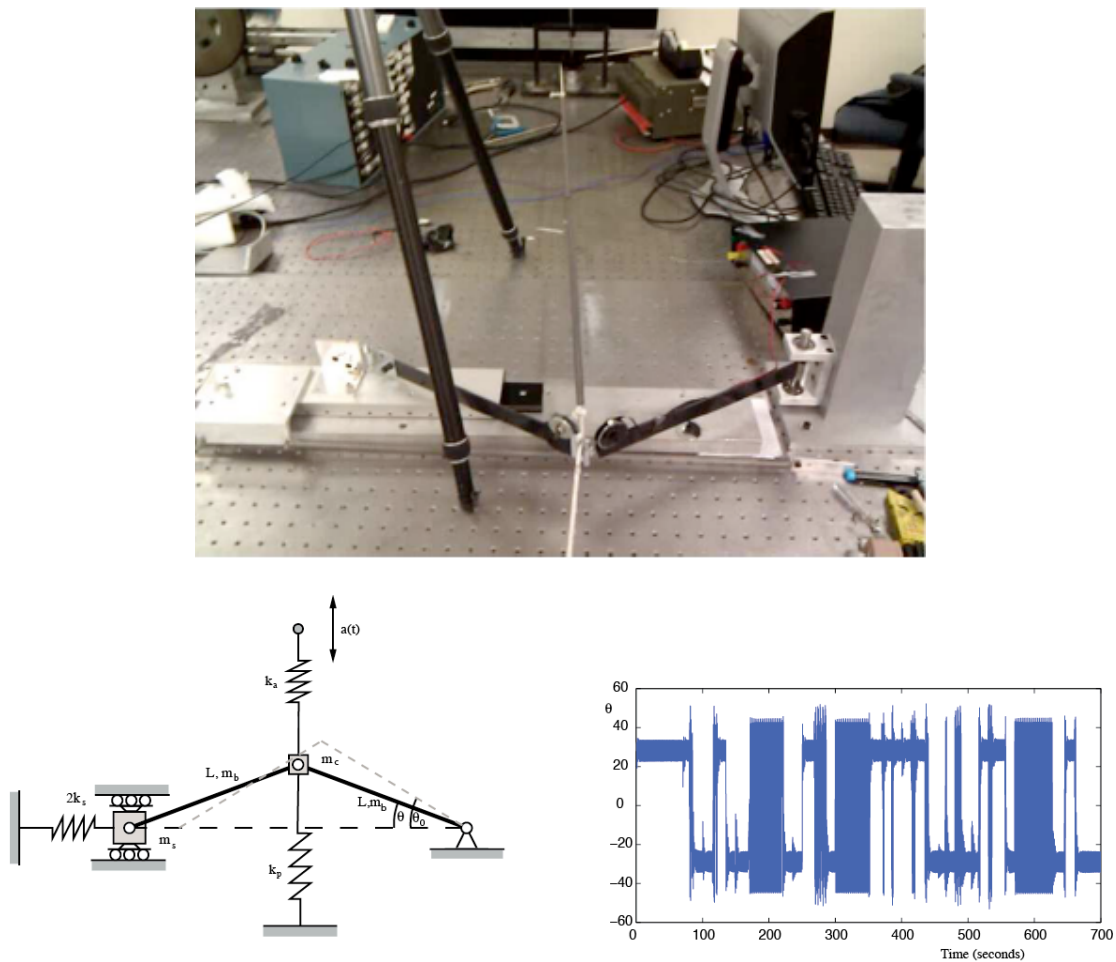


Figure 1: The link model, (a) the system as constructed in the lab, (b) a schematic, (c) a time series in which the system is perturbed between co-existing states.

More details of the types of dynamic behavior relating to this system can be found in references [1-4].

Summary of Numerical Results

A sophisticated finite element analysis and simulations of snap-through behavior was conducted by Prof. Stanciulescu (the subcontractor) and her students at Rice University. In addition to the mechanical instability of interest progress was also made on accounting for the coupling between mechanical and thermal loading.

As an example, Figure 2(a) shows through an indirect evaluation, a lower bound on the (snap-through) temperature that can be identified for a given shallow arch. This is the continuous analog of the discrete system discussed in the experimental section. Below these temperatures the arch will *not* experience snap-through. A direct method for tracing the stability boundary of coupled systems was also formulated and implemented. It can handle any type of critical points and also identifies mode changes, with a typical set of results displayed in Figure 2(b).

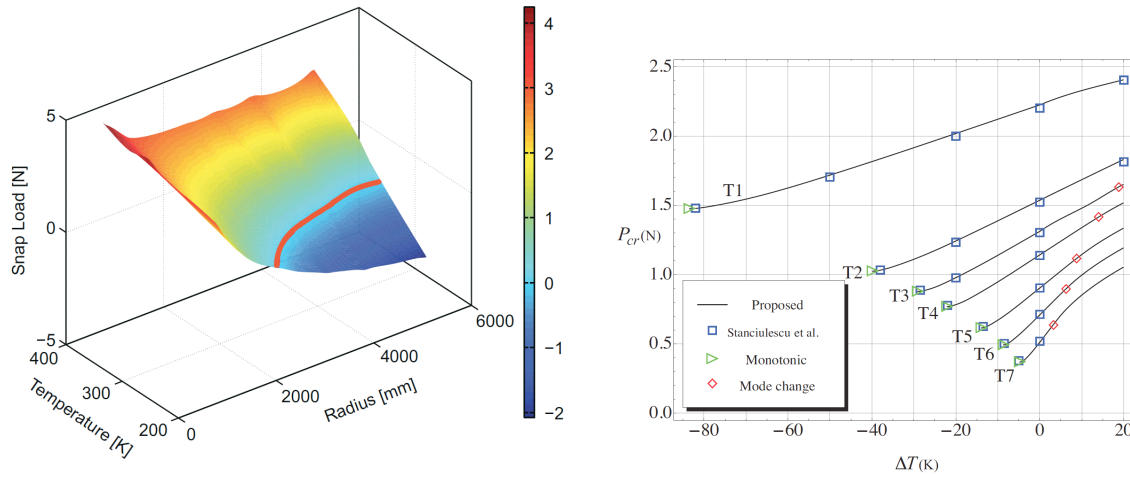


Figure 2: Sample finite element results, (a) Safe snap-through boundaries for a shallow arch including thermal loading, (c) Critical loads under various conditions.

Summary of Experimental/Numerical Correlation

One of the original goals of this research project was to utilize parallel approaches to experimental and numerical studies. A typical example is shown in Figure 3. The lower data (plotted in black) shows how the response of the experimental system depends strongly on the forcing parameters. The response of the system is monitored in terms of the number of 'snaps' per forcing cycle. For example, when the system is forced at a fixed amplitude, at a frequency Ω of 4 Hz, no snapping behavior occurs and the system simply oscillates (with small amplitude) about one of the (buckled) equilibria. Over the forcing frequency range $\Omega = 4.4$ to 6.2 the system may either not snap-through, or snap-through periodically (hence the '0' or '2' label). However, over the range $\Omega = 6.3$ to 9 Hz,

The system exhibit very complex (sometimes chaotic) behavior. Some sample time series are shown as insets in this figure. The upper part of the diagram shows the corresponding numerical result. The correlation is remarkable.

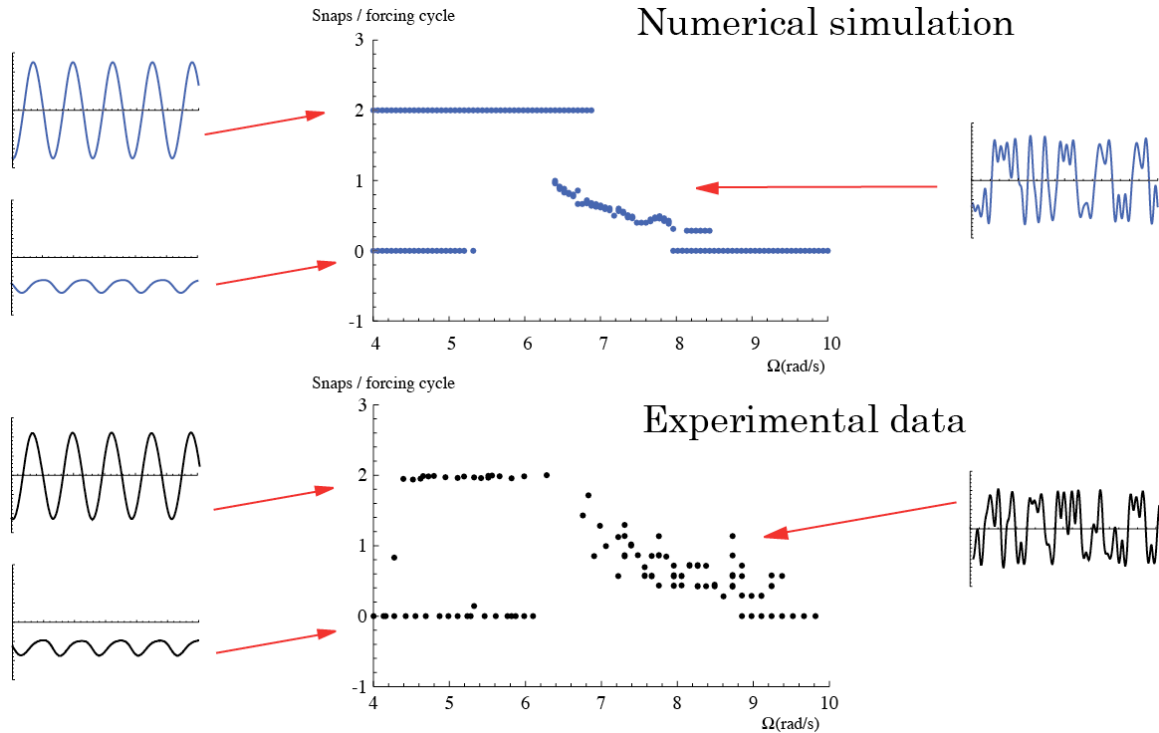


Figure 3: A comparison between experimental and numerical results.

Summary:

The research achieved in this program has resulted in a range of innovative approaches in both the experimental and computational realms. This work provides a strong foundation on which to build more sophisticated studies based on more realistic (panel and shell-like structures, including composites). The list of publications from this research are given below, and be consulted for further details.

Publication List:

- (1) R. Wiebe, L.N. Virgin, I. Stanciulescu, and S.M. Spottswood, 'On Snap-Through Buckling', *52nd AIAA/ASME/ASCE/AHS/ASC Structures, Structural Dynamics and Materials Conference*, Denver, CO (2011).
- (2) Y. Chandra, I. Stanciulescu, T.G. Eason, and S.M. Spottswood, 'Numerical Pathologies in Snap-Through Simulations', *Engineering Structures*, 34, pp.495-504, 2011.
- (3) I. Stanciulescu, T. Mitchell, Y. Chandra, T.G. Eason, S.M. Spottswood 'A lower bound on snap-through instability of curved beams under thermomechanical

- loads', *International Journal for Numerical Methods in Engineering*, accepted for publication.
- (4) I. Stanciulescu, Y. Chandra, and T.G. Eason, 'Boundaries of Snap-Through Buckling of Curved Beams', *52nd AIAA/ASME/ASCE/AHS/ASC Structures, Structural Dynamics and Materials Conference*, Denver, CO (2011).
 - (5) R. Wiebe and L.N. Virgin (2012) 'A heuristic method for identifying chaos from frequency content', accepted for publication in *Chaos: An Interdisciplinary Journal*.
 - (6) R. Wiebe, L.N. Virgin, I. Stanciulescu, S.M. Spottswood and T.G. Eason (2012) 'Characterizing dynamic transitions associated with snap-through: A discrete system', accepted for publication in *ASME Journal of Computational and Nonlinear Dynamics*.
 - (7) Y. Chandra, I. Stanciulescu, L.N. Virgin, T.G. Eason, and S.M. Spottswood 'Characterizing dynamic transitions associated with snap-through. A continuous model'. In final stages of preparation.
 - (8) R. Wiebe and L.N. Virgin 'The influence of damping on a transition through bifurcation', in preparation.

Characterizing Dynamic Transitions Associated with Snap-Through: A Discrete System

R. Wiebe

Graduate Research Assistant
Department of Civil Engineering
Duke University
Durham, NC 27708
Email: rwiebe1313@gmail.com

L.N. Virgin

Professor
Department of Mechanical Engineering
Duke University
Durham, NC 27708
Email: l.virgin@duke.edu

I. Stanciulescu

Department of Civil Engineering
Rice University
Houston, TX 77251
Email: ilince@rice.edu

S.M. Spottswood

Aerospace Engineer
Structural Mechanics Branch
AFRL/VASM, 2790 D Street WPAFB, OH 45433-7402
Email: Stephen.Spottswood@wpafb.af.mil

T.G. Eason

Aerospace Engineer
Structural Mechanics Branch
AFRL/VASM, 2790 D Street WPAFB, OH 45433-7402
Email: Thomas.Eason@wpafb.af.mil

ABSTRACT

Geometrically nonlinear structures often possess multiple equilibrium configurations. Under extreme conditions of excitation it is possible for these structures to exhibit oscillations about and between these co-existing configurations. This behavior may have serious implications for fatigue in the context of aircraft surface panels. Snap-through is a name often given to sudden changes in dynamic behavior associated with mechanical instability (buckling). This is an often encountered problem in hypersonic vehicles in which severe thermal loading and acoustic excitation conspire to create an especially hostile environment for structural elements. In this paper, a simple link model is used, experimentally and numerically, to investigate the mechanisms of snap-through buckling from a phenomenological standpoint.

1 Introduction

In order to meet ever increasing performance demands modern aircraft are being designed lighter than ever before. This weight efficiency usually leads to more slender structural components. Slender structures are susceptible to instabilities, particularly buckling, which can occur well before strength limits are reached. The nonlinear vibration of buckled structures may also lead to a large variety of chaotic and periodic oscillations. We are primarily interested in the circumstances under which a curved structure is forced to its inverted configuration, as shown in Fig. 1(a) and (b).

Snap-through buckling is a particular type of instability where the structure snaps from one state to another (remote) state. Such large deflections pose a hazard since they can exacerbate fatigue [1,2]. The two primary types of snap-through buckling, post buckled/bifurcated snap-through and limit point snap-through, are shown in parts (c) and (d) of Fig. 1 [3].

Limit point buckling occurs in structures where the stiffness decreases (with increasing loading) to a vanishing point, i.e., a horizontal tangency in the force-deflection relation (as shown in Fig. 1(c)). At the limit point the structure jumps to the remaining stable equilibrium. At loads below the limit point the structure may also snap-through under external perturbations. *Postbuckled snap-through* occurs in axially loaded structures, where a structure snaps between the two (often) symmetric buckled states under some perturbation, for example, from point δ_e to δ_e^* in Fig. 1(d). Postbuckled snap-through typically occurs after pitchfork buckling; and it often requires that the structure first be loaded to a buckled configuration (as shown in Fig. 1(d)). Related behavior can also occur in aircraft surface panels that may buckle due to thermal loading, [4–6].

When a structure with an underlying snap-through static behavior is subjected to excitation, then highly nonlinear oscillations are possible. In order to gain phenomenological insight into this type of response and enable relatively unambiguous experimental verification we introduce a very simple single degree of freedom (SDOF) discrete structural system (Fig. 2). This system, for a certain induced pre-stress through the axial spring $2k_s$, and $a(t) = \text{constant}$ (i.e., the actuator is held in a fixed position), possesses two symmetric static equilibria, $\theta = \pm\theta_e$. Furthermore, when the system is subject to 'lateral' excitation $a(t)$, we observe the possibility of complicated behavior involving motion that is heavily influenced by the locations of the underlying equilibria. A key aspect of this form of dynamic buckling is the existence of an unstable equilibrium between the stable states. These unstable equilibria define the basins of attraction for the stable states. Hence, the energies of the stable and unstable states may be useful for distinguishing between trajectories that snap from those that do not. The static equilibria, both stable and unstable, are therefore of great importance in studying the systems' forced dynamics. This system will be scrutinized using classical analysis techniques as well as experimental verification to shed light on the issue of dynamic snap-through in the larger context of aircraft structural components. Later work will focus on the multi-degree-of-freedom system, in which mode shapes, asymmetric behavior, etc. will be important features.

Single degree of freedom systems, particularly ones with Duffing-type potential wells, are well represented in the literature. An excellent review of the behavior of the forced Duffing oscillator is available in [7,8]. The route to potential well escape (i.e., snap-through for a mechanical system) is studied in [9] using Melnikov theory. Melnikov theory is also used in [10] to give a criterion for the existence of chaos in quasi-periodically forced Duffing oscillator. An SDOF structure with an underlying Duffing potential well was studied in [11]. This paper discusses the use of homoclinic orbits as the bifurcation indicator in an unforced system, and bifurcation to and from chaos with respect to harmonic forcing parameters.

A (modified) Duffing oscillator was studied numerically in [12,13]. In the vicinity of basin boundaries, small changes in initial conditions, parameters, or indeed in the numerical algorithm used, may lead to different attractors. A study of the bifurcations in forcing parameter space, similar to the goal of this research, is done in [14]. This work produced approximate analytical boundaries separating bounded from unbounded motion.

2 Experimental Setup

Shallow arches typically snap-through in a symmetric mode shape [15–19], and thus a SDOF link arch may be used to *qualitatively* model this behavior. For deeper arches, i.e., arches with a higher rise-to-span ratio, an asymmetric mode of buckling is typically encountered. Figure 3 is a photograph of the experimental SDOF link model tested. The two link arms were both carbon fiber and had a length of 32.4 cm and a mass of 41g. The center joint had a mass of 166g and the slider had a mass of 1260g. Note that the system was set up horizontally on a test bed and hence force due to gravity was out of the plane of the system dynamics.

The two axial springs are an essential component of the structure and result in the underlying multivalued potential energy surface which mimics a shallow arch. As a practical consideration it was decided to use two opposing mutually pre-tensioned springs (each with $k_s = 74$ N/m) to avoid inducing compressive forces, which would of course buckle the springs. The two transverse springs connected to the center joint provided a transmitted force to the system via the displacement of the opposite end of the active spring, k_a . The displacement was provided by a Scotch-yoke mechanism moving with an approximately sinusoidal motion [8]. The second (anchor) spring, k_p , ensured a pre-tension in the active spring. The active and anchor springs had stiffnesses of $k_a = 38$ N/m and $k_p = 23$ N/m respectively. The control parameters for the system were the Scotch-yoke amplitude and frequency which equate to the forcing amplitude and forcing frequency of the system.

The most natural generalized coordinate for this system is the angle of the link arm on the non-sliding side of the structure. This angle, θ , was measured using a high speed camera (Prosilica GC640). The arm position, and hence the angle, was obtained by locating a small white target on the link arm (see Fig. 3) by its contrast with the background using LabVIEW software. This process was done in real-time for each frame taken by the camera, providing a time series of the arm angle. Experimental results are discussed later in sections 4 and 5.

3 Modeling

A numerical model was developed to compare with the experimental results. Referring back to Fig. 2, we model the discrete dynamic system using an energy approach. Here, m_b is the mass of the link arms, m_c is the mass of the center joint (assumed to be a point mass), m_s is the mass of the slider assembly and joint, L is link length, k_s are the lateral structural spring stiffnesses, k_a is the active spring stiffness, k_p is the anchor spring stiffness, and θ is the angle of the link arm on the non-sliding side. The spring masses were considered negligible. The displacement at the end of the active spring $a(t)$ is transmitted as a force through the active spring to provide the system forcing. The angle θ_0 is the unforced equilibrium angle, i.e., the angle of the stable equilibrium with the forcing in the *neutral* position. Once again the effect of gravity is ignored in the analysis since the experimental system was laying flat. The kinetic and potential energies, along with the

energy dissipation of the system are given by

$$\begin{aligned}
T(\theta, \dot{\theta}, t) &= \left\{ \frac{1}{2} (m_c + \frac{1}{3}m_b) L^2 + \frac{1}{2}m_s x_s'(\theta)^2 \right. \\
&\quad \left. + \frac{1}{6}m_b [x_c'(\theta)^2 + x_c'(\theta)x_s'(\theta) + x_s'(\theta)^2 + y_s'(\theta)^2] \right\} \dot{\theta}^2, \\
V(\theta, t; \theta_1) &= k_s [x_s(\theta) - x_s(\theta_1)]^2 + \frac{1}{2}k_a [a(t) - y_c(\theta)]^2 + \frac{1}{2}k_p y_c(\theta)^2, \\
F(\theta, \dot{\theta}, t) &= \frac{1}{2}\beta [\dot{x}_s(\theta)]^2 = \frac{1}{2}\beta [x_s'(\theta)\dot{\theta}]^2,
\end{aligned} \tag{1}$$

where $x_c(\theta) = L\cos(\theta)$, $y_c(\theta) = L\sin(\theta)$, $x_s(\theta) = 2L\cos(\theta)$. The masses of the springs were small and their contribution to the kinetic energy was neglected. The slider mechanism was by far the largest contributor to the damping of the experimental system; therefore the dissipation function F was set to be a function of \dot{x}_s only. The angle θ_1 is the angle at which the two lateral structural springs were in equilibrium. This is the angle at which the potential energy of these two springs is at a minimum, i.e., the stable equilibrium of the system if the transverse (forcing) springs were removed. However the equilibrium states observed experimentally are at the stationary points of the total potential energy [20]. The two angles θ_0 and θ_1 are related by the expression

$$\frac{\partial}{\partial \theta} [V(\theta; \theta_1)]_{\theta=\theta_0} = 0. \tag{2}$$

Note that the two forcing springs, k_a and k_p , were set to be in equilibrium for $\theta = 0$.

The potential and kinetic energy equations may be substituted into the Euler-Lagrange equation [21]

$$\frac{d}{dt} \left(\frac{\partial(T - V)}{\partial \dot{\theta}} \right) - \frac{\partial T}{\partial \theta} + \frac{\partial V}{\partial \theta} + \frac{\partial F}{\partial \dot{\theta}} = 0, \tag{3}$$

to yield the equation of motion of the system:

$$\begin{aligned}
&[m_c + \frac{2}{3}m_b + 2(m_b + 2m_s)\sin^2\theta] \ddot{\theta} + (m_b + 2m_s)\sin(2\theta)\dot{\theta}^2 + 4\beta\dot{\theta}\sin^2\theta \\
&+ 8k_s(\cos\theta_1 - \cos\theta)\sin\theta + \frac{1}{2}(k_a + k_p)\sin 2\theta - (k_a/L)\cos\theta a(t) = 0.
\end{aligned} \tag{4}$$

The damping coefficient β (Kg/s) was determined by fitting a simulated (using fourth-order Runge-Kutta time stepping of Eq. (4) with $\Delta t = 0.001$ s) free decay response with the experimental response. In order to check the numerical stability of the Runge-Kutta routine it was also compared with simulations done using the *NDSolve* function available in *Mathematica*,

with excellent agreement. Figure 4 (a) shows this comparison between simulated and experimental time series (for $\theta_0 = 26.0^\circ$ and $\theta_1 = 36.2^\circ$). We note that the agreement is good, despite the large-amplitude, snap-through characteristic of the free decay. Parts (b) and (c) of this figure show the sensitivity of the simulation error norm (calculated as the average of the absolute difference between simulated and experimental time series up to $t = 6$ s) as a function of β . Part (b) is for the large amplitude experimental data points shown in part (a). The large jumps in the error occur because as the damping is changed the system will snap-through either too often (damping too low), or not enough (damping too high). The lower error region near $\beta = 0.65$ occurs because the system in fact snaps-through an extra two times and therefore returns to the same side as the experimental data so the error is actually lower than for higher values of β where only one extra snap event occurs. This leads to a smaller error norm even though it is less accurate. Note that although the system seems to be very sensitive to the damping coefficient, this plot corresponds to a single experimental time series. Finally part (c) shows a similar sensitivity study done using a small non-snapping free decay, which shows a clear minimum. Parts (a) and (b) hint that an optimal damping is approximately $\beta = 1.2$, whereas part (c), for the small amplitude decaying oscillation, has a optimal value closer to $\beta = 1.3$. This indicates that the system damping is slightly larger for small oscillations. However, since the results to be shown tended to be dominated by large amplitude oscillations the value $\beta = 1.2$ was used throughout. The model could be refined by including the effects of Coulomb damping such as in [22], where Coulomb friction is shown to induce follower forces on the system. However, due to the overall excellent agreement between the experimental and numerical results shown later, it was decided that the viscous friction used in the model is accurately portraying the system dynamics in general, including energy dissipation.

4 Equilibria and Stability

The static force-displacement relationship may be obtained by finding the static force (or in this case static displacement $a(t) \rightarrow a_e$) and angle θ_e for which the potential energy of the system exhibits a stationary point. The force-displacement relationship is given by

$$a_e = \frac{L}{k_a} \left[k_a + k_p + 8k_s \left(\frac{\cos \theta_1}{\cos \theta_e} - 1 \right) \right] \sin \theta_e. \quad (5)$$

According to the theorem of minimum potential energy the stability of the equilibria are given by the sign of the second derivative of the potential energy function [20]. A positive (negative) second derivative implies a minimum (maximum) potential and hence stable (unstable) equilibrium. An equivalent approach is to investigate the local natural frequency of the system for small oscillations about the equilibria under the static load being considered [3, 23]. This method is preferred because unlike potential energy it is easy to directly measure the response frequency of an experimental system. The natural frequency may also be of interest in its own right. The sign of ω^2 determines stability, i.e., if $\omega^2 > 0$ then disturbances do not grow in time. Linearizing the equation of motion about a static equilibrium position $\theta = \theta_e$ under a static load $a(t) = a_e$ produces the equation of a simple harmonic oscillator from which the undamped natural frequency is easily determined to

be

$$\omega_0^2 = \frac{8k_s L^2 \cos \theta_1 \cos \theta_e + (k_a + k_p - 8k_s) L^2 \cos 2\theta_e + k_a L a_e \sin \theta_e}{\frac{1}{2} \left(m_c + \frac{1}{3} m_b \right) L^2 + \frac{1}{3} m_b L^2 + 2(m_b + 2m_s) L^2 \sin^2 \theta_e}, \quad (6)$$

where the numerator is the second derivative of the potential energy. Given that the denominator of equation (6), i.e., the inertia, is positive definite, this result is clearly in agreement with the theorem of minimum potential energy.

Figure 5 shows the relationship between the force (static displacement of the actuator a_e), displacement, and local natural frequency for both the experimental system and the analytical model (for $\theta_0 = 26.0^\circ$ and $\theta_1 = 36.2^\circ$). The experimental response frequency is necessarily the damped natural frequency, whereas in the analytical result is the undamped natural frequency. However, because the damping is relatively small these two values are still very close. For the experimental results there are no data points in the unstable region given that these equilibria cannot be observed. However the agreement is excellent in the stable region.

The static equilibria of dynamical systems, and underlying potential energy, give much insight into the dynamic response, i.e., they act as an organizing framework for the nonlinear behavior. If the system is subject to periodic excitation, they also influence large amplitude snap-through oscillations and highly nonlinear global behavior. This will be considered in the next section.

5 Dynamic Response

The forced dynamic response of the system was simulated by applying a fourth-order Runge-Kutta time stepping scheme on Eq. (4) with $a(t) = A \sin \Omega t$. Figure 6 shows some typical periodic responses from the system in Fig. 5 (numerical simulation in parts (a) and (b) and experimental in parts (c) and (d)). Each time series was produced with a forcing amplitude of $A = 6.25$ cm (compare with the $A_{snap} \approx 8.21$ cm), however parts (a) and (c) corresponded to a forcing frequency of $\Omega = 4.40$ rad/s while parts (b) and (d) corresponded to $\Omega = 3.36$ rad/s. The transmissibility of the forcing mechanism effectively translates to a moving restoring force, but superimposing the phase trajectories in this way gives a clear indication of whether the system is oscillating about, or snapping between, the two sides of the system. It is interesting that there is better agreement between the numerical and experimental results for the large snap-through motion in Fig. 6(b) and (d) than for the small non snap-through motion in (a) and (c). It is likely that this is due to some nonlinear damping effects that were not included in the model, particularly Coulomb damping (already discussed earlier), which has a more pronounced effect on slower motions.

Figure 7 shows several time series from simulation (a-d) and experiment (e-h), this time for a more shallow angle $\theta_0 = 15.0^\circ$ ($\theta_1 = 29.9^\circ$) and $A = 1.10$ cm (compare with $A_{snap} \approx 1.56$ cm). The relatively simple 'period-one (P1)', periodic responses shown in parts (a,b,e,f) correspond to a forcing frequency of $\Omega = 4.9$ rad/s, i.e., they co-exist at this set of parameter values, and which attractor occurs depends on the initial conditions. This aspect of the behavior will be revisited a little later.

The non-simple but still periodic responses shown in parts (c and g) are not quite the same. The numerical result shown

in part (c) occurred for $\Omega = 7.6$ rad/s and can be characterized as a 'period-four (P4)' oscillation, i.e., it repeats itself every four forcing cycles. The experimental result shown in part (g) is for a slightly different forcing frequency ($\Omega = 7.9$ rad/s) and is in fact a P5 oscillation. The chaotic behavior for the numerical result (part d) corresponds to $\Omega = 7.8$ rad/s and the experimental result (part h) corresponds to $\Omega = 8.1$ rad/s. These values are very close to those used to generate the time series in parts (c and g), thus suggesting a parameter sensitivity in this range.

The frequency content of these time series (see Fig. 8 for the more interesting time series) can be quite useful in assessing certain qualitative features of the dynamics. They can also assist in determining whether the system is exhibiting snap-through oscillations, since it is typically somewhat difficult to consistently distinguish between trajectories that snap-through from those that do not. The broadband nature of the discrete Fourier transform (DFT) of a time series is of course a well-established signature of chaos.

Figure 9 contains a 'bifurcation' diagram of snap-through behavior as a function of forcing frequency with ($\theta_0 = 15.0^\circ$, $A = 1.10$ cm). Parts (a) and (b) show the number of snap-through events per forcing cycle from simulation and experimental results, respectively. A snap-through event was considered to be any crossing of the state $\theta = 0$. This definition of snap-through works relatively well for the system because the unstable equilibria does not change significantly with the forcing. Each data point in part (a) indicates the result of one simulation with the snap-through events per forcing cycle being averaged over 1000 forcing cycles after the transients were given sufficient time to decay. The plot was created by running 10 simulations with random initial conditions for 100 forcing frequencies to capture co-existing attractors. The experimental data points were instead obtained by performing a moving average of the number snap-through events per forcing cycle on a sweep-up followed by a sweep-down through forcing frequency. The sweep-up and -down primarily differ in the region below $\Omega = 6.2$ rad/s where the sweep-up did not snap-through and the sweep-down did. The responses that snap-through twice per forcing cycle indicate a snap-through *in-phase* with the forcing, i.e., P1 snap-through (see Fig. 7(b and f) for example time series). The responses with intermediate occurrences of snap-through indicate responses with occasional, or sporadic, snap-through, which may occur in higher-period periodic behavior (Fig. 7(c and g)) and chaotic behavior (Fig. 7(d and h)). Figure 9(c) shows the likelihood (via simulation only) of the system response converging to one of the three competing types of behavior seen in parts (a) and (b), where green corresponds to no snap-through, red corresponds to P1 snap-through, and blue is higher-periodic or chaotic (less frequent) snap-through. The likelihood was measured by running 100 simulations at random initial conditions at each frequency. This method may be more difficult to apply to higher dimensional systems as the separatrices are typically more complex and may be more dependent on the system forcing. However, in this relatively simple system it gives a straightforward interpretation of a potentially onerous event (snap-through) and thus useful data to inform practical issues including life-time fatigue predictions.

Another approach might be to observe some kind of energy measure of a given response. For a system to snap-through it is postulated that the external forcing must add a sufficient amount of energy to the system. Figure 10 shows the average kinetic energy over a span of forcing cycles against the forcing frequency for the same parameters as Fig. 9. The experimental data points were obtained by first sweeping slowly up, then down, through forcing frequency. The agreement between the experimental and numerical results is excellent, with only a slight horizontal shift in the data points.

One anticipates that the average kinetic energy of a system would be much larger for trajectories that traverse across the unstable equilibria than for those that oscillate about a single equilibria; however this detection is made more difficult by responses that only occasionally snap-through. This typically occurs with very high periodic, or more often, chaotic responses, which prevail for much of the right half of the energy plots. This makes the determination of chaos another important aspect of the analysis, especially since it is known that single well chaos is relatively rare [24].

The standard method of identifying chaos is to determine the Lyapunov spectrum of the system. Lyapunov exponents (LE) are however relatively difficult to determine from experimental data [25]. Figure 11(a) shows the LE obtained from the simulation of equation (4) (using the method in [26]) against forcing frequency. The data points were produced by running 10 simulations for different random initial conditions at 100 frequencies to make it possible to capture co-existing attractors. When comparing with Fig. 10 it appears that most of the chaotic responses of the system occur for snap-through trajectories.

An alternative approach is introduced in [27], whereby the number of distinct frequency spikes (peaks on the DFT, above a certain threshold) of a dynamical system are plotted against the parameter used for the simulation/experiment. There is typically a clear dichotomy in the number of peaks for a chaotic response with a broadband spectrum and a non-chaotic response with a finite number of peaks, making identification of chaos possible. Figure 11(b) shows the identification of chaos using this peak count method. In these results 10 simulations with randomly generated initial conditions were run at 100 forcing frequencies. It is confirmed that the chaotic responses are almost entirely within the region of high energy response.

An interesting 'second-order' feature in these plots is an assessment of how chaotic a signal might be. Two sample time series (indicated by the vertical dashed red lines) are also shown in Fig. 11(c) and (d). Part (d) corresponding to $\Omega = 7.6$ rad/s shows a slightly stronger periodicity than the time series shown in part (c) ($\Omega = 7.0$ rad/s): the second half of the time series appears nearly periodic, this short term periodicity is ubiquitous throughout the time series as the trajectory appears to spend more time oscillating about (rather than between) the underlying static equilibria. When subject to the LE algorithm this periodic signature results in a slightly less positive LE, and there are a few less spectral peaks occurring above the threshold. It is not uncommon for a chaotic trajectory to spend periods of time in a near-periodic state (a typical chaotic attractor has embedded within it many unstable periodic orbits). It was also just mentioned that in certain (relatively small) regimes of forcing frequency co-existing oscillations occur. In order to illuminate this feature, Fig. 11(e) shows the outcome of 100 simulations using randomly generated initial conditions, in which the percentage of numerical simulations that lead to chaos is charted for both the LE (dashed black line) and the peak-count (solid green line) approaches. Clearly, both criteria are effective in distinguishing chaotic from non-chaotic motion. Outside of this range of forcing frequencies the behavior was typically non-chaotic, although co-existing attractors could still exist, and the periodic motion could be either small-amplitude (contained within the vicinity of an equilibrium), or relatively large-amplitude (cross-well) motion.

The same approach was also applied to the experimental system. Figure 12 shows bifurcation diagrams, based on 18 tests, in terms of chaotic vs. non-chaotic behavior. The computation of the largest Lyapunov exponent (λ) is based on a standard algorithm [28] in which a time series is assessed in terms of the exponential rate at which nearest neighbors tend to evolve in time. This can be a sensitive undertaking, for example, part (a), for $\Omega = 6.518$, and (b), for $\Omega = 8.140$ of

Fig. 12 show how the approach requires a linear fit. This is by no means straightforward. The red dashed lines in (a) and (b) show an approximately exponential divergence (the y-axis is a log-scale) for short time evolutions. However, the response in part (a) is characterized by a very small slope and corresponds to a periodic oscillation, whereas the case in part (b) is more convincingly positive and corresponds to a chaotic oscillation. Part (c) of this figure summarizes this behavior, and part (d) shows the equivalent results based on the peak count criterion. The red dashed lines in these parts show the specific frequencies at which the snapshots were taken for parts (a) and (b). The peak counts approach appears to be more robust and easier to apply than the conventional LE approach. The agreement with the numerical results is quite good. The bifurcations are slightly shifted, however the progression and even some of the periodic windows are still captured.

6 Conclusions

Snap-through buckling is investigated on a SDOF system. Some aspects of the underlying force-deflection and free vibration behavior of the system are described. Under the action of periodic excitation, the focus of interest shifts from equilibria to oscillatory behavior. In a broad sense, the behavior of the forced system can be divided into regimes of either small-amplitude or large-amplitude behavior. This latter response can be associated with snap-through behavior - an often highly undesirable behavior in many structural applications. Alternatively, the behavior can be divided into regimes of chaotic and non-chaotic behavior. Chaos is commonly associated with snap-through behavior but they are not necessarily the same thing. A promising method of distinguishing between small- and large-amplitude responses based on average total energy is introduced and applied to the system with good agreement between experimental results and the numerical model. Another method based on distinguishing between chaotic and non-chaotic responses is also proposed. In general, this work provide a useful overview of how snap-through behavior depends on the forcing parameters.

Acknowledgments

The authors acknowledge the support of Air Force Office of Scientific Research (AFOSR) grant FA9550-09-1-0204.

References

- [1] B. Clarkson. Review of sonic fatigue technology. *Tech. Report, NASA Contract Report 4587*, 1994.
- [2] S. Suresh. *Fatigue of Materials, 2nd edition*. Cambridge University Press, 1998.
- [3] L. N. Virgin. *Vibration of Axially Loaded Structures*. Cambridge University Press, 2007.
- [4] S. P. Timoshenko and S. Woinowsky-Krieger. *Theory of Plates and Shells, 2nd Edition*. McGraw Hill, 1959.
- [5] L. W. Chen and L. Y. Chen. Thermal buckling of laminated composite plates. *Journal of Thermal Stresses*, 10(4):345–356, 1987.
- [6] K. D. Murphy, L. N. Virgin, and S. A. Rizzi. The effect of thermal prestress on the free vibration characteristics of clamped rectangular plates: theory and experiment. *Journal of Vibration and Acoustics*, 119:243–249, 1997.

- [7] Y. Ueda. Survey of regular and chaotic phenomena in the forced Duffing oscillator. *Chaos, Solitons & Fractals*, 1:199, 1991.
- [8] L. N. Virgin. *Introduction to Experimental Nonlinear Dynamics*. Cambridge University Press, 2000.
- [9] J. M. T. Thompson. Fractal basins and chaotic bifurcations prior to escape from a potential well. *J. M. T. Thompson and S. R. Bishop and L. M. Leung*, 121:116, 1987.
- [10] S. Wiggins. Chaos in the quasiperiodically forced Duffing oscillator. *Physics Letters A*, 124:138, 1987.
- [11] I. Ario. Homoclinic bifurcation and chaos attractor in elastic two-bar truss. *International Journal of Nonlinear Mechanics*, 39:605, 2004.
- [12] P. S. Addison, A. H. C. Chan, D. A. Ervine, and K. J. Williams. Observations on numerical method dependent solutions of a modified Duffing oscillator. *Communications in Applied Numerical Methods*, 8:519, 1992.
- [13] L. Bardella and F. Genna. Newmark's time integration method from discretization of extended functionals. *Journal of Applied Mechanics*, 72:527, 2005.
- [14] A. H. Nayfeh and N. E. Sanchez. Bifurcations in a forced softening Duffing oscillator. *International Journal of Nonlinear Mechanics*, 24:483, 1989.
- [15] C. Hsu. Stability of shallow arches against snap-through under timewise step loads. *Journal of Applied Mechanics*, 35:31–39, 1968.
- [16] L. Rehfield. Nonlinear flexural oscillations of shallow arches. *AIAA Journal*, 12:91–93, 1974.
- [17] E. Johnson and I. McIvor. The effect of spatial distribution on dynamic snap-through. *Journal of Applied Mechanics*, 45:612–618, 1978.
- [18] W. Gregory and R. H. Plaut. Dynamic stability boundaries for shallow arches. *Journal of Engineering Mechanics*, 108:1036–1050, 1982.
- [19] R. H. Plaut and J. C. Hsieh. Oscillations and instability of a shallow arch under two-frequency excitation. *Journal of Sound and Vibration*, 102:189–201, 1985.
- [20] J. M. T. Thompson and G. W. Hunt. *A General Theory of Elastic Stability*. Wiley, 1973.
- [21] H. Goldstein, C. P. Poole, and J. L. Safko. *Classical Mechanics (3rd Ed.)*. Addison Wesley, 2001.
- [22] D. Bigoni and G. Noselli. Experimental evidence of flutter and divergence instabilities induced by dry friction. *Journal of the Mechanics and Physics of Solids*, To appear.
- [23] L. N. Virgin. Parametric studies of the dynamic evolution through a fold. *Journal of Sound and Vibration*, 110:99–109, 1986.
- [24] J. A. Gottwald, L. N. Virgin, and E. H. Dowell. Experimental mimicry of Duffing's equation. *Journal of Sound and Vibration*, 158:447–467, 1992.
- [25] G. Q. Wu, N. M. Arzeno, L. L. Shen, D. K. Tang, D. A. Zheng, N. Q. Zhao, D. L. Eckberg, and C. S. Poon. Chaotic signatures of heart rate variability and its power spectrum in health, aging and hear failure. *Plos One Open Access*, 4:1–9, 2009.
- [26] W. C. Xie. *Dynamic Stability of Structures*. Cambridge University Press, 2006.

- [27] R. Wiebe and L. N. Virgin. A heuristic method for identifying chaos from frequency content. *Chaos*, To appear.
- [28] M. T. Rosenstein, J. J. Collins, and C. J. D. Luca. A practical method for calculating the largest Lyapunov exponents from small data sets. *Physica D: Nonlinear Phenomena*, 65:117–134, 1993.

Figure Captions:

1. A typical curved panel, and two schematic scenarios in which such a system might exhibit a snap-through event in its force-displacement relationship. (a) pre-snap, (b) post-snap, (c) limit point buckling, (d) pitchfork bifurcation.
2. A single degree of freedom (SDOF) link model.
3. (a) Photograph of experimental setup, (b) the low-friction pin joint, (c) the Scotch-yoke forcing mechanism.
4. Identification of damping parameter β (Kg/s). (a) A typical nonlinear free decay; the points are experimental data, and the continuous line represents the numerical integration of equation (4) with $\beta = 1.2$. (b) Normalized average error vs. β for the large amplitude time series (in part (a)). (c) Normalized average error vs. β for a small amplitude time series.
5. Free response characteristics. (a) force vs. natural frequency (squared), (b) force vs. deflection, (c) natural frequency (squared) vs. deflection. The points are experimental data, the continuous lines are the theoretical results.
6. Experimental and simulated time series superimposed on the restoring force. Numerical, (a) $\Omega = 4.40$ rad/s; (b) $\Omega = 3.36$ rad/s; Experimental, (c) $\Omega = 4.40$ rad/s; (d) $\Omega = 3.36$ rad/s.
7. Numerical (a-d) and experimental (e-h) time series. (a) $\Omega = 4.9$ rad/s; (b) $\Omega = 4.9$ rad/s; (c) $\Omega = 7.6$ rad/s; (d) $\Omega = 7.8$ rad/s; (e) $\Omega = 4.9$ rad/s; (f) $\Omega = 4.9$ rad/s; (g) $\Omega = 7.9$ rad/s; (h) $\Omega = 8.1$ rad/s.
8. Experimental and simulated DFT's for parts (c,d,g,h) in Fig.7 respectively.
9. Occurrence of snap-through. (a) simulation, (b) experiment, (c) relative dominance of co-existing attractors (simulation only). Green - non-snap, red - P1 snap-through, blue - higher periodic or chaotic (less frequent) snap-through. The vertical dashed red lines in (a) and (b) indicate the specific frequencies relating to Fig.7.
10. Average kinetic energy as a function of forcing frequency, (a) simulation, (b) experiment.
11. Distinction between chaotic and non-chaotic behavior based on (a) the largest Lyapunov exponent, (b) the peak-count criterion; (c) and (d) typical chaotic time series, (e) relative dominance of chaotic behavior.
12. Experimental LE and peak count. (a) and (b) typical linear fits for the local rate of divergence, (c) Largest LE as a function of the forcing frequency, (d) corresponding peak count result.

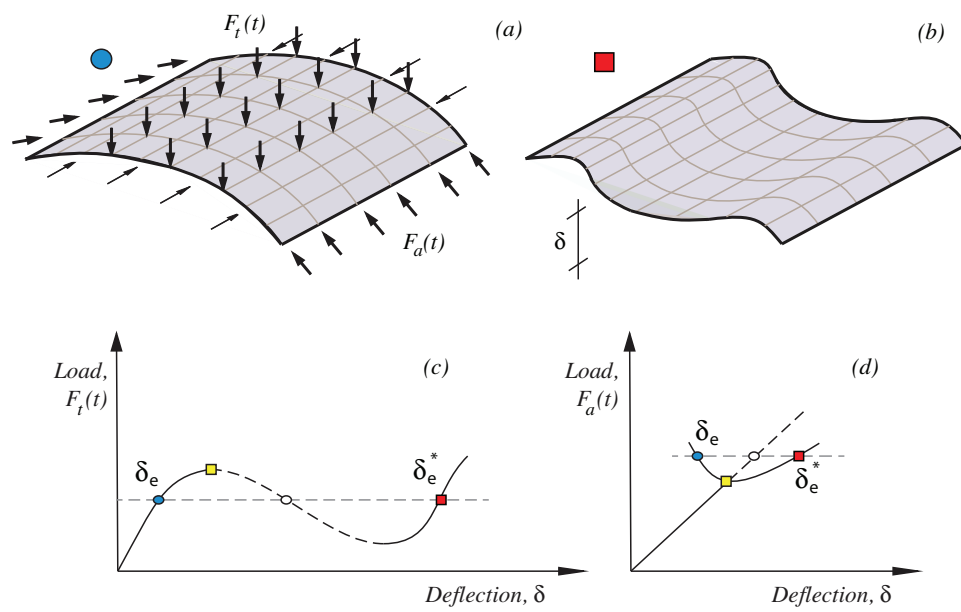


Fig. 1. figure1.eps

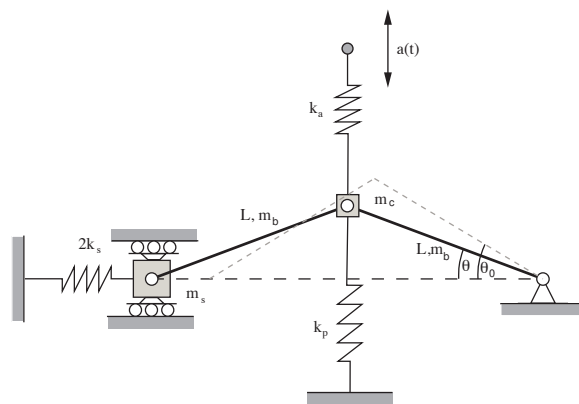


Fig. 2. figure2.eps

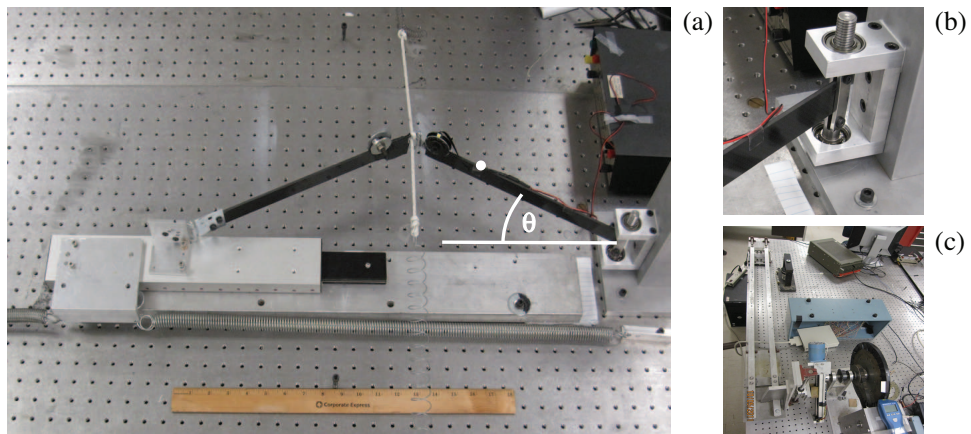


Fig. 3. figure3.eps

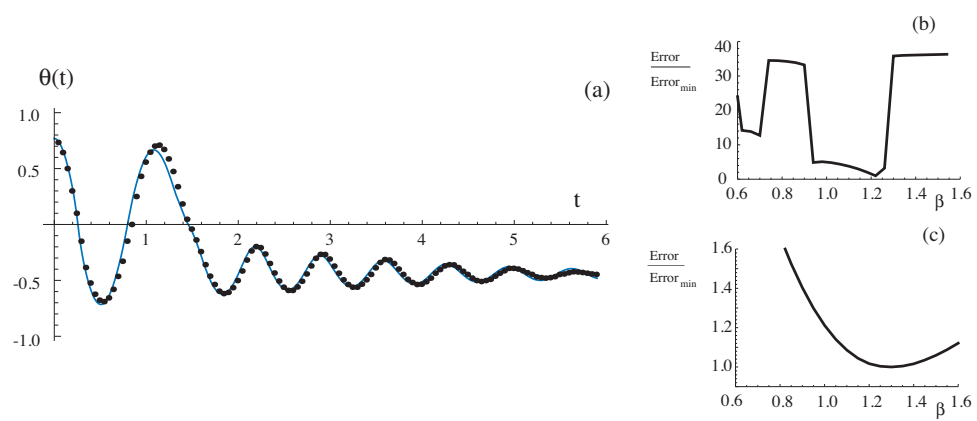


Fig. 4. figure4.eps

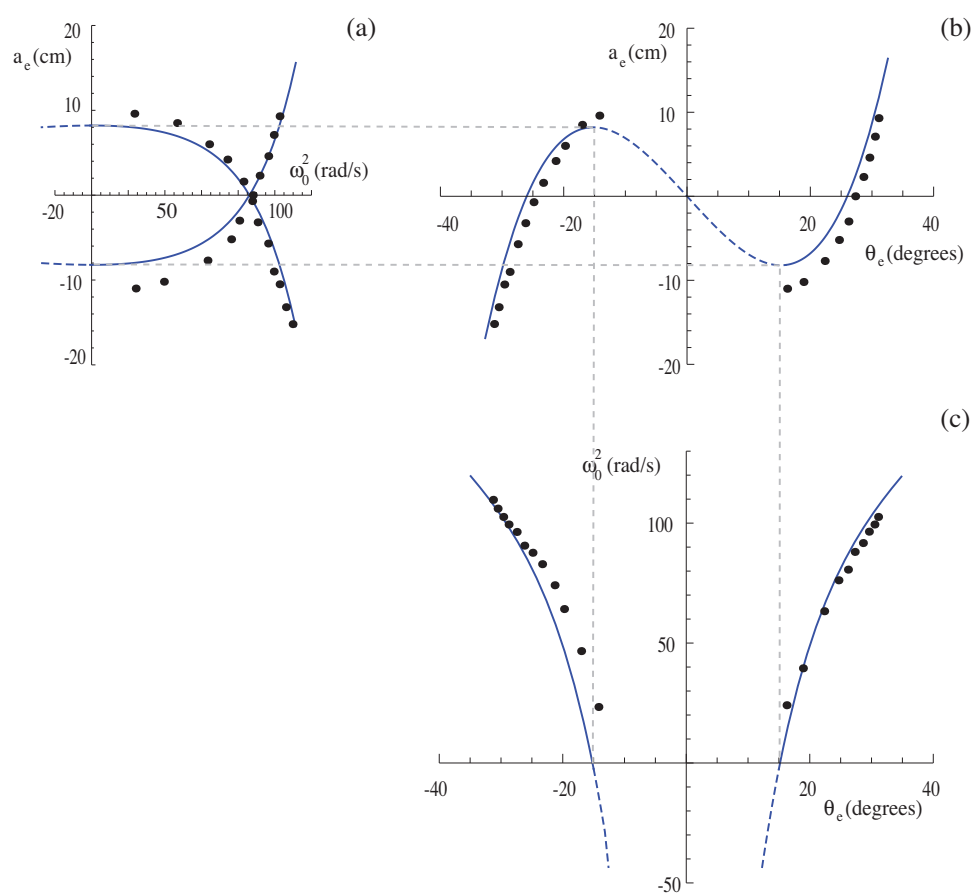


Fig. 5. figure5.eps

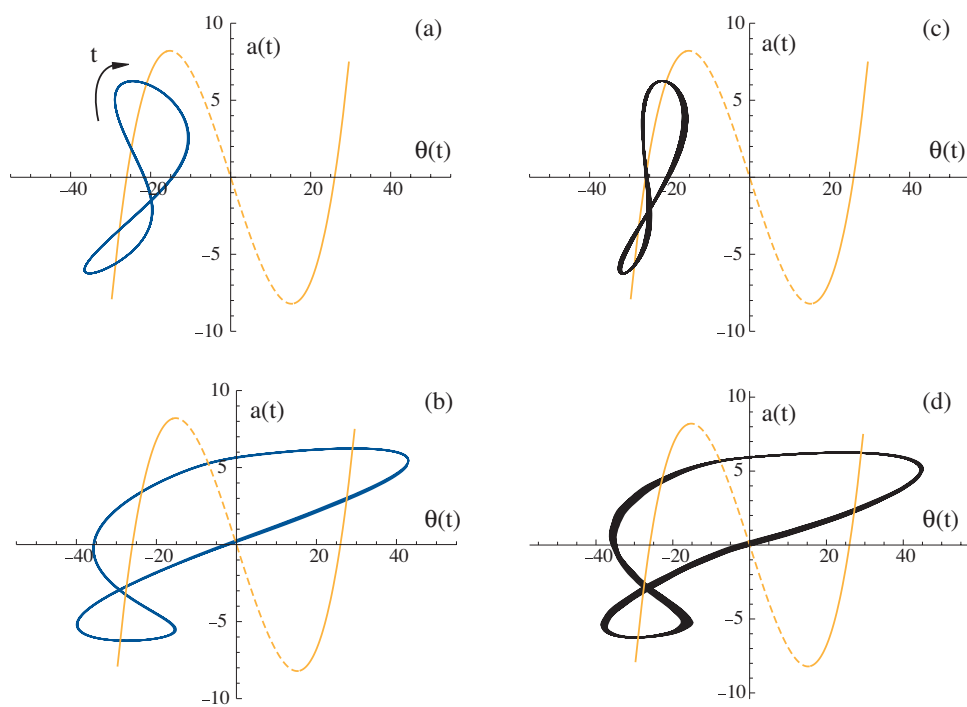


Fig. 6. figure6.eps

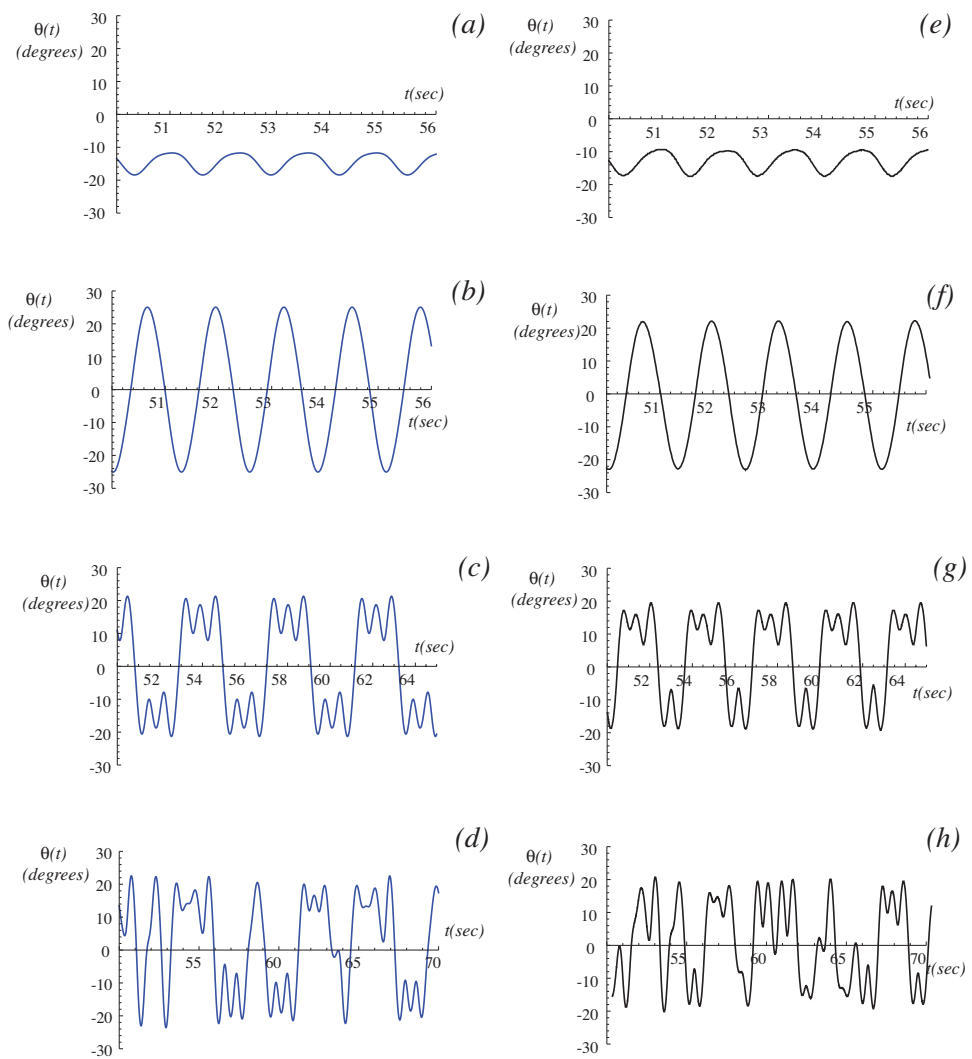


Fig. 7. figure7.eps

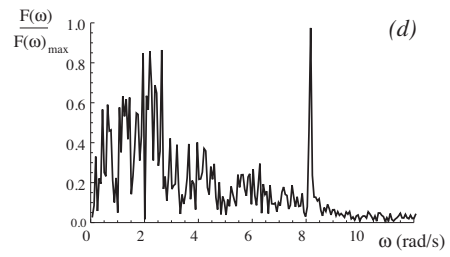
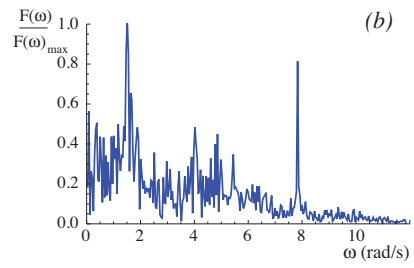
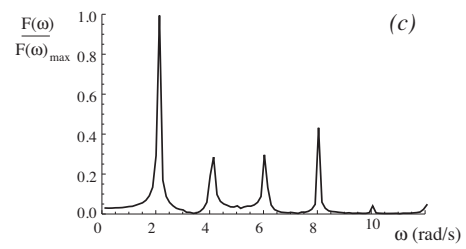
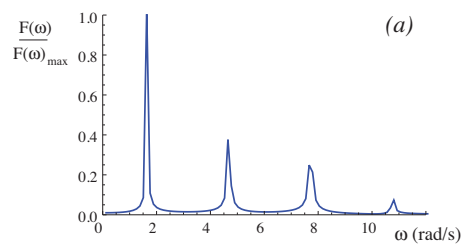


Fig. 8. figure8.eps

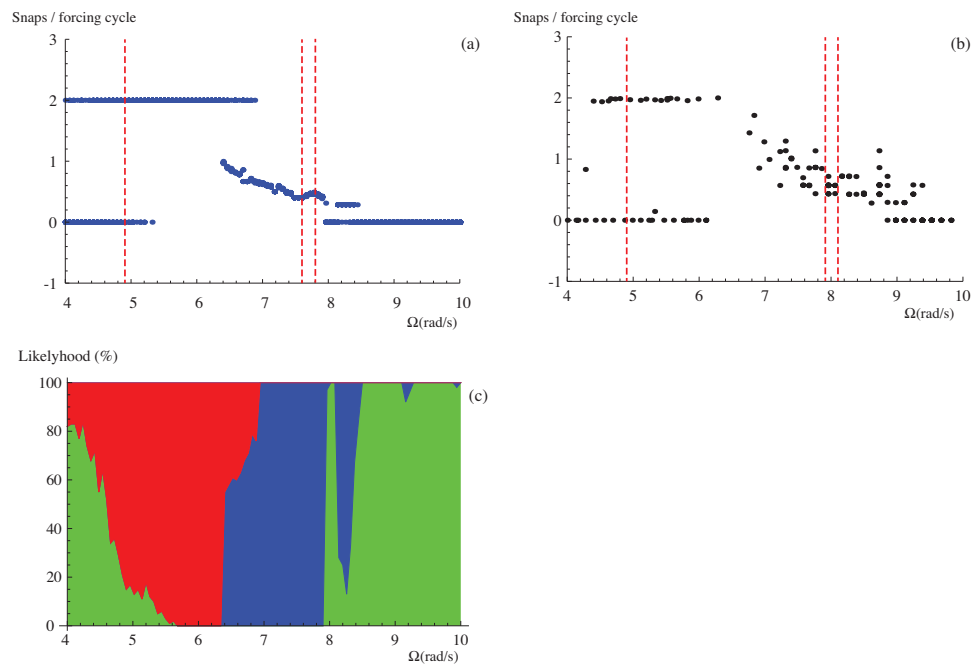


Fig. 9. figure9.eps

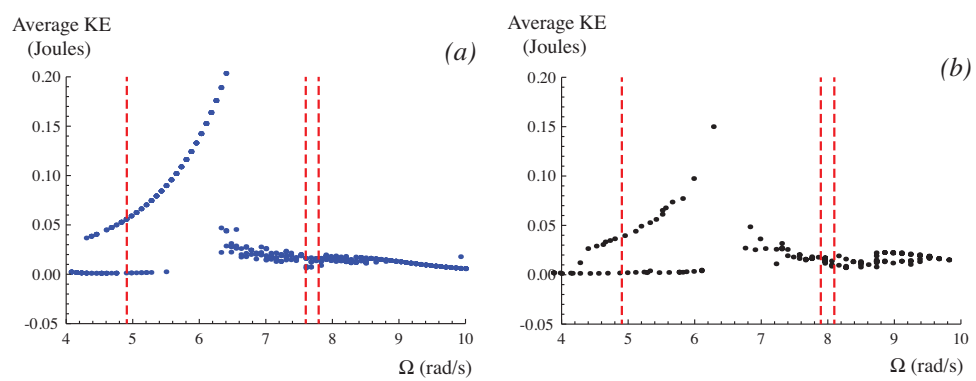


Fig. 10. figure10.eps

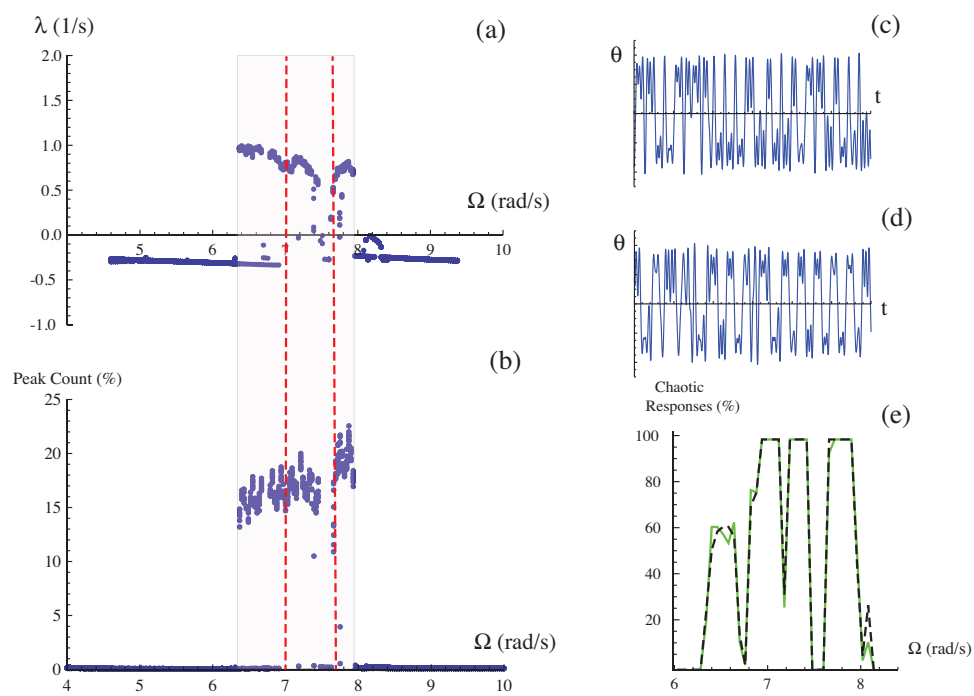


Fig. 11. figure11.eps

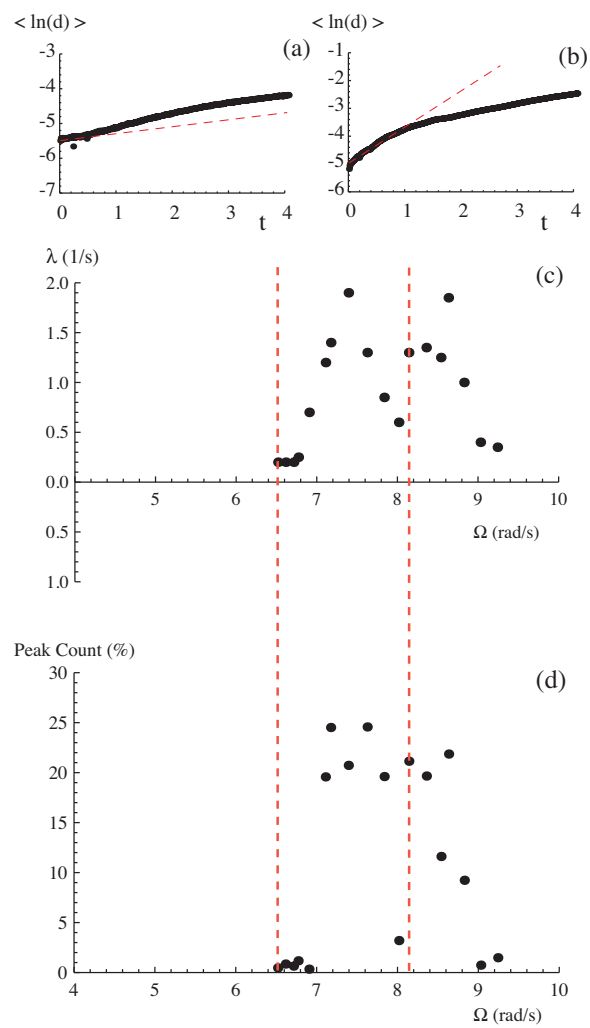


Fig. 12. figure12.eps

A Heuristic Method for Identifying Chaos from Frequency Content

R. Wiebe^{1, a)} and L.N. Virgin^{1, b)}

School of Engineering, Duke University, Durham, NC.

(Dated: 2 November 2011)

The sign of the largest Lyapunov exponent is the fundamental indicator of chaos in a dynamical system. However, although the extraction of Lyapunov exponents can be accomplished with (necessarily noisy) experimental data, this is still a relatively data-intensive and sensitive endeavor. This paper presents an alternative pragmatic approach to identifying chaos using response frequency characteristics and extending the concept of the spectrogram. The method is shown to work well on both experimental and numerical data.

Keywords: Chaos, Lyapunov Exponents, Frequency Analysis

It is often easy to distinguish between chaotic and nonchaotic trajectories by visual inspection of their time series and frequency spectra. The frequency transform of chaotic time series generally show certain characteristic signatures such as fractal geometry and broadband frequency content. This is contrasted with the distinct signature of periodic, or nonchaotic behavior. The heuristic method developed herein uses a quantifiable measure based on the broadband non-smooth nature of the frequency spectra of chaotic trajectories. The method is then verified numerically and experimentally by comparison with the largest Lyapunov exponent.

I. BACKGROUND

Chaos is defined as the output of a deterministic dynamical system that exhibits sensitivity to initial conditions. If the governing equations are known then it is usually straightforward to interrogate (especially chaotic) behavior. In the experimental (noisy) context, however, it is more challenging to characterize behavior under certain parameter regimes. An excellent summary of time series analysis and chaos is provided in¹⁻³. The Lyapunov exponent (LE) spectrum of a dynamical system describes the divergence/convergence rate of nearby trajectories in state space⁴ and is the most direct measure of chaos. Determining the LE spectrum of a numerical system can, in principle, be done directly as the full system state is known. An algorithm for calculating the LE's of a numerical system is given in⁵. For experimental data, however, the process is more difficult since not all states are typically measured and because the linearization (or normalization) required in calculating the LE is not possible. Therefore in order to extract the LE's of an experimental system one must normally reconstruct the

phase portrait via time lag embedding and then use the method of nearest neighbors to analyze the divergence rates⁶⁻⁸. This method typically requires long time series to ensure accuracy and requires some tuning of the time span over which the divergence remains approximately exponential, i.e. the time span over which the LE may be calculated. The difficulty of calculating LE's from noisy time series is discussed in⁹.

In many dynamical systems the presence of noise can lead to a phenomenon known as unstable dimension variability (see¹⁰ for an overview). This occurs when the number of stable, unstable, and neutrally stable eigendirections change intermittently when a system is perturbed between co-existing invariant sets by noise. One anticipates that this phenomenon would further complicate the calculation of LE's.

Another interesting approach for identifying chaos is discussed in¹¹ whereby noise is artificially added to a signal in order to find the threshold noise limit whereby the nonlinearity becomes undetectable. This 'titration' method is shown to work quite well and has the added benefit of also revealing the level of noise in the system, however it also requires one to choose some nonlinearity indicator.

Frequency analysis is commonly used to characterize noisy signals and is a standard procedure in signal processing. The power spectrum of noisy signals has long been used to characterize the noise type with the power spectrum power law¹². The frequency content of deterministic or systems with minimal noise is also commonly used to qualitatively identify whether a time series is chaotic or periodic¹³⁻¹⁵. However, the inspection must be done qualitatively and therefore the method is not tractable for a full investigation of the parameter space of a dynamical system. Attempts have been made to automate the identification process by assigning a single metric to the power spectrum or DFT of a time history such as its fractal dimension¹⁶. The heuristic method discussed and developed herein, which consists of a counting the peaks on the DFT, was first mentioned in¹⁷. However, the method was only applied to a numerical system, and the effects of noise were not thoroughly discussed. The effect of noise on the method was studied numerically in¹⁸. In the following, the same method is applied to an experimental system, which serves to validate its

^{a)}Electronic mail: rw75@duke.edu.

^{b)}Also at Center for Nonlinear and Complex Systems, Duke University, Durham, NC.

practicality, and confirm its ability to work well even in the presence of real noise.

II. THE HEURISTIC METHOD

It is often straightforward to distinguish between chaotic and nonchaotic trajectories by inspecting their frequency spectra. A periodic signal will have a spectrum dominated by a single peak (harmonic) or a finite set of peaks for a more complicated but still periodic, or quasi-periodic, signal. Noise tends to cause a slight spread in the width of these peaks and some underlying low level energy across the frequency spectra, but the peaks are generally still easy to distinguish. For a chaotic response, on the other hand, the spectral content is spread over a relatively broad range of frequencies. A spectrogram or waterfall plot¹⁹ summarizes these effects as a system parameter is changed, i.e., there is a distinct change in the frequency signature at a bifurcation. In some circumstances we wish to display different types of behavior as two parameters are changed. Spectrograms are however limited to showing bifurcations in a single parameter, as two dimensions are needed to display the frequency spectra themselves.

The Heuristic method used herein extends the idea of the spectrogram to allow plotting of multi-parameter, especially two-parameter, systems. The heuristic approach relies on the noisy nature of the Fourier transform of chaotic trajectories and is summarized in Fig. 1. First a DFT/FFT is applied to a time series of the dynamical system of interest. For a steady-state response it is appropriate to use just a single sample (as used in the examples in this paper), providing sufficient data is used to capture the essential dynamics. Just as in the calculation of LE's one needs to allow the system to settle onto the attractor prior to beginning the calculation of the DFT. Once the DFT is obtained a **threshold** value is chosen based on the maximum peak height of the frequency spectra, represented by the dashed line in Fig. 1. The number of peaks (local maxima) above this threshold are counted. If the number of peaks counted is above a second **threshold** the system is considered chaotic, otherwise it is labeled periodic. The challenge arises in choosing the two threshold values. The DFT of a periodic signal contains only a handful of peaks at resonant frequencies as in Fig. 1(a). However in the presence of noise (or rounding error in the case of simulation) the curve, when magnified, will contain many local maxima especially near zero (as in Fig. 1(b)). The first threshold can therefore usually be chosen to be a small percentage of the maximum peak height, and therefore only the *excited* frequencies will be counted for a periodic signal. Chaotic signals, however, produce many peaks on a similar order of magnitude to the maximum peak as seen in Fig. 1(c). The dichotomy of peak counts seen in Fig. 1 are typical of many systems and usually make it relatively easy to tune the threshold values.

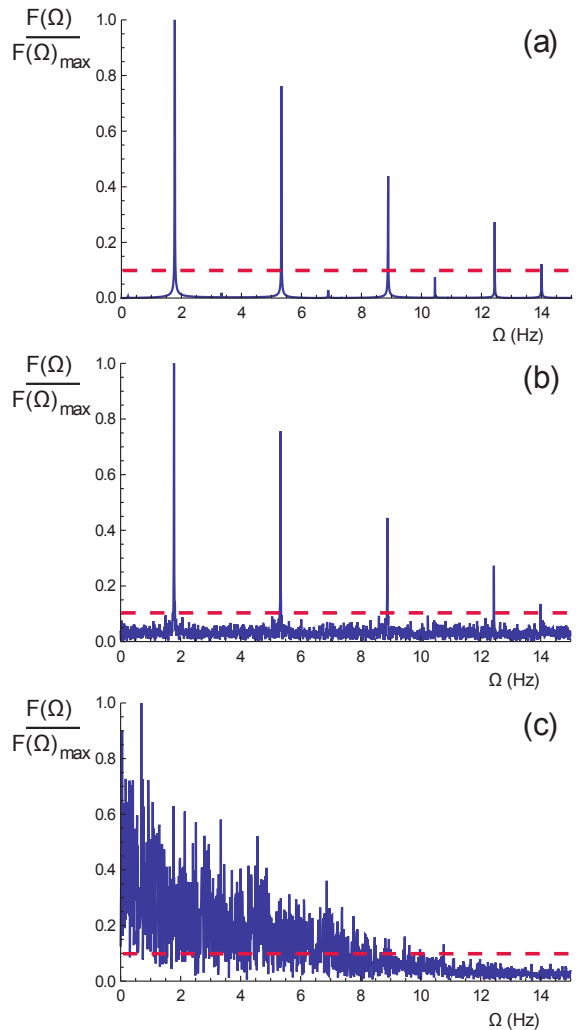


FIG. 1. Illustration of heuristic method with typical signals, (a) periodic, (b) periodic with noise, (c) chaotic.

Typically any state of a system may be used to generate the DFT as periodic motion in one state of a coupled system typically implies periodic motion in the other states. However, certain states may produce frequency spectra in which chaos is easier to ascertain, for instance in a pendulum angular velocity is bounded whereas the angle is not.

In essence this method emulates visual identification of chaos from frequency spectra, and therefore allows for high resolution sweeps through system parameters in a relatively hands-off fashion. This allows one to build an indicator function over the parameter space with a binary output describing the response as either chaotic or periodic. As will be seen, no distinction is made between different types of periodic behavior. In similarity with any bifurcation diagram, capturing coexisting attractors would require additional testing based on varying initial conditions. In practice however, the method is most useful for plotting boundaries in two-parameter space separating chaotic from nonchaotic motion.

One particular advantage of this method over LE's is the ease of implementation; one needs only apply a frequency transform, a standard signal processing feature. It may also be used together with LE's to provide a level of mutual verification. Despite its simplicity the method proves to be surprisingly robust (in the presence of real noise) and matches excellently with the LE's of the numerical model, while being much easier to obtain than experimental LE's.

The method may run in complications for systems with a low signal to noise ratios due to the noise raising the number of peaks on the DFT. One possible method to counteract this is discussed in¹, where several DFT's are averaged to reduce noise in the DFT.

III. TEST CASE: A NONLINEAR MECHANICAL OSCILLATOR

A. Experimental Setup

The heuristic method was tested on the experimental nonlinear mechanical oscillator shown in Fig. 2. The oscillator is a product of "Pasco Systems" and consists of a pendulum with a torque spring. The pendulum is comprised of an aluminum disk, with an off-center brass weight. The torque spring is made up of a pair of linear springs connected by a string that is looped over a pulley attached behind the pendulum. The springs also supply the forcing to the system. The forcing is transmitted by the active spring attached to the pendulum by the displacement of the forcing arm on the motor, as shown in the bottom inset of Fig. 2. The forcing motor is connected to the active spring by a string which passes through the guide-post (also visible in the bottom inset of Fig. 2). The guide-post is necessary to transform the circular motion of the forcing arm into a linear, nearly sinusoidal, motion on the active spring. The secondary, anchor, spring ensures that both springs are always in tension to avoid needing a tension-compression capable spring. The response of the system is measured by a rotary motion sensor attached to the axle of the pendulum. The forcing is also measured by a rotary motion sensor attached to the forcing string directly above the guide-post.

The potential energy function underlying the system is the summation of a sinusoidal gravity potential due to the eccentric mass (the brass attachment), and a parabolic potential due to the linear torque spring. By altering the eccentric mass and the torque spring stiffness one is able to choose the number of static equilibria of the system; one may choose 1, 3, 5, ... equilibria in an appropriate operational range. Another parameter in the experimental system is the zero point of the forcing, i.e. the angle of the forcing arm and the corresponding position of the static equilibria. For this paper the spring stiffness and mass were chosen such that there were three equilibria with the forcing zeroed, with the unstable equilibria be-

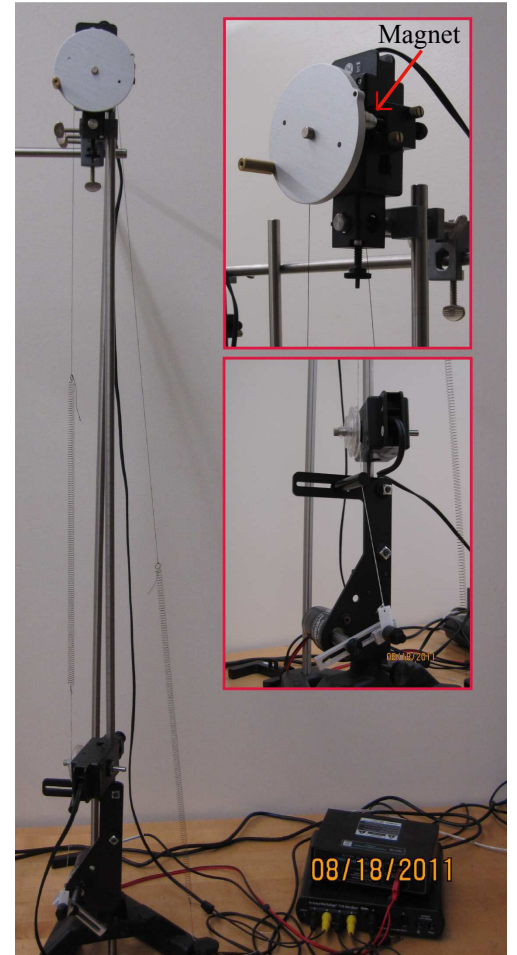


FIG. 2. Experimental apparatus.

ing the inverted pendulum state and therefore two symmetric stable equilibria (one of which is shown in the top inset figure 2). The force zero point was chosen to be when the forcing arm was horizontal. This was selected because setting a horizontal forcing arm coinciding with a vertical unstable equilibrium (i.e. inverted pendulum state) was the easiest to consistently calibrate between experimental runs.

B. Numerical Modelling

Figure 3 shows a schematic of the experimental apparatus, where θ is the angle of a ray projected to the eccentric mass from the pivot measured counter-clockwise from vertical, $y_0(t)$ is the time varying linear displacement of the driving string above the guide-post, m is the mass of the brass attachment, M is the mass of the aluminum disc, r_m is the radius of the aluminum disc (note that the eccentric mass is centered at the edge of the disc), r_p is the radius of the pulley attaching the springs to the pendulum, k_1 and k_2 are the stiffnesses of the active and anchor springs respectively, and d is the

distance between the guide-post and the axle of the driving motor. The two adjustable forcing parameters for the system are the length of the forcing arm L and the forcing frequency f . The rotary motion sensor attached to the forcing string (located between the guide-post and spring 1) is omitted for clarity. The equation of motion describing the system is given by

$$\begin{aligned}\ddot{\theta} + 2\zeta\omega_0\dot{\theta} + \omega_0^2\theta - \frac{mgr_m}{I}\sin\theta &= \frac{k_1r_p}{I}y_0(t), \\ \omega_0^2 &= \frac{1}{I}(k_1 + k_2)r_p^2, \\ I &= mr_m^2 + \frac{1}{2}Mr_m^2,\end{aligned}\quad (1)$$

where a small linear viscous damping term with coefficient ζ is inserted to capture the viscous energy dissipation of the system.

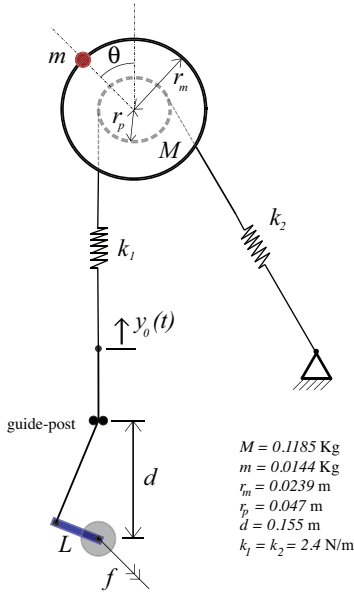


FIG. 3. Schematic of system (not to scale).

The choice of zero-ing the forcing with the forcing arm horizontal leads to a slightly biased forcing due to the geometry relating the forcing arm and the guide-post as shown in Fig. 3. The motion of the string above the guide-post driving the active spring is given by

$$y_0(t) = \sqrt{d^2 - 2Ld\cos(2\pi ft) + L^2} - \sqrt{d^2 + L^2}. \quad (2)$$

Note that it was decided to *not* normalize the length scale as the units are of a physically appreciable scale, and there is no clear meaningful characteristic length for the system. Figure 4 shows a time series and a time lag plot (with a time lag of one forcing period) of Eqn. (2) versus experimental measurement and a sinusoid for comparison. It is clear that Eqn. (2) captures both the bias and the shape better than the sinusoid.

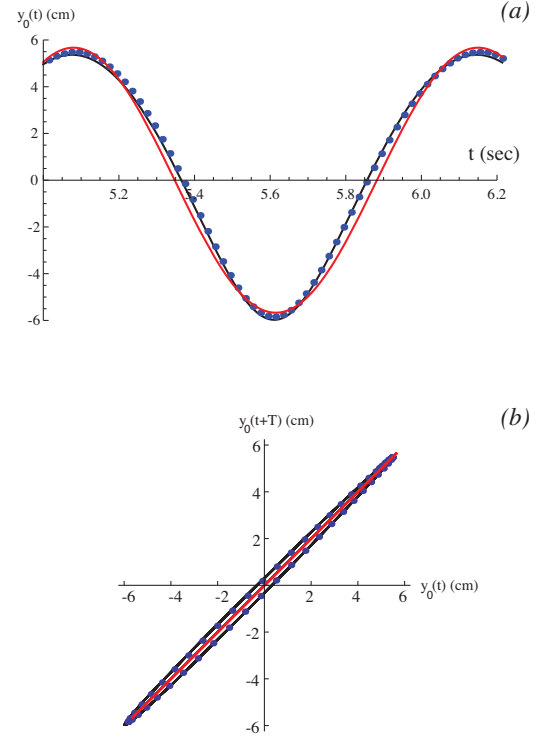


FIG. 4. System identification: forcing. Dots = experimental data, black line = Eqn. (2), red line = sinusoid. (a) Time series, (b) time lag portrait.

Damping is provided by eddy current drag from the interaction between the aluminum disc and a permanent magnet placed slightly behind it (visible in the top inset of Fig. 2). This form of damping is described in²⁰ and is shown to be linear viscous damping as long as velocities are not too large. Determining at which velocity the linear viscous damping assumption fails requires extensive electromagnetic analysis and was not investigated. The excellent agreement between experimental and numerical results shown later, however, suggest that the velocities obtained experimentally are well below this threshold.

For a linear system there are many well-tested methods of assessing energy dissipation such as logarithmic decrement and the half-power methods²¹. In order to apply these methods the eccentric brass mass was removed leaving a simple linear oscillator (Eqn. (1) with $m = 0$). The damping coefficient obtained by removing the mass must however be corrected by

$$\zeta = \sqrt{\frac{I_{m=0}}{I}}\zeta_{m=0} \approx 0.90\zeta_{m=0}. \quad (3)$$

The correction is necessary because the damping is linearly proportional to velocity prior to normalization, i.e. the term $2\zeta\omega_0 I$ is constant. Therefore ζ must change inversely with \sqrt{I} since $\omega_0 \propto 1/\sqrt{I}$.

Figure 5 shows the results of three different methods of assessing damping. The logarithmic decrement method

uses successive peak heights in the free decay time series' as shown in 5 (a). The damping coefficient can be approximated by the relation $\zeta = \ln(A_n/A_{n+m})/2\pi m$. The blue and black lines in part (a) both yielded $\zeta_{m=0} \approx 6.0\%$ or $\zeta \approx 5.4\%$ for the corrected damping coefficient. Part (b) shows the frequency response curve for a forcing amplitude of $L = 5.5\text{cm}$. This curve is used in the half power method to obtain the damping coefficient from the relation $\zeta = (f_2 - f_1)/2f_0$ which yields $\zeta_{m=0} \approx 6.5\%$ or $\zeta \approx 5.9\%$ for this system. A subtle issue with this approach is that the half power relation is derived for a sinusoidal forcing function, however as already shown the forcing for this system is not quite sinusoidal. Finally part (c) shows the result of an error minimization approach, whereby the time averaged error between a simulated free decay (Eqn. (1) with $m = 0$, $y_0 = 0$) and the experimental time series (from part (a)) is plotted against the $\zeta_{m=0}$ value used for the simulation. The minimum error occurs for $\zeta_{m=0} \approx 6.2\%$ or $\zeta \approx 5.6\%$. The first inclination when presented with multiple measurements is to take their average. However, since the three methods are so different, it is not necessarily true that the average will be any more physically relevant than any individual result. It is also unlikely that the results are accurate to the tenth of a percent. Therefore it was decided to simply take $\zeta = 6\%$ as two of the methods round to this value.

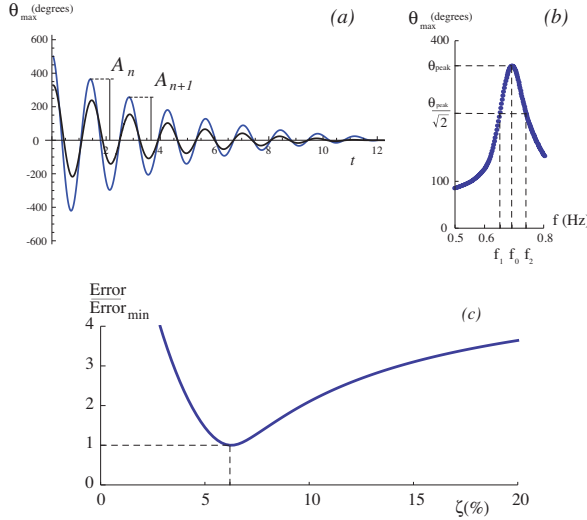


FIG. 5. System identification: damping. (a) Logarithmic decrement, (b) half power method with $f_1 = 0.65\text{Hz}$, $f_0 = 0.69\text{Hz}$, and $f_2 = 0.74\text{Hz}$, (c) error minimization.

The equation of motion (Eqn. (1)) was simulated using a fourth-order Runge-Kutta time stepping scheme²², and is in excellent agreement with the experimental results. Figures 6 and 7 show the numerical and experimentally obtained time series' and DFT's of a small amplitude and large amplitude period 1 (i.e. one response cycle for every forcing cycle) oscillation respectively. Figure 8 shows the same for a period 3 (i.e. one response cycle

for every 3 forcing cycles) oscillation with the addition of the phase portraits to highlight the more complicated motion. Finally Fig. 9 shows the numerically and experimentally obtained time series', phase portraits, DFT's, and Poincaré sections for a chaotic oscillation. The phase portraits were all obtained using time lag embedding with a time lag of a quarter of the forcing period. The chaotic Poincaré section data was however taken once per forcing cycle, and numerical differentiation was used to obtain the angular velocity experimentally. (The dashed line running across the DFT's for all of these samples is at 5% of the maximum peak height. This is the cut-off used for peak counting in the Heuristic method applied later.)

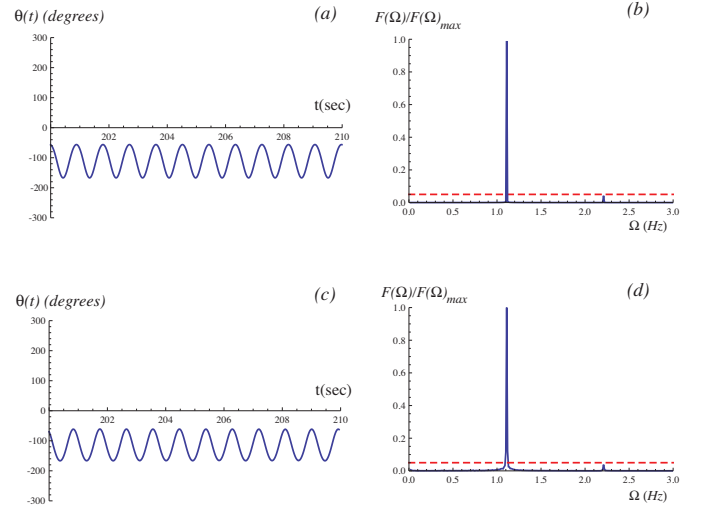


FIG. 6. Small amplitude period 1 oscillation, $L = 5.5\text{cm}$ and $f = 1.10\text{Hz}$. (a) Numerical time series, (b) numerical DFT, (c) experimental time series, (d) experimental DFT.

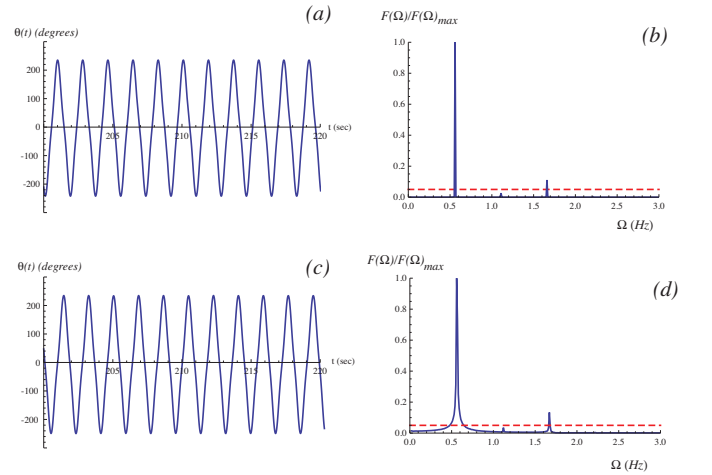


FIG. 7. Large amplitude period 1 oscillation, $L = 5.5\text{cm}$ and $f = 0.55\text{Hz}$. (a) Numerical time series, (b) numerical DFT, (c) experimental time series, (d) experimental DFT.

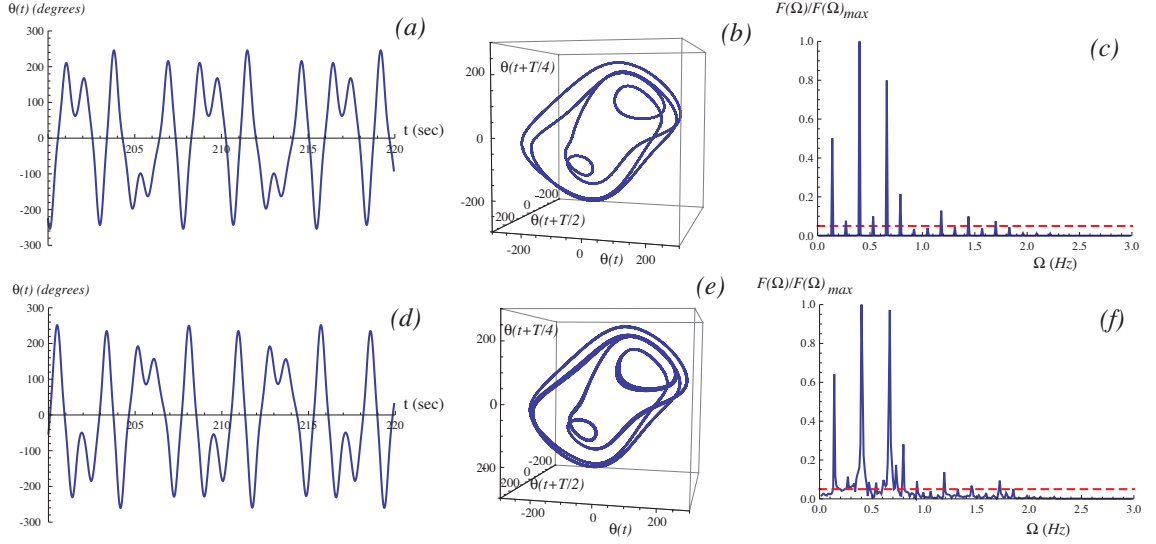


FIG. 8. Period 3 oscillation, $L = 5.5\text{cm}$ and $f = 0.39\text{Hz}$. (a) Numerical time series, (b) numerical phase portrait, (c) numerical DFT, (d) experimental time series, (e) experimental phase portrait, (f) experimental DFT.

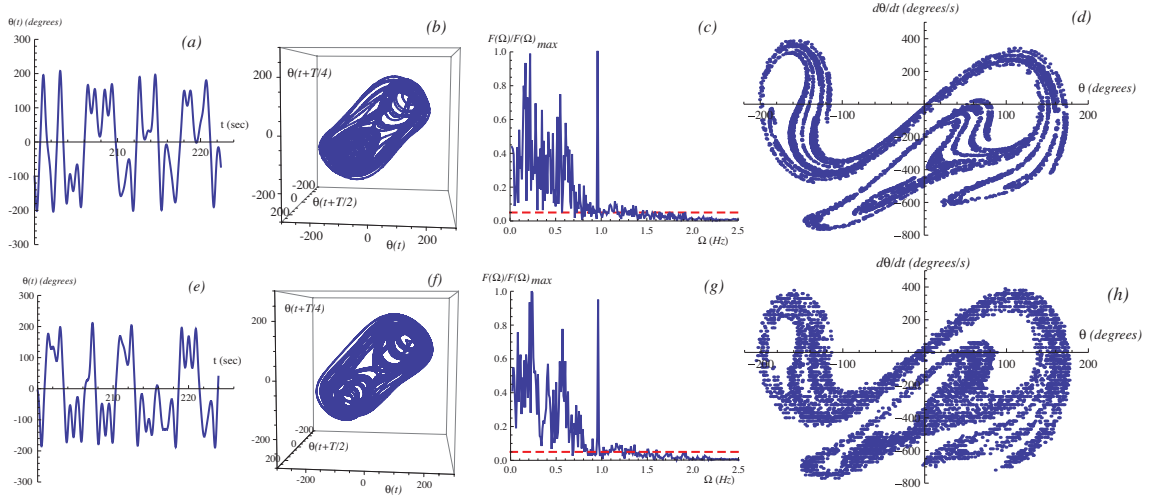


FIG. 9. Chaotic oscillation, $L = 5.5\text{cm}$ and $f = 0.95\text{Hz}$. (a) Numerical time series, (b) numerical phase portrait, (c) numerical DFT, (d) numerical Poincaré section, (e) experimental time series, (f) experimental phase portrait, (g) experimental DFT, (h) experimental Poincaré section.

C. Identification of Chaos

There are many applications where one is interested the parameter dependence of a system. There are many forms of bifurcation diagrams used to present the qualitative changes (in our case whether the response is chaotic or nonchaotic) in behavior with respect to a change in parameters. Producing bifurcation diagrams, especially experimentally, is typically a laborious process. Any method that would reduce the amount of data required to qualify the nature of a response as chaotic or nonchaotic would therefore be highly advantageous.

Spectrograms are at the heart of the heuristic method and may be used as a one-dimensional bifurcation di-

agram. Figure 10 shows numerical and experimental spectrograms over a range of forcing frequencies with the forcing amplitude held constant at $L = 5.5\text{cm}$. The ordinate of the spectrograms is the response frequency while the contour indicates the power of the system (dark colors are low power, light colors high power) at that frequency. The resolution of the spectrograms is 100 and 58 individual DFT's respectively for the numerical and experimental plots respectively, with each DFT containing 300 data points between 0 and 3 Hz. Spectrograms are useful in that they clearly indicate the components of a periodic response, and show chaotic regions as bands of erratic contouring. Their downside is that since one dimension is used to plot the response frequency, only one

system parameter may be studied at a time. The heuristic method works to free-up this dimension, rather than plotting the entire DFT of a response, only the number of peaks is plotted. In doing this one loses the information about the nature of a periodic response, however there is still a clear difference between chaotic and periodic responses. Figure 11 shows the number of peaks out of a total possible 300 points on the DFT versus the forcing frequency (again for $L = 5.5\text{cm}$) for the numerical and experimental system. In order to make the comparison more direct, the numerical resolution (again along the forcing frequency axis) was reduced down to 58 to match the number of experimental tests performed. The cut-off threshold for this plot was set at 1% of the maximum peak height to eliminate false peaks (due to noise) being counted. It is clear that this method produces a useful alternative bifurcation diagram as the number of peaks in the chaotic and nonchaotic regions is easy to distinguish. Note that dashed vertical lines denote the locations of the four samples in Fig.'s 6 to 9.

All of the time series used, both experimentally and numerically, were first allowed to run for a period of 200 seconds to allow transients to decay and then the following 100 seconds were recorded for analysis. The selection of these two times should be made on a system specific basis. In the case of periodically forced systems this is made somewhat easier, as one may just select a time period long enough to capture several forcing periods. However, one also needs to consider how many points they require on the DFT of the response. This is important when applying the heuristic method because the number of peaks on a periodic response does not typically increase with resolution, whereas for a chaotic response the number does increase with resolution. Therefore there should be enough points to allow for a clear difference in peak counts, where this distinction will grow more and more clear with increasing resolution.

The sensitivity of the peak count cut-off threshold is investigated in Fig. 12 for the experimental data. Part (a) shows that a wide range of threshold values from 1% to 10% of the maximum peak height yield easily distinguishable regions of chaos and periodic behavior. For the case of a 0% cut-off periodic responses begin to be masked by noise, making it difficult to distinguish chaotic from periodic responses. This is expected and is due to the low magnitude peaks in the DFT discussed earlier. Part (b) shows the peak count values versus the cut-off threshold for a periodic ($f = 0.55\text{ Hz}$) and chaotic ($f = 0.95\text{ Hz}$) trajectory. These two frequencies correspond to Fig. 7 and Fig. 9 respectively. This highlights the drastic difference between the peak counts for periodic and chaotic trajectories. The peak counts fall off very rapidly with threshold for the periodic case, while they only gradually drop off for the chaotic case. This shows that the output (binary output of either chaotic or nonchaotic) is quite insensitive to the selection of the cut-off threshold. The method is still likely limited to systems with relatively high signal to noise ratios where the noise does not

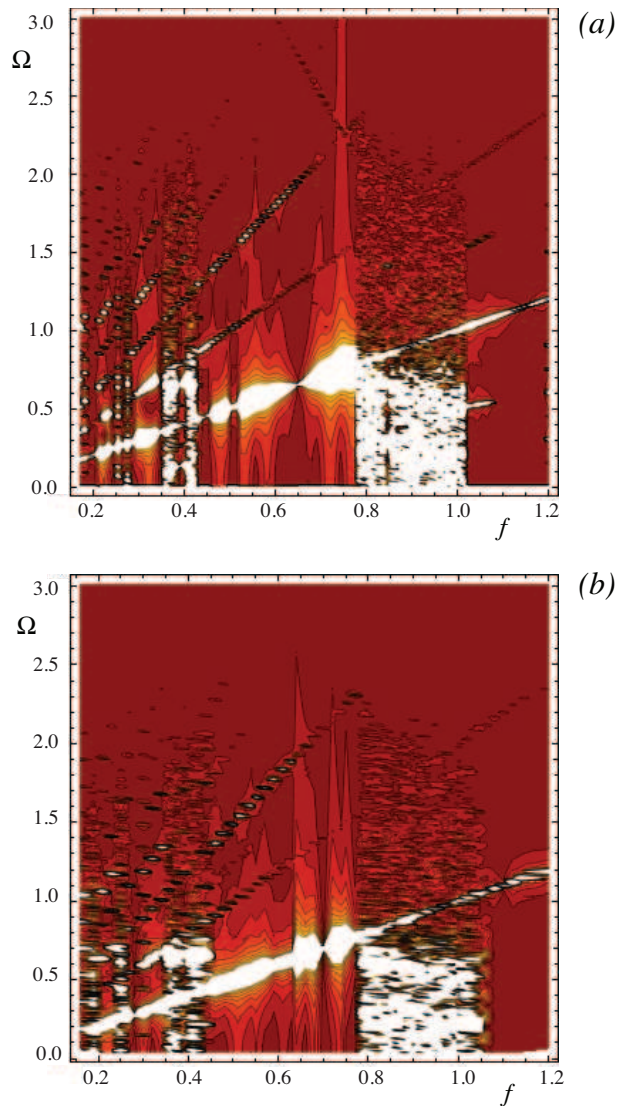


FIG. 10. Spectrograms, (a) numerical, (b) experimental.

swamp the frequency spectra of the response. Of course, the presence of noise also makes the determination of LE's more difficult. However, the system noise level is not atypical of periodically forced low-order mechanical systems.

In order to verify the above bifurcation diagrams, several other methods were also applied. Figure 13 shows numerical and experimental one-parameter amplitude bifurcation diagrams over the same frequency range. The dashed vertical lines again show the locations of the four samples in Fig.'s 6 to 9. The ordinate axis shows the amplitude difference between a peak and the following valley in the time series of $\theta(t)$. To develop this plot an individual simulation/test was run for each forcing frequency (400 simulations numerically, 58 tests experimentally). The system was again allowed to run for an initial period of time to allow transients to decay. For a periodic time series all of the data points will lay on top

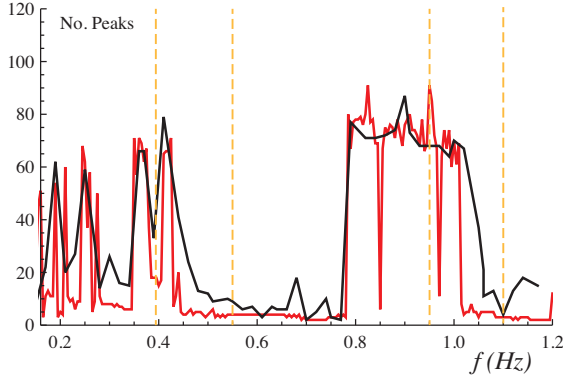


FIG. 11. Plot of peak counts of DFT, threshold = 1%. Numerical (red), experimental (black).

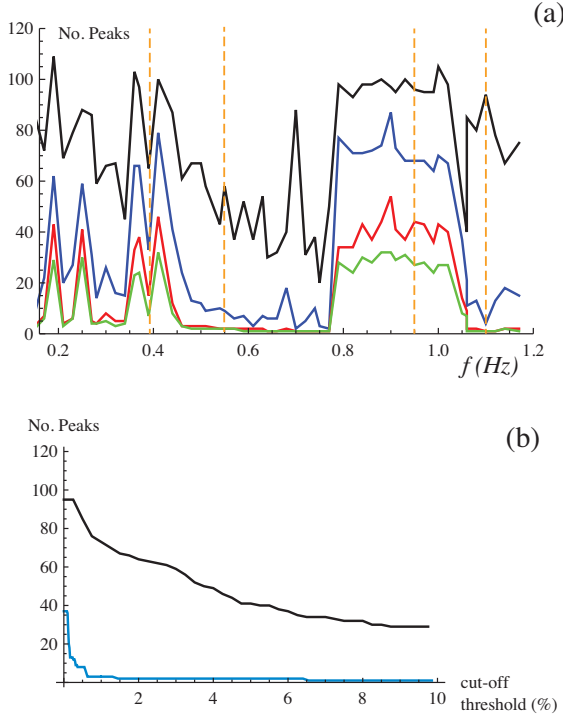


FIG. 12. Sensitivity of peak counts to cut-off threshold. Threshold = 0% (black), 1% (blue), 5% (red), 10% (green).

of one another, while for a chaotic time series they will be scattered about. It is interesting in the chaotic band between approximately $f = 0.8\text{Hz}$ and $f = 1.0\text{Hz}$ that there is a strip of mid-range $\Delta\theta$ values that are never visited. This makes sense since in a system with a periodic potential the oscillations will either be within a single potential well and therefore small, or crossing between the two wells and therefore large. The agreement between the experimental and numerical results is excellent and they both show a resonant jump in amplitude near $f = 0.65\text{Hz}$ which is typical of 'softening' spring systems²³. There is also excellent agreement with the peak count plots.

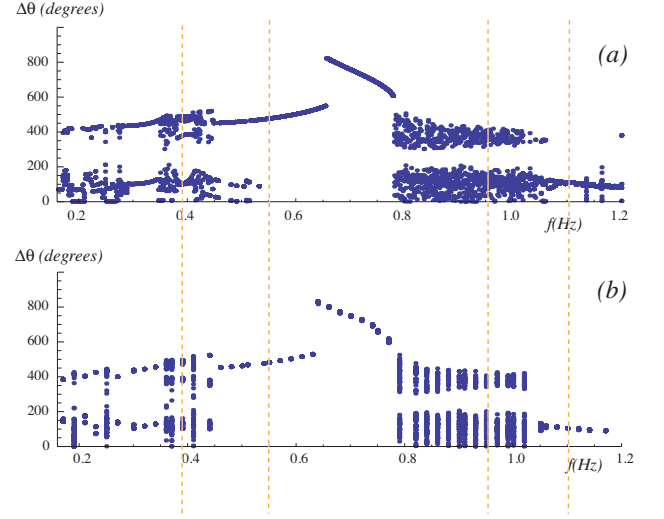


FIG. 13. Amplitude bifurcation diagram, (a) numerical, (b) experimental.

Figure 14 shows the numerically obtained largest LE bifurcation diagram for the same parameter range. The curve was obtained by simulating the equation of motion, and calculating the largest LE using the method in⁵. Once again the dashed vertical lines denote the four samples in Fig.'s 6 to 9. The regions of positive largest LE agree well with the regions of chaos in Fig.'s 10 to 13. Note that for a nonchaotic trajectory the true largest LE of a temporally forced system is zero since the time state is non-converging. However since the numerical method has direct access to each state one may remove time from the divergence calculations and therefore obtain negative LE's.

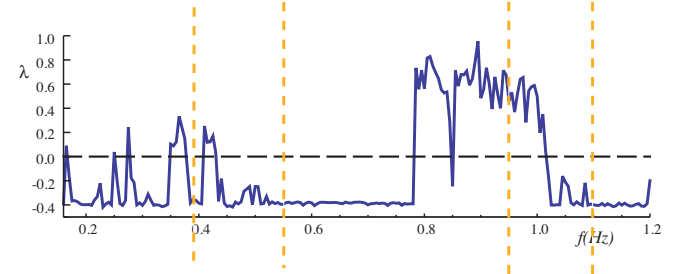


FIG. 14. Numerical LE bifurcation diagram.

Determination of LE's from experimental data is a sensitive procedure. In calculating LE's numerically from an equation of motion one has the ability to either normalize and restart the analysis of divergence rates of nearby trajectories or to simply linearize the divergence rates. This makes it possible to calculate the LE directly by its definition as an exponential divergence rate. This is not possible with experimental data. One useful method however, especially with small data sets, is discussed in⁷. In this method the phase portrait is first reconstructed and then the nearest neighbor is found for each data

point. Then the pairs of nearest neighbors are stepped forward in time and their divergence rate is monitored. Finally the average of the logarithm of the divergence rate of nearest neighbors is taken over all sets of pairs at each point in time (relative time for each pair). In the best case there is a relatively long lasting period of time in which the plot of the logarithm of the divergence rate is approximately linear. The slope of the linear portion is of course the divergence rate, and therefore the LE of the system. Of course, as two nearby trajectories grow far apart the dynamics of their divergence rate will become more and more nonlinear and hence the logarithm of the divergence will eventually lose its linearity. The time scale over which the linear behaviour occurs and the largest LE may be calculated is highly system and parameter dependent making it very difficult to tune for a hands-off analysis over parameter space. For many systems, especially autonomous or low dimensional systems, the nearest neighbors divergence approach works very well for calculating LE's (See Appendix). However for the forced oscillator studied herein the results were less impressive. Figure 15 shows the logarithm of the divergence rate of initially nearby trajectories as a function of time for two different sets of forcing parameters. Part (a) is for the chaotic response in Fig. 9 while part (b) is for the periodic response in 7. The red lines (left vertical axes) shows the average of the Logarithm of the divergence of nearest neighbors for experimental data, while the blue lines (right vertical axes) shows the same (using the same method) on numerically simulated data from the equation of motion. The experimental curves have a much larger y -intercept as the nearest neighbors are much farther apart with experimental data. The slope of the dashed lines is equal to the exact LE's, that is the LE obtained directly from the equation of motion earlier. This dashed line was placed artificially and its y -intercept is not particularly meaningful. The time lag (for this case it was $1/4$ of the forcing period) which is used to reconstruct the phase portrait can effect the result. However the curves in Fig. 15 were relatively insensitive to this parameter, a fact which is also mentioned in⁷. It is clear from part (a) that tuning the time scale over which to calculate the LE would be difficult for this system as there is no clear linear portion of the line. For part(b) one would hope that the experimentally obtained LE for a periodic trajectory would be either negative, zero, or at least much smaller than those for a chaotic response. This is the case for the blue line, but the experimental data still appears to have a positive slope. It is likely that this is due to the real noise in the system, as the phase portrait in Fig. 7 is clearly periodic.

In general it is not immediately clear whether the heuristic method or the LE approach require longer time series to obtain a good result, however for this system it appears that the heuristic method yields better results. The experimental time series used in this system were all 100s long, which is approximately 16 forcing cycles in the vicinity of the 1 Hz forcing region of the bifurca-

tion diagrams. This was done because a large number of parameters were investigated. To the naked eye it is relatively easy to distinguish between periodic and chaotic responses over this number of cycles. This is also usually enough cycles to capture quasi-periodicity on the DFT of the response, as long the Nyquist frequency is high enough to capture all of the dominant frequencies (the sampling rate used was 200 Hz which was well above any contributing frequencies in the response). However, especially for a chaotic response, this may not provide enough pairs of nearby neighbors with which to yield a good approximation of the LE.

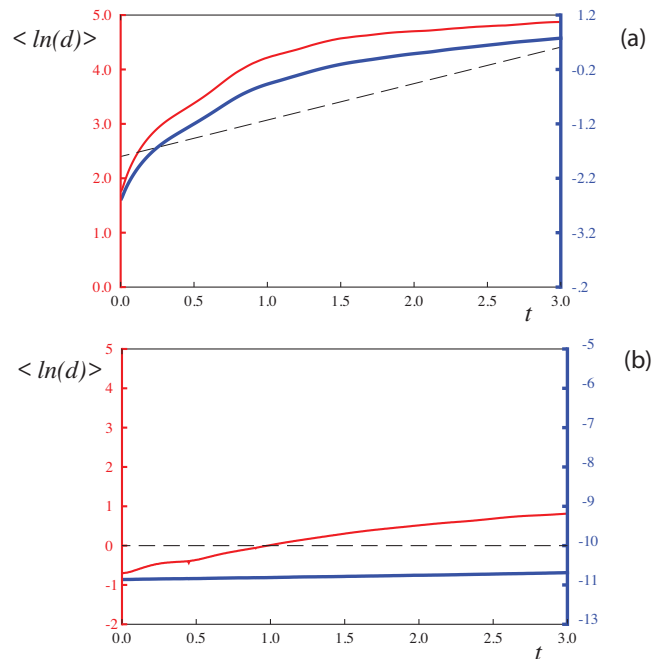


FIG. 15. Average of logarithm of divergence of nearest neighbors, $L = 5.5\text{cm}$, (a) $f = 0.95\text{Hz}$, (b) $f = 0.55\text{Hz}$.

In order to obtain the boundaries between chaotic and periodic response in two-parameter space, (f, L) , one can plot the peak count as a contour plot versus any two parameters. Figure 16 shows the results from numerical LE calculations where regions colored orange indicate parameters with a chaotic response ($LE > 0$) while regions in red indicate a periodic response ($LE < 0$). The horizontal line at $L = 5.5\text{cm}$ denotes the forcing amplitude of the one-parameter bifurcation diagrams presented earlier. The resolution of the plot is 200 points in the frequency axis and 200 in the forcing amplitude axis yielding 40,000 total points.

The two-parameter plot is where the heuristic method is especially useful over the standard spectrogram. Figure 17 shows the results of the two-parameter investigation using the heuristic method on both numerically simulated and experimental data. The peak count cut-off threshold used was 1% and 5% respectively for the numerical and experimental cases. Selection of these values was aided by referencing Fig.'s 11 and 12. The numerical

threshold could be chosen smaller since the only source of 'noise' is due to the numerical errors. To allow for a direct comparison with LE's it was decided to set a second threshold peak count number separating classification as either chaotic or periodic. This was made relatively easy due to the clear dichotomy in the peak counts between chaotic and periodic responses shown earlier. This second threshold was chosen to be 40 and 20 peaks respectively for the numerical and experimental cases. These values were chosen as points approximately mid-way between typical chaotic and periodic response peak counts by referencing the one-parameter peak count plots in Fig.'s 14 and 15. The resolution for part (a) is 40,000 data points (same as Fig. 16) while the resolution for the experimentally obtained plot in part b) is only 58×15 . The agreement is once again excellent, as is the agreement between the LE's and the heuristic method. It is important to note that the standard LE approach also frequently requires calibration via visual inspection for experimental data. The run time over which to determine the LE is especially difficult to perform automatically and is frequently somewhat ambiguous as seen in Fig. 15.

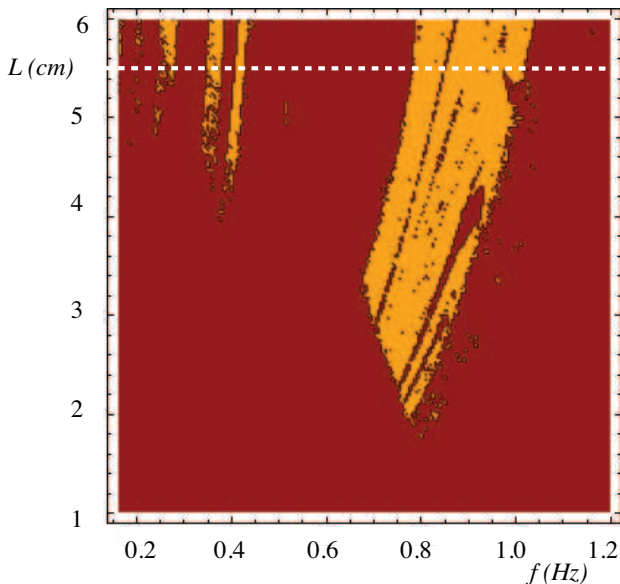


FIG. 16. Chaotic boundaries in parameter space: numerical LE's.

IV. CONCLUSIONS

A heuristic method for identifying chaos is developed and tested both numerically and experimentally on a nonlinear mechanical oscillator. The method is used to create several bifurcation diagrams and shows excellent agreement with numerically obtained Lyapunov exponents, much better in fact than the experimentally obtained Lyapunov exponents.

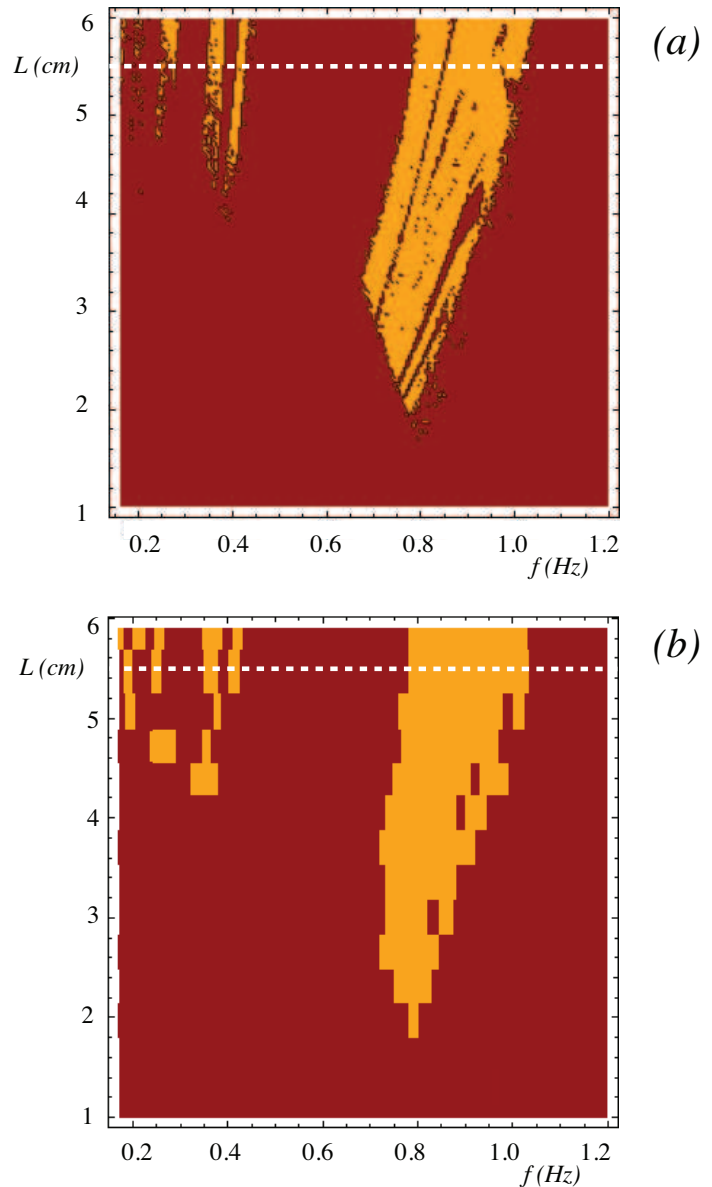


FIG. 17. Chaotic boundaries in parameter space: heuristic method. (a) Numerical, (b) experimental.

ACKNOWLEDGMENTS

The authors gratefully acknowledge the support of the US Air Force grant FA9550-09-1-0204, and NSF-CMMI-09-27186.

Appendix: The Lorenz Equations

In order to show the applicability of the method to other systems it has been applied numerically to the familiar Lorenz equations^{24,25}

$$\begin{aligned}\dot{x} &= \sigma(y - x), \\ \dot{y} &= rx - y - xz, \\ \dot{z} &= xy - bz,\end{aligned}\tag{A.1}$$

with parameters (σ, r, b) and states (x, y, z) . Figure 18 shows a typical periodic and chaotic response for the Lorenz equations. Figure 19 shows the chaotic boundaries in (σ, r) space with $b = 8/3$ obtained using the heuristic method and the using LE's. The white dots shown in the figure denote the location of the samples shown in Fig. 18. The heuristic method was carried out using a peak count cut-off threshold of 1% of the maximum peak.

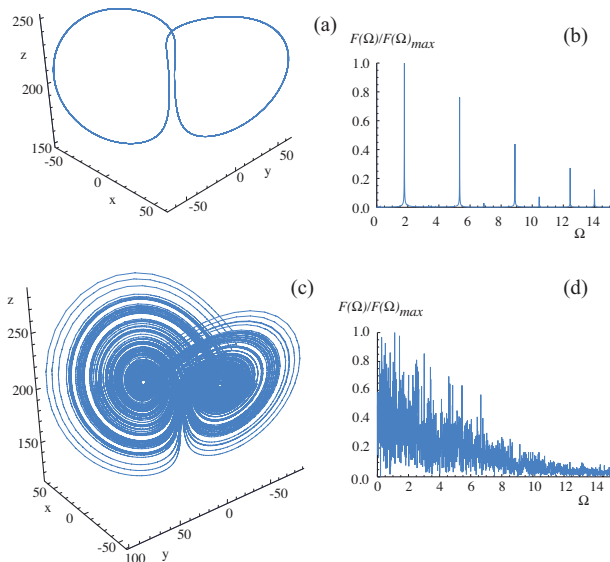


FIG. 18. Sample responses (numerical) from the Lorenz equations, $r=200$, $b=8/3$, (a) $\sigma = 100$, (b) $\sigma = 25$.

The experimental nearest neighbors divergence method works better on the Lorenz system than it does on the forced oscillator (Fig. 12). Figure 20 shows the results of the nearest neighbors approach versus direct calculation of LE's. These are 1D slices as indicated by the horizontal dashed lines in 19, i.e. three chaotic zones when $r = 500$, and two when $r = 200$. Once again the nearest neighbors method here is applied to data simulated from the equation of motion, and then compared to the direct method of LE calculation. Parts (a) and (b) show the average logarithm of the divergence of nearest neighbors for two different sets of parameters located in two different bands of chaos for $r = 500$. The time scale over which the LE may be calculated (the linear portion) is much easier to identify

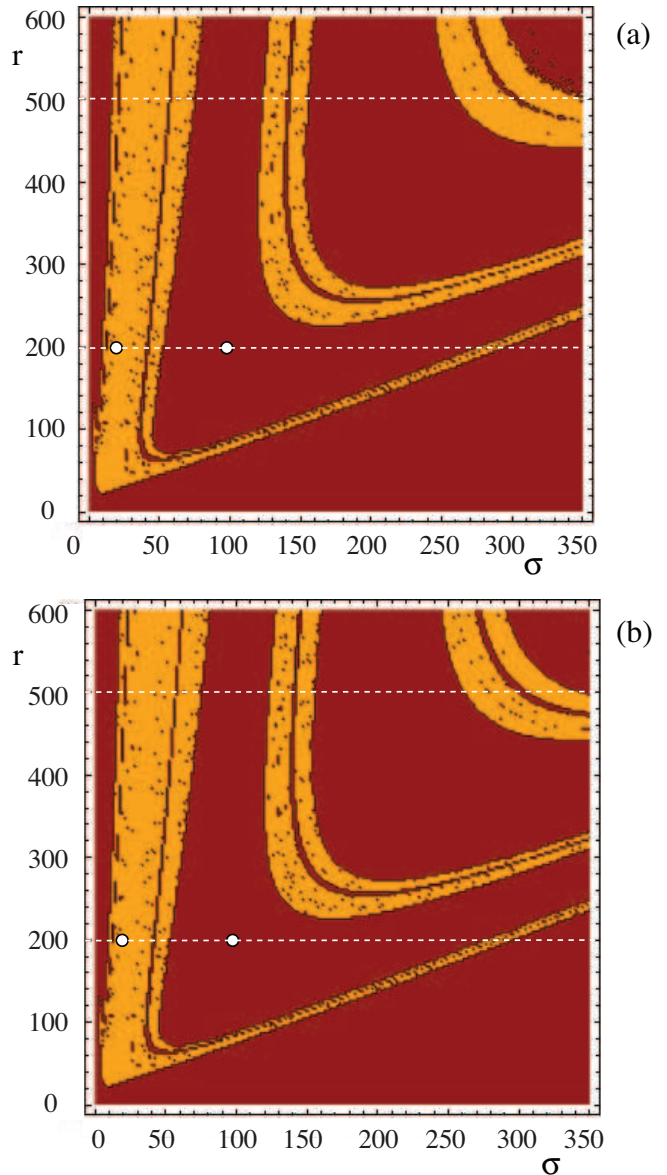


FIG. 19. Chaotic boundaries in two-parameter space for the Lorenz system for $b = 8/3$. (a) Heuristic method, (b) LE's.

and appears to be much more stable for the Lorenz system. The dashed lines superimposed on each plot has the slope of the LE which was obtained by the direct numerical approach. Part (c) shows a comparison of the one-parameter LE bifurcation plots obtained using the experimental approach (black line) and the direct numerical approach (red line) for $r = 500$, where the two vertical dotted lines indicate the location of parts (a) and (b). Finally part (d) shows the same comparison of the bifurcation diagrams, but this time for $r = 200$, while the two vertical dashed lines now denote the location of the phase portraits in Fig. 18. For the experimental data approach the LE was calculated by obtaining the approximate slope of the logarithm of the divergence plot from $t = 0s$ to $t = 0.3s$ as this

appears to be reasonably a stable zone where the line remains nearly linear. The curves were all obtained with 50s simulations and 5000 data points and the time lag used for phase space reconstruction was 11 time steps. These are all the same parameters that were used in⁷. The difference in the magnitude between the two methods could likely be reduced by a more thorough calibration of the time lag and slope measurement time span, however the agreement on the locations of the bifurcations between periodic and chaotic behaviours is excellent.

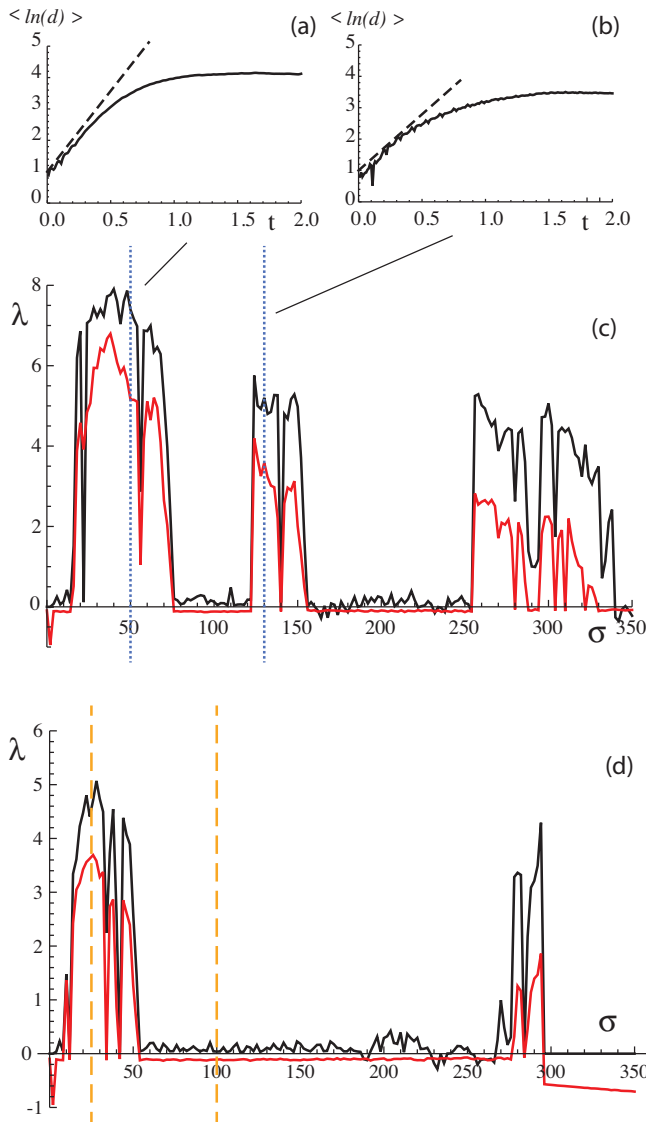
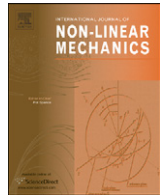


FIG. 20. Comparison of LE calculation methods for $b = 8/3, r = 500$ for (a),(b),(c), and $r = 200$ for (d). Parts (a) $\sigma = 50$, and (b) $\sigma = 130$, show the average logarithm of the divergence rate of nearest neighbors. Parts (c) and (d) show bifurcation diagrams from the direct numerical method (red), and the experimental approach (black).

- ¹H. Kantz and T. Schreiber, *Nonlinear time series analysis* (Cambridge University Press, UK, 1997)
- ²E. Ott, *Chaos in dynamical systems (2nd ed.)* (Cambridge University Press, USA, 2002)
- ³J. C. Sprott, *Chaos and time series analysis* (Oxford University Press, USA, 2003)
- ⁴V. Oseledets, "A multiplicative ergodic theorem: Lyapunov characteristic numbers for dynamical systems," *Transactions of the Moscow Mathematical Society* (1968)
- ⁵W.-C. Xie, *Dynamic stability of structures* (Cambridge University Press, USA, 2006)
- ⁶A. Wolf, J. B. Swift, H. L. Swinney, and J. A. Vastano, "Determining Lyapunov exponents from a time series," *Physica D: Nonlinear Phenomena* **16**, 285–317 (1985)
- ⁷M. T. Rosenstein, J. J. Collins, and C. J. D. Luca, "A practical method for calculating largest Lyapunov exponents from small data sets," *Physica D: Nonlinear Phenomena* **65**, 117–134 (1993)
- ⁸K. Briggs "An improved method for calculating Liapunov exponents of chaotic time series," *Physics Letters A* **151**, 27–32 (1990)
- ⁹G.-Q. Wu, N. M. Arzeno, L.-L. Shen, D.-K. Tang, D.-A. Zheng, N.-Q. Zhao, D. L. Eckberg, and C.-S Poon, "Chaotic signatures of heart rate variability and its power spectrum in health, aging and heart failure," *Plos One* **4**, e4323 (2009)
- ¹⁰Y.-C. Lai, Z.-H. Liu, L. Billings, and I. B. Schwartz, "Noise-induced unstable dimension variability and transition to chaos in random dynamical systems," *Physical Review E* **67**, (2003)
- ¹¹C.-S. Poon and M. Barahona "Titration of chaos with added noise," *Proceedings of the National Academy of Sciences* **98**, 7107–7112 (2000)
- ¹²T. Higuchi, "Approach to an irregular time series on the basis of fractal theory," *Physica D: Nonlinear Phenomena* **31**, 277–283 (1988)
- ¹³P. Bergé, Y. Pomeau, and C. Vidal, *Order within chaos: towards a deterministic approach to turbulence* (Wiley, USA, 1986)
- ¹⁴G. L. Baker and J. P. Gollub, *Chaotic Dynamics - An Introduction, Second Edition* (Cambridge University Press, USA, 1996)
- ¹⁵J. P. Gollub and H. L. Swinney, "Onset of Turbulence in a Rotating Fluid," *Phys. Rev. Lett.* **35**, 927–930 (1975)
- ¹⁶S. Blacher and J. Perdang, "The power of chaos," *Physica D: Nonlinear Phenomena* (1981)
- ¹⁷R. Wiebe, L. N. Virgin, and T. P. Witelski, "A parametrically forced nonlinear system with reversible equilibria," *In Press - International Journal of Bifurcations and Chaos* (2011)
- ¹⁸R. Wiebe and L. N. Virgin, "On the identification of chaos from frequency content," *Proceedings of the 2011 ASME IDETC/CIE Conference*, Washington DC, August (2011)
- ¹⁹L. N. Virgin, J. M. Nichols, and S. T. Trickey, "A note on the response spectrum map," *International Journal of Bifurcation and Chaos* **13**, 1337–1341 (2003)
- ²⁰T. D. Rossing and J. R. Hull, "Magnetic levitation," *The Physics Teacher* **December**, 552–562 (1991)
- ²¹W. T. Thomson, *Theory of vibration with applications (2nd. ed.)* (Prentice Hall, USA, 1981)
- ²²W. H. Press and S. A. Teukolsky, and W. T. Flannery, *Numerical recipes: the art of scientific computing (3rd. ed.)* (University Press, USA, 2007)
- ²³L. N. Virgin, *Introduction to Experimental Nonlinear Dynamics* (Cambridge University Press, USA, 2000)
- ²⁴E. Lorenz, "Deterministic nonperiodic flow," *Journal of Atmospheric Sciences* **26**, 636–646 (1963)
- ²⁵S. H. Strogatz, *Nonlinear Dynamics and Chaos, With Applications to Physics, Biology, Chemistry, and Engineering* (Perseus Books Publishing, USA, 1994)



A lower bound on snap-through instability of curved beams under thermomechanical loads

Ilinca Stanciulescu^{a,*}, Toby Mitchell^b, Yenny Chandra^a, Thomas Eason^c, Michael Spottswood^c

^a Rice University, Department of Civil and Environmental Engineering, 6100 Main Street, Houston, TX 77005, USA

^b University of California at Berkeley, Department of Civil Engineering, Berkeley, CA 94720, USA

^c Air Force Research Laboratory, Structural Sciences Center, 2790 D. Street, WPAFB, OH, USA

ARTICLE INFO

Article history:

Received 24 September 2010

Received in revised form

8 August 2011

Accepted 9 October 2011

Keywords:

Snap-through

Finite element

Curved beam

Solid (continuum) elements

Thermomechanical loads

ABSTRACT

A non-linear finite element formulation (three dimensional continuum elements) is implemented and used for modeling dynamic snap-through in beams with initial curvature. We identify a non-trivial (non-flat) configuration of the beam at a critical temperature value below which the beam will no longer experience snap-through under any magnitude of applied quasi-static load for beams with various curvatures. The critical temperature is shown to successfully *eliminate snap-through in dynamic simulations at quasistatic loading rates*. Thermomechanical coupling is included in order to model a physically minimal amount of damping in the system, and the resulting post-snap vibrations are shown to be thermoelastically damped. We propose a test to determine the critical snap-free temperature for members of general geometry and loading pattern; the analogy between mechanical prestress and thermal strain that holds between the static and dynamic simulations is used to suggest a simple method for reducing the vulnerability of thin-walled structural members to dynamic snap-through in members of large initial curvature via the introduction of initial pretension.

© 2011 Elsevier Ltd. All rights reserved.

1. Introduction

Thin structural members can dynamically jump between multiple equilibrium configurations when subjected to mechanical forces, acoustic vibrations, and thermal loads like those encountered by aerospace vehicles in extreme operating conditions. This process, commonly referred to as snap-through, can cause large-amplitude structural vibrations, induce fatigue, and lead to global instability. Such vibrations can have a chaotic pattern and therefore can be difficult to control [1]. Avoiding snap-through is therefore highly desirable in the design of thin-walled structures such as aircraft and spacecraft.

In this paper, the existence of a critical temperature below which an initially curved beam will no longer experience snap-through at *any* applied quasi-static load level is demonstrated. This temperature provides a *lower bound* below which snap-through instability no longer occurs. This temperature also corresponds to a *non-trivial* (that is, non-flat) deformed beam configuration, a fact that is not apparent through methods used to characterize snap-through that are limited to modeling small deflections. We argue that such a limit can be obtained for a

variety of static loads and that it also reduces the amplitude of the oscillations when loads are applied at dynamic rates. Through numerical experiments we show this limit to be found at states characterized by specific properties associated with the energy of the system and the directional derivatives of this energy function.

Experimental characterizations of snap-through under mechanical vibrations and combined thermal and mechanical loads have existed for several decades [2–4], but numerical modeling of snap-through remains an area of active research. In the general case, snap-through involves combined flexural, shear, and normal stresses, large time varying deflections and rotations, and thermal effects. Non-linear coupling between these effects makes snap-through challenging to model accurately. An extensive literature exists on the subject, with models describing different degrees of geometric non-linearity [5,6], material non-linearity [7–9], thermal and acoustic loading [10–12], and various combinations of these factors [13,14].

Previous research on snap-through falls into three general categories: (1) limited-deflection models (based on the von Karmann or Duffing equations for plates), (2) elastica models (based on specialized analytical techniques going back to Euler), and (3) non-linear (finite-deformation) finite element models.

The first category suffers from the most significant limitation: these models can only describe member deflections of less than 2.5 times the member thickness [5]. This is especially problematic because large initial curvatures that may be present by design,

* Corresponding author. Tel.: +1 713 348 4704; fax: +1 713 348 5268.
E-mail address: ilinc@rice.edu (I. Stanciulescu).

e.g., in a rocket booster hull or aircraft wing, will lead to larger snap-through loads and therefore more severe and damaging post-snap vibrations, none of which can be modeled with limited deflection formulations.

Elastica methods are valid at a theoretically unlimited range of deflections and initial curvatures, at the cost of increased mathematical complexity. These techniques have only recently been extended to the solution of thermal and snap-through problems [15–17]. This is most likely due to the increased ease of solving the equations numerically, e.g., by shooting methods [18,19]. Although there is no apparent limitation to obtaining the results discussed in this paper by elastica methods (other than possible limitations to particular instances of the theory, e.g., the common omission of shear strain), they are not as well-developed for general classes of problems as non-linear finite element methods.

Non-linear finite element methods are the most general of the methods available to model snap-through, an advantage for which they sacrifice the direct, problem-specific analytical insight that is available via the first two methods. This lack of transparency is more than compensated by the versatility to model geometric non-linearity, thermomechanical coupling, large strains, material non-linearity, fluid–structure interaction in aircraft, etc.

The non-linear finite element method is chosen for this study; it is capable of including the full range of non-linearities that influence snap-through and can easily model large deflections. Beam and shell models, usually the most computationally efficient choice for finite element modeling of thin structural members, always involve some simplifications of the underlying three-dimensional kinematics that can lead to artificial stiffness under particular load states (locking). These kinematic assumptions that are built into the formulation of structural elements can lead to inaccurate solutions [20]. In this work we avoid such issues as well as the locking sometimes present when linear elements are used by choosing to work with three-dimensional (solid) quadratic elements only. In this paper, the numerical simulations are performed with the Finite Element Analysis Program (FEAP), an open source research code, which provides a framework for finite element simulations where we can formulate and implement additional elements, constitutive models and solution schemes via user subroutines. The formulations utilized for the analysis discussed in this paper are a mix of FEAP original elements and user routines [21].

By *thermomechanical coupling* we refer only to the coupling between elastic deformation and thermal effects via the thermal strain terms in the equations of mechanical equilibrium and the structural elastic heating term in the heat equation. Although thermoelastic coupling is present in all materials, it is often neglected; however, for large-amplitude vibrations, the thermal gradient induced between the compressive and tensile fibers of a vibrating member due to purely elastic deformation results in significant heat conduction and therefore loss of energy via *thermoelastic damping*. We do not include any other mechanisms of dissipation besides thermoelastic damping, so the damping in our study is *physically minimal*, and the resulting vibrations are exaggerated relative to real physical systems.

In many studies [22,23], thermal strain due to applied temperature is included *without* modeling thermoelastic coupling: temperature changes are thus treated as a simple mechanical expansion or contraction of the material. This can be useful in tracing static solution paths, and may also give information about the temperature-sensitivity of a particular structure, but the absence of thermoelastic coupling can impact the accuracy of dynamic simulations, especially as amplitudes of vibration become large. We employ the strain-only method in our static simulations, but move to full coupling in order to capture relevant dynamic coupling effects.

Modeling of thermomechanical coupling also requires the selection of an appropriate thermomechanical material constitutive law. A hyperelastic constitutive law based on a modified neo-Hookean material that is appropriate for metals has been proposed in previous studies [24]. Since we will be primarily concerned with metals, the modified thermomechanical neo-Hookean material law is appropriate and will be valid at a much larger range of strains than the thermomechanical St. Venant–Kirchhoff law.

Failure to account for any of the above modeling concerns can significantly impact the accuracy of dynamic simulation results. The formulation adopted for this study accounts for the geometric non-linearity, large strains, and thermomechanical coupling effects required to describe snap-through. It is a non-linear finite element formulation that uses the adiabatic staggered scheme and the constitutive law detailed in [24] and quadratic hexahedral (or tetrahedral) elements.

The initial boundary value problem is formulated as follows: For all $t \in \mathbb{I}$ find the motion (ϕ) and temperature (T) fields such that

$$\begin{aligned} \rho_0 \frac{\partial^2}{\partial t^2} \phi &= \text{div } \mathbf{P} + \mathbf{b}, \\ c\dot{T} &= \mathcal{D} - \mathcal{K} - J \text{div}[\mathbf{q}/J] + \mathcal{R}, \end{aligned} \quad (1)$$

with boundary conditions $\mathbf{P}\mathbf{n}_0 = \bar{\mathbf{t}}$ on $\Gamma_\sigma \times \mathbb{I}$, $\phi = \bar{\phi}$ on $\Gamma_\phi \times \mathbb{I}$, $\mathbf{q}\mathbf{n}_0 = \bar{\mathbf{q}}$ on $\Gamma_q \times \mathbb{I}$, $T = \bar{T}$ on $\Gamma_T \times \mathbb{I}$ and initial conditions $\phi|_{t=0} = \mathbf{I}$ in $\bar{\Omega}$, $(\partial/\partial t)\phi|_{t=0} = \mathbf{V}_0$ in $\bar{\Omega}$, $T|_{t=0} = T_0$ in $\bar{\Omega}$. $\Omega \subset \mathbb{R}^{n_d}$ is the domain in the reference configuration, n_d is the number of spatial dimensions in the problem, ρ_0 is the reference configuration density, \mathbf{P} is the first Piola–Kirchhoff stress tensor, \mathbf{b} is the prescribed body force, c is the heat capacity, \mathcal{D} is the mechanical dissipation, \mathcal{K} is the heating from the Joule effect [25], \mathcal{R} is the prescribed heat source term, and J is the Jacobian of the deformation. $\bar{\bullet}$ denotes the prescribed value of the quantity \bullet over the appropriate boundary region or at the initial time. The generic problem described here can be completed with a constitutive law prevailing in the body and the Fourier law for heat conduction is assumed to relate the local heat flux \mathbf{q} to the temperature gradient, $\mathbf{q} = -[k\mathbf{1}]\nabla T$, where k is the thermal conductivity and $\mathbf{1}$ is the identity tensor. For the purpose of this paper, the constitutive law is assumed to have temperature-dependent constitutive moduli. After a spatial discretization is applied (e.g., finite element) the system (1) can be expressed as a system of ordinary differential equations with two coupled partitions: mechanical (second order) and thermal (first order).

For the transient solution we use the adiabatic staggered scheme for coupled thermoelastic boundary value problems developed in [24]; this approach splits the solution into partitions such that the dissipative property of the original problem is maintained in the partitioned problem. The scheme consists of (1) a standard finite deformation mechanical phase, formulated such that it is solved at *constant entropy*, and (2) a heat conduction phase, formulated such that it is solved at *fixed deformation*.

We also adopted the constitutive law from [24, p. 760, Eqs. (82)–(83)], for a regularized compressible neo-Hookean material. This is a law that performs well for metals and is given by the thermomechanical strain energy density function:

$$\Psi(\mathbf{C}, \Theta) = W(\bar{\mathbf{C}}) + U(J) + M(J, \Theta) + T(\Theta), \quad (2)$$

where W , U , M , and T are the mechanical deviatoric, mechanical volumetric, thermomechanical coupling, and thermal-only terms respectively, given by

$$W(\bar{\mathbf{C}}) = \frac{1}{2} \mu (\text{tr}(\bar{\mathbf{C}}) - 3) = \frac{1}{2} \mu (J^{-2/3} \text{tr}(\mathbf{C}) - 3),$$

$$U(J) = \frac{1}{2} K (\ln J)^2,$$

$$M(J, \Theta) = -3K\alpha(\Theta - \Theta_{ref})\ln J,$$

$$T(\Theta) = \rho c_m \left[(\Theta - \Theta_{ref}) - \Theta \ln \left(\frac{\Theta}{\Theta_{ref}} \right) \right],$$

where \mathbf{C} is the right Cauchy–Green tensor, μ is the shear modulus, c_m is the mass heat capacity, Θ_{ref} is the reference temperature, K is the bulk modulus, α is the coefficient of thermal expansion and J is the Jacobian of deformation.

For the detailed derivation of the components of the finite element formulations utilized in this work, the interested reader is referred to [26].

The rest of the paper is organized as follows. In Section 2 we describe the geometry of the system under consideration and briefly describe the solution methods utilized to retrieve equilibrium paths. Section 3 is dedicated to numerical experiments that trace such equilibrium paths. In this section, we identify special equilibrium configurations corresponding to boundaries in the parameter space that separate domains with different stability behaviors. Among these, the quasi-static temperature limit that we will refer to as monotonic, i.e., that value of the temperature below which the equilibrium path is a monotonic curve, and snap-through is no longer encountered. Section 4 demonstrates, through a variety of transient simulations, that the monotonic temperature also identifies a limit below which the amplitude of the dynamic oscillations is drastically reduced and asymptotically reaches 0 at temperatures in the neighborhood of the quasi-static limit. Section 5 provides a generalization of the concept of monotonic temperature and shows that information regarding such stability limits is no longer available when some specific finite element formulations (e.g., the Timoshenko beam) are utilized. When kinematic approximations such as those used by the Timoshenko beam are used, information available in the higher derivatives of the energy is lost in such formulations.

2. Static analysis of a curved beam

A planar curved beam described by an arc of a circle is chosen as the test problem to explore the effect of applied temperature and initial beam curvature on snap-through. The problem is solved in two phases (mechanical and thermal). The beam geometry is completely specified by the length of the horizontal projection between the end points L , the projection of the lengths of the supports L_{BC} , and the radius of curvature of the beam R (Fig. 1). The primary load case considered is a point load P in the negative y -direction located at the midpoint between the supports (Fig. 2a). A distributed load p , applied as a uniform force in the negative y -direction on each node of the finite element mesh, is also considered (Fig. 2b).

In simulations, eight different beams were utilized, with R varying from 762 mm (30 in.) to 5080 mm (200 in.). The effect of temperature variation on the load–deflection behavior in the case of larger curvatures was found to be very small, so such test problems were abandoned.

Table 1 summarizes the geometry of the beams: M is the arch rise, $\kappa = 1/R$ is the curvature of the beam, θ is the angle subtended by the beam, and M/h is the ratio of M to the thickness h of the beam. Fig. 3 shows the different initial beam curvatures. For all beams, the projection length is $L = 304.8$ mm (12 in.), the thickness $h = 0.508$ mm (0.02 in.) and the transverse depth $b = 12.7$ mm (0.5 in.). The ends of the beam are held fixed over a length $L_{BC} = 28.7$ mm (1.125 in.) on each end. Material properties are those of steel, given in Table 2.

In this paper we concentrate our attention to a system that is effectively two-dimensional; nevertheless, we use a finite

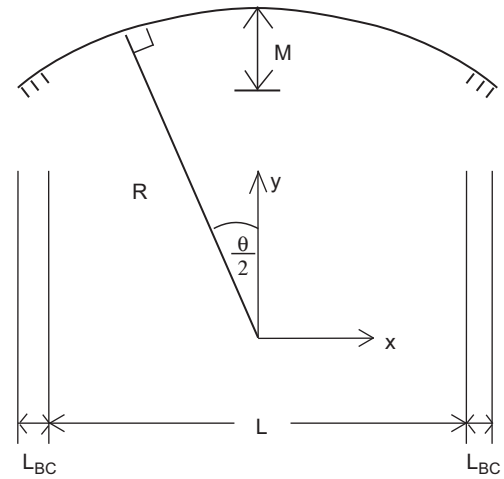


Fig. 1. Geometry for semicircular beam.

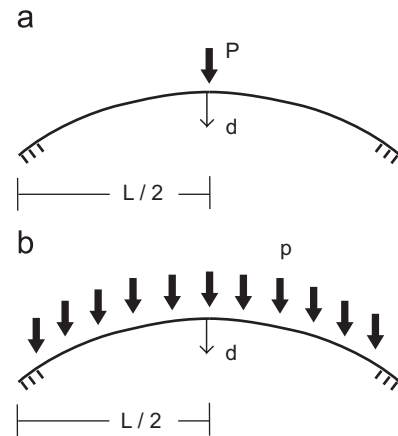


Fig. 2. Concentrated (a) and distributed (b) loads. The point load is the primary case considered.

Table 1
Geometry of curved beams.

Beam	R (mm)	M (mm)	κ (1/mm)	$\theta/2$ (rad)	M/h
1	762.0	21.84	1.312×10^{-3}	0.2400	86.0
2	1270.0	12.99	0.787×10^{-3}	0.1431	51.1
3	1828.8	8.98	0.546×10^{-3}	0.0990	35.3
4	2133.6	7.70	0.469×10^{-3}	0.0850	30.3
5	2438.4	6.74	0.410×10^{-3}	0.0744	26.5
6	3048.0	5.39	0.328×10^{-3}	0.0595	21.2
7	3810.0	4.31	0.262×10^{-3}	0.0475	17.0
8	5080.0	3.23	0.169×10^{-3}	0.0357	12.7

element model with full three-dimensional capabilities. Mesh refinement studies were performed and the level of refinement adequate to accurately capture the snap-through loads lead to a model with approximately 20,000 degrees of freedom. Note that linear elements suffer from shear locking and are not appropriate for snap-through problems, or for any problems involving large deformation. This problem is avoided by using quadratic elements.

The formulation adopted [24] treats the coupling through an adiabatic staggered approach. For the quasistatic simulations of systems under constant temperature presented in the next

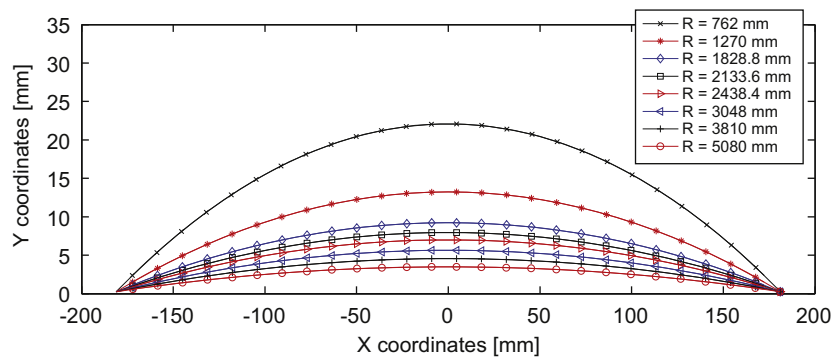


Fig. 3. Initial beam configurations.

Table 2
Material properties of thermoelastic beam.

Property	Symbol	Value	Units
Young's modulus	E	206,483	N/mm ²
Poisson's ratio	ν	0.28	–
Density	ρ	7.834×10^{-9}	N s ² /mm ⁴
Conductivity	k	45.0	N/s K
Specific heat	c_m	434×10^6	mm ² /s ² K
Thermal expansion	α	14×10^{-6}	mm/mm K

section, the mechanical phase is solved in isolation from the thermal phase, treating the applied temperature change as a conservative, purely mechanical expansion or contraction of the beam material. Many other studies have employed this method, but, with a few exceptions [15,16,6], they have been limited to beams of small initial curvature.

The case of the point load along the line of symmetry of the beam provides an easy interpretation of the simulation results. If the symmetry is not broken by a bifurcation, as may occur if the second, asymmetric buckling mode emerges [27], the plots of midpoint deflection d versus load value P will indicate loss of stability and locate the snap-through and snap-back loads at the points where $\partial P/\partial d = 0$. The ability to obtain such information is completely dependent on the symmetry of the problem: in cases without a clear line of symmetry it is no longer possible to obtain information about the snap-through point from the load–deflection curve, and even in the symmetric case of the distributed load this breaks down at heightened temperatures. The simplicity of the symmetric concentrated load case will make it easier to develop insight into the stability behavior of the beam, which we will then need to generalize to cases where important behaviors are no longer apparent from the load–deflection curves.

2.1. Static solution paths

Snap-through is inherently a dynamic phenomenon; since the static equilibrium path is interrupted by an unstable region, as the load is increased, the system must dynamically jump past the unstable region and onto a stable region capable of bearing loads above the snap-through load. Unlike column buckling, there is no stable branch that the system can follow continuously along the equilibrium path. Nevertheless, useful information can be obtained by studying the static solution paths.¹ The lack of inertia allows us to simplify the analysis, since there is no need to

consider the effects of varying loading rates. Moreover, the *unstable* equilibrium path between the stable regions discloses information that is relevant to the dynamic case. We mapped the static equilibrium path by using a pseudo-arc-length procedure to traverse the unstable region.

The non-linear continuum finite element method recovers information that is unavailable from methods based on the beam or plate (restricted kinematics) equations. In particular, there exists a *non-trivial* deformed configuration, at a temperature below the zero-stress reference temperature Θ_{ref} , that will *not* experience snap-through at any applied static load value. The value of this temperature depends on the initial beam geometry, the boundary conditions, and the pattern of applied load. Simulations suggest that any beam that is cooled below this temperature no longer experiences snap-through.

The subsequent sections in this paper are concerned with developing tests to establish this *lower bound on thermoelastic instability* and determining whether this limit, which is derived from purely mechanical considerations, is sufficient to eliminate dynamic snap-through in beam simulations that incorporate full thermomechanical coupling.

3. Numerical experiments. The quasi-static analysis

The zero-stress reference temperature in all simulations is $\Theta_{ref} = 300$ K. Note that the adiabatic staggered scheme is implemented in terms of absolute temperature, so Θ refers to absolute temperature and $\Delta T = \Theta - \Theta_{ref}$ refers to the temperature relative to the reference temperature.

Applied load versus deflection curves were extracted for all beams at various temperature variations ΔT . The $R=762$ mm beam (Fig. 4) shows relatively little variation in load–deflection curve behavior with temperature variation. This plot is representative for the results corresponding to beams with larger curvatures. Fig. 5 is representative for beams with smaller curvatures.

The *key observation* made by examining Fig. 5 (and confirmed for the other six beams for which we do not present the results here) is that for each beam there exists a critical temperature below which the beam no longer experiences snap-through at any load value for a given conservative loading pattern, and exhibits instead a monotonic dependence of the load on deflection. We will simply call this critical value the *monotonic temperature*. The load–deflection curves for this particular boundary value problem also possess a *center point* where all the curves obtained for temperatures above the monotonic temperature intersect; this center point coincides with the limit point where $\partial P/\partial d = 0$ on the *monotonic temperature load–deflection curve itself*. Results for Beam 1 presented in Fig. 4 do not include the monotonic curve since for this particular system the temperature corresponding to it was non-physical (in a mathematical sense however, it does exist).

¹ “Static” refers to the mode of recovery of information on snap-through, not an actual physical scenario.

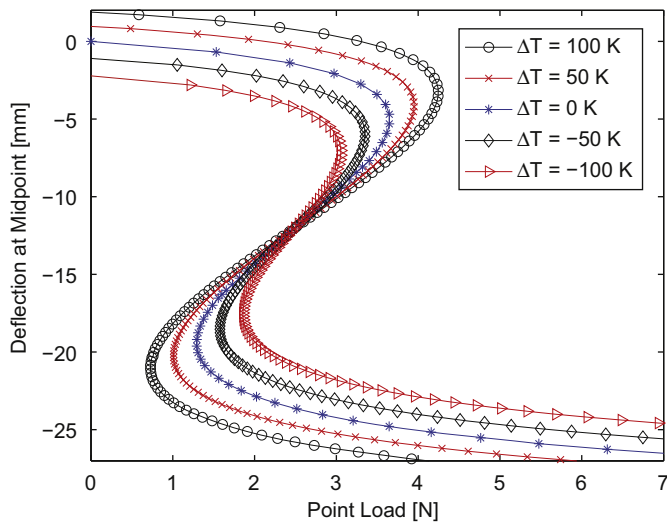


Fig. 4. Beam 1 ($R=762$ mm). Pseudo-arc-length equilibrium paths for different ΔT .

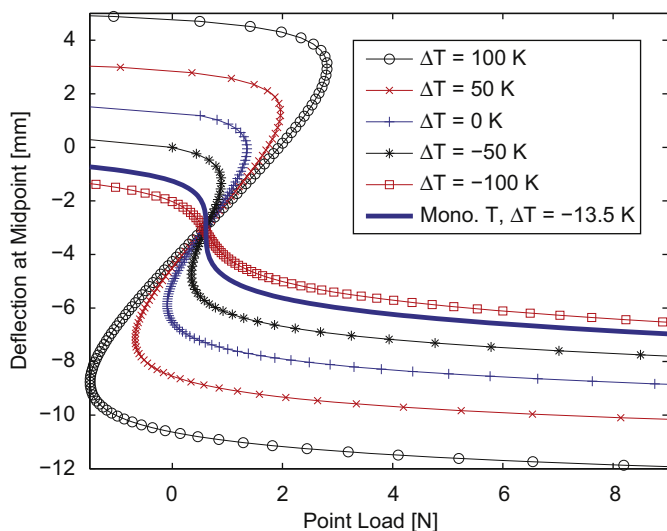


Fig. 5. Beam 6 ($R=3048$ mm). Pseudo-arc-length equilibrium paths for different ΔT .

The method presented in this paper indirectly estimates the lower bound under the assumption of snap-through to a symmetric solution branch. This method relies on tracing the full equilibrium path and on systematic numerical experimentation to identify the temperature for which the above mentioned path is monotonic. In this approach, we sweep through the range of temperatures of interest and check the monotonicity of the solution.

Although apparently similar results have been known for many years [5], note that the snap-free configuration disclosed in such studies is simply the configuration of an unbuckled, initially flat beam or plate, which obviously will not experience snap-through under any magnitude of lateral loading (if no temperature variation is applied). Similarly, the center point in these studies is simply the unloaded initial configuration. Note that if the temperature is raised above a critical buckling temperature, such a member will deform into a curved shape that is itself subject to snap-through [5]. Numerous studies have been devoted to mapping this and the many subsequent post-buckled states [22,28]. Our results are distinct from these studies, since the underlying problem is different: here, rather than an initially

flat plate or beam which must have some initial thermal deformation to experience snap-through, we have an initially curved beam with fixed supports that displays snap-through at the zero-stress reference temperature.

Fig. 6 indicates that the monotonic temperature approaches Θ_{ref} as $\kappa \rightarrow 0$, as expected. For small curvatures the lower bound varies slowly with the curvature. More significant variations are observed for larger curvatures. For very large curvatures the method presented here does not apply since taller arches will buckle asymmetrically. The snap-through loads themselves vary linearly with beam curvature at $\Delta T = 0$ K, a fact that has been determined analytically at small deformation and which appears to continue to hold at large κ ; however, snap-through loads no longer vary linearly with temperature away from the zero-stress reference temperature (Fig. 7). For beams with very low initial curvature, if the temperature is too low, the beam will be straight and in tension and no snap will be experienced.

We can observe several general trends in the results. The relative influence of temperature on the load-deflection behavior of the beam diminishes as the curvature $\kappa = 1/R$ of the beam increases. For the case of $R=254$ mm, the effect of even a temperature change of $\Delta T = +100$ K is so small that the

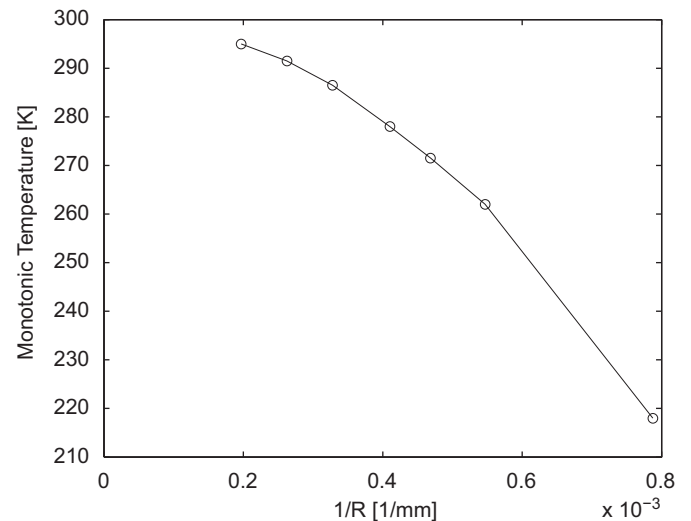


Fig. 6. Monotonic temperature varies non-linearly with curvature.

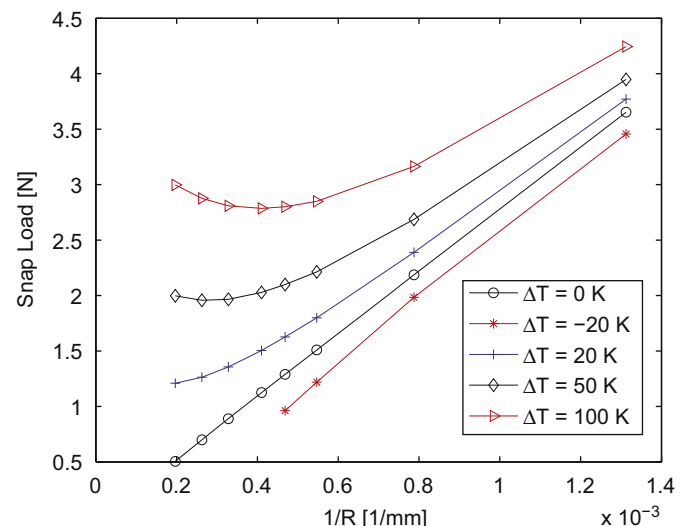


Fig. 7. Snap-through load does not vary linearly with curvature away from $\Delta T = 0$ K.

load–deflection curves for different temperatures would be difficult to distinguish on a graph; the snap-through load at $\partial P/\partial d = 0$ barely changed. By contrast, the influence of temperature on the $R=5080$ mm beam is significant enough that $\Delta T = +100$ K is sufficient to more than triple the snap-through load. This effect can be seen in the decrease in the magnitude of the slope with increasing curvature shown in plots of snap-through load versus temperature in Fig. 8. Note that the effect of temperature will be more significant for materials that are more sensitive to temperature, e.g., aluminum.

Fig. 9 combines these results and shows the snap-through load as a function of both the geometry (radius) and temperature. The contour line represents the snap-through boundary, i.e., the limit (monotonic) temperature beyond which the beam does not experience snap-through. An alternate method that can be used in obtaining the snap load and the monotonic temperature for shallow arches is presented in [29], which shows a very good comparison with the results obtained in this paper.

We also perform a study on the effect of beam width and thickness on the snap-through load and the lower bound temperature. The study shows that varying the beam width (b) for the

same beam thickness (h) does not influence the lower bound temperature; the snap-through load, however, increases linearly as the beam width increases (Fig. 10). As we vary the beam thickness, the snap-through load and the lower bound temperature are both higher for thicker beam (Figs. 11 and 12).

The pseudo-arc-length solution sometimes jumps from the equilibrium path that shows the expected symmetric deformation of the beam (Fig. 13) to another path where the beam deforms asymmetrically (Fig. 14). This asymmetric buckling mode has been previously discussed [5]. While the second buckling mode is negligible if the initial curvature is small enough [27], this mode clearly *cannot* be neglected for large initial beam curvatures.

Nevertheless, a unique lower bound on instability for a given beam and load pattern *can* still be established if the second mode only occurs above the monotonic temperature. If the *entire* unstable region itself is eliminated from the static solution path at the monotonic temperature – including the higher buckling modes – then the lower bound on instability is *unique* for a given load pattern and initial member shape. No static simulation that we conducted contradicted this conjecture, and dynamic simulation results indicated that higher modes tend to be activated at higher temperatures but disappear as temperature is lowered, suggesting that the lower bound is in fact unique.

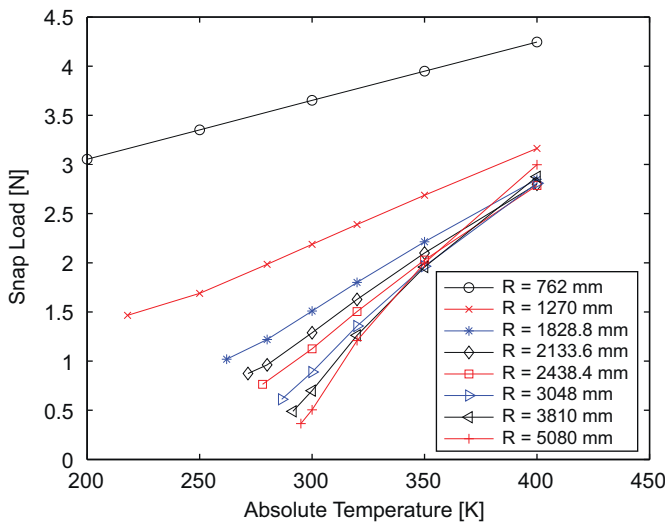


Fig. 8. Snap-through loads for all beams at various temperatures.

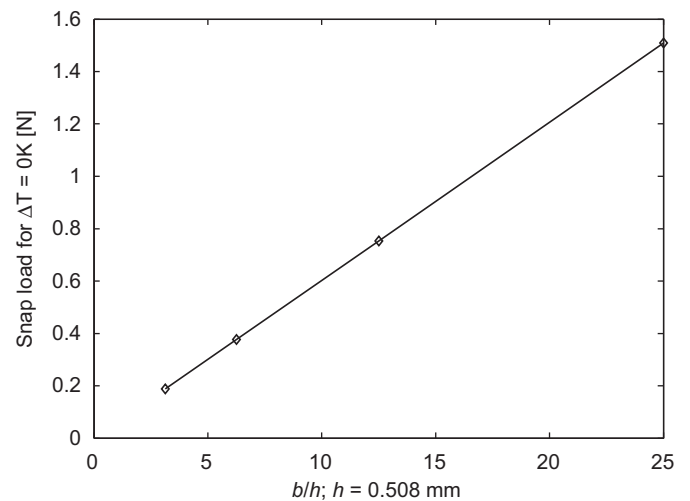


Fig. 10. Snap-through loads for varying b/h with $h=0.508$ mm for all beams.

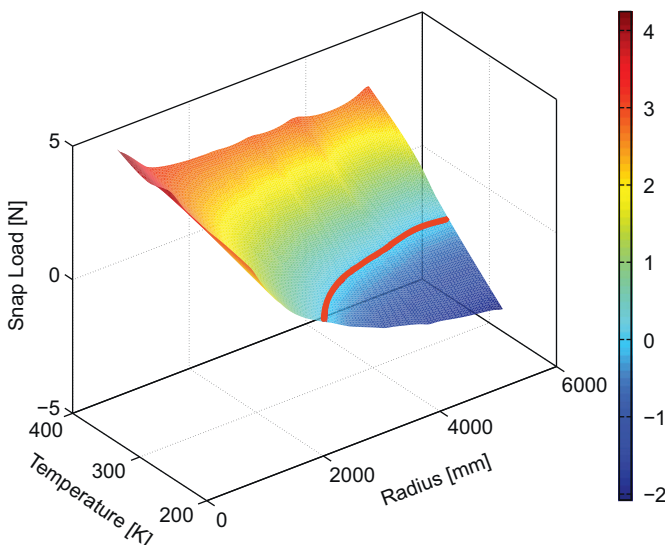


Fig. 9. Snap-through loads versus radius and temperature.

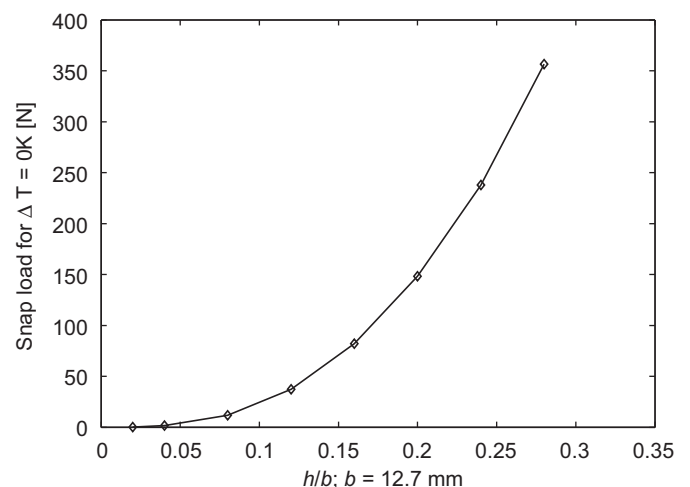


Fig. 11. Snap-through loads for varying h/b with $b=12.7$ mm for all beams.

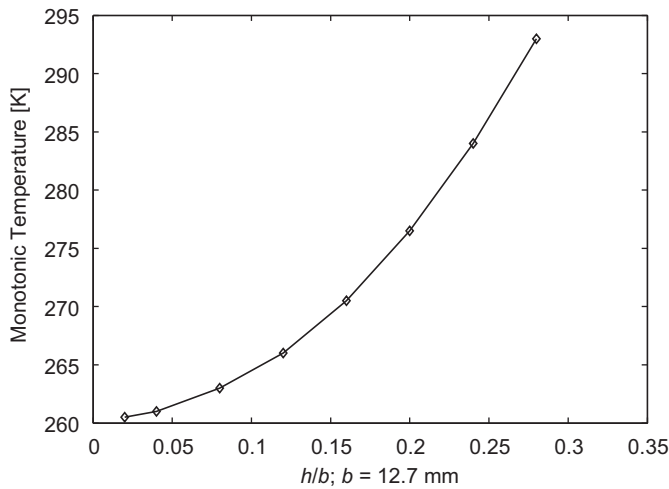


Fig. 12. Monotonic temperature for varying h/b with $b = 12.7$ mm for all beams.

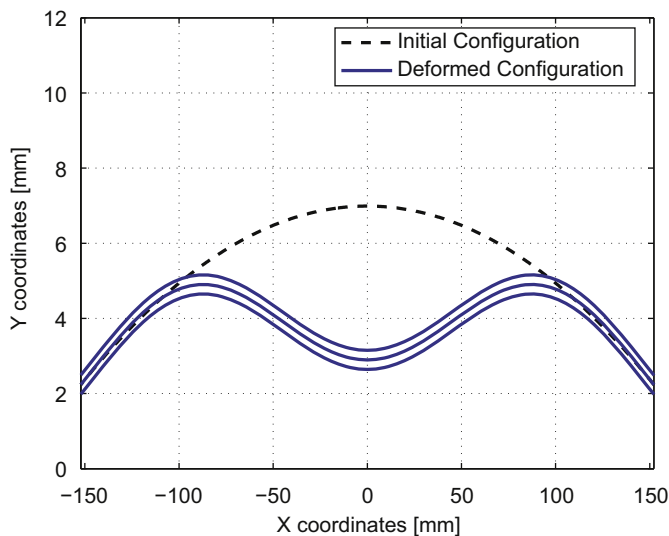


Fig. 13. Beam 5 ($R = 2438.4$ mm). Symmetric unstable solution; $\Delta T = 0$ K.

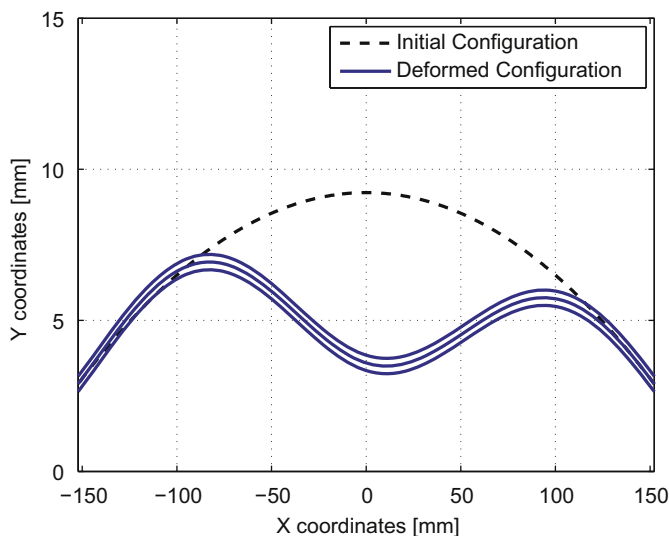


Fig. 14. Beam 3 ($R = 1828.8$ mm). Unstable asymmetric configuration; $\Delta T = 0$ K.

3.1. The monotonic temperature and the energy derivative tests

The coincidence of the limit point of the load–deflection curve at the monotonic temperature with the center point of the graph suggests that there is something special about this point, and inspection of the graphs suggests that this point is likely the inflection point of the curve (Figs. 15 and 16). Numerical evaluation of the derivative $\partial^2 P / \partial d^2$ confirms this. Note that these results are obtained through numerical approximation, therefore the coincidence points are not exact. However, we prove through analytical studies that this hypothesis holds for a simple case [26]. In the case of the symmetric point-loaded beam, we can construct a straightforward physical explanation of the existence of this center point that will help guide our understanding of more general load cases and geometries.

If the beam stays symmetric about the midpoint, the slope of the beam at the midpoint must always be horizontal, and by equilibrium the axial internal force at the midpoint must be equal to the horizontal reaction force at the supports. We intuitively expect that the unstable configuration with the maximum horizontal reaction force is the *maximally unstable configuration*, that is, the unstable configuration that would move to a stable configuration with the *maximum possible kinetic energy* relative to

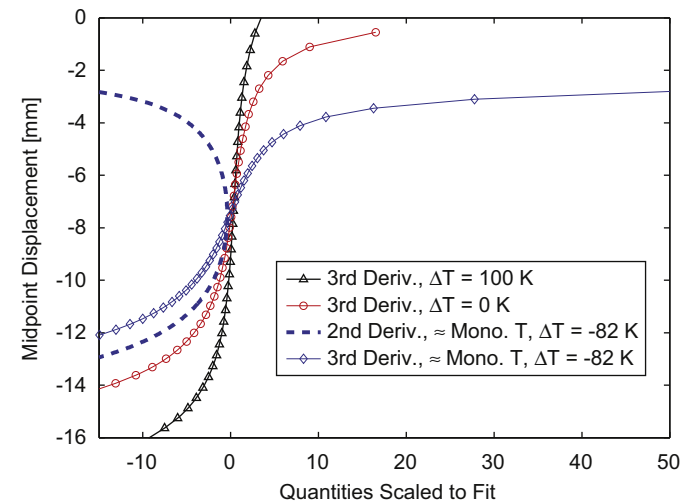


Fig. 15. Beam 2 ($R = 1270$ mm). Energy derivatives are zero at center point.

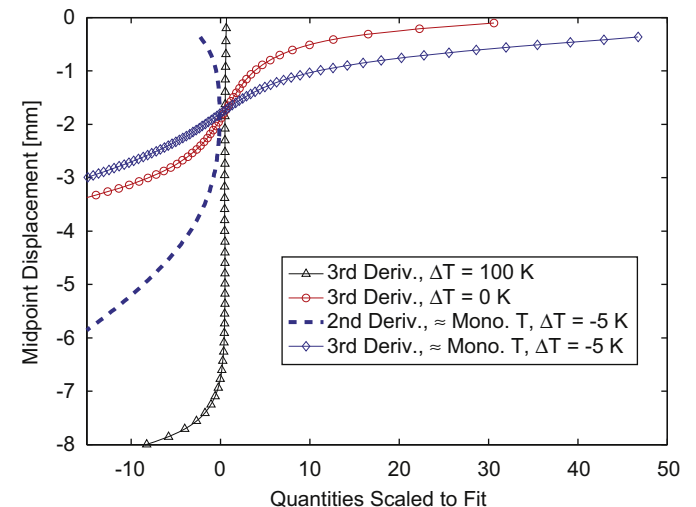


Fig. 16. Beam 8 ($R = 5080$ mm). Observation holds at varied curvatures.

all other unstable configurations (if the beam were initially held perfectly fixed at this configuration and then released).

The maximum horizontal reaction *does* coincide with the center point of the graphs (Fig. 17), indicating that the center point corresponds to the maximally unstable configuration. This does *not* mean that the horizontal reaction must be less than or equal to zero at the monotonic temperature in order to avoid instability, as one might assume: Fig. 17b shows that the maximum horizontal reaction can still be compressive at the monotonic temperature.

The center point is a function of the specific boundary value problem that we chose to explore. We would like to develop a more general test to determine the maximally unstable configuration for problems where the load–deflection curve may not be so well-behaved. The following heuristic argument will point us toward such a test. For this particular problem, the external work can be computed as the integral of the product of the concentrated load $P(d)$ and the deflection at the midpoint d .

The second derivative of energy gives the standard static stability test, while the third derivative of energy gives new information that should locate the center point. The third derivative of energy allows us to suggest a mathematical definition of the maximally unstable configuration and the monotonic temperature. Since the value of $\partial^2 E / \partial d^2$ can be considered a measure of the *degree of instability* present in the system, we would expect that a point where its derivative $\partial^3 E / \partial d^3$ is zero would be an *instability extremum* that is local to the unstable region. The maximally unstable configuration would be the instability extremum in the range where $\partial^2 E / \partial d^2 < 0$. If we are able to shrink this range by lowering the temperature, then in the limit where the unstable domain shrinks to zero we have both $\partial^3 E / \partial d^3 = 0$ and $\partial^2 E / \partial d^2 = 0$ at the *same* configuration. The temperature that generates this configuration and satisfies these conditions is the monotonic temperature. In other words, the temperature that shrinks the unstable region to a point, for which the maximally unstable ($\partial^3 E / \partial d^3 = 0$) and the minimally stable ($\partial^2 E / \partial d^2 = 0$) configurations are necessarily one and the same, is the monotonic temperature. Note that this is similar to the use of higher derivatives in continuation methods [22], though some simplifications of these more general (and computationally expensive) techniques may be possible for thermomechanical problems, as discussed below.

The energy E^{int} is obtained from the finite element code, and its numerical derivatives can be approximated by simple difference formulas. We use this data to test the above hypothesis and

we do find that the third numerical derivatives of energy are zero at the center point, and the second derivative of energy is zero at the same point for the monotonic temperature (Fig. 15). This observation holds for beams of significantly different curvatures (Fig. 16).

For the case of the distributed load (Fig. 2b), a global center point no longer exists (Fig. 18). The curves for lower temperatures possess a center point but the curves at elevated temperatures do not pass through it. Similar to the case of the concentrated load, the curved beam acts like an arch under distributed load, resisting primarily through axial stiffness rather than through weaker flexural stiffness. However, this “arch” is not geometrically perfect and suffers from local flexural buckling (Fig. 20a–c) at load values *below* those achieved in the case of the concentrated load.

These higher buckling modes may deflect upward at the midpoint even as global stability is lost, so we can no longer assume that $\partial P / \partial d = 0$ indicates a snap-through point, at least at elevated temperatures. Similarly, $\partial^3 E / \partial d^3 = 0$ does not occur in the distributed load case at high temperatures and can therefore no longer be related to the maximally unstable configuration as it can in the concentrated load case. Nonetheless, the energy derivatives are still zero at the monotonic temperature (Fig. 19).

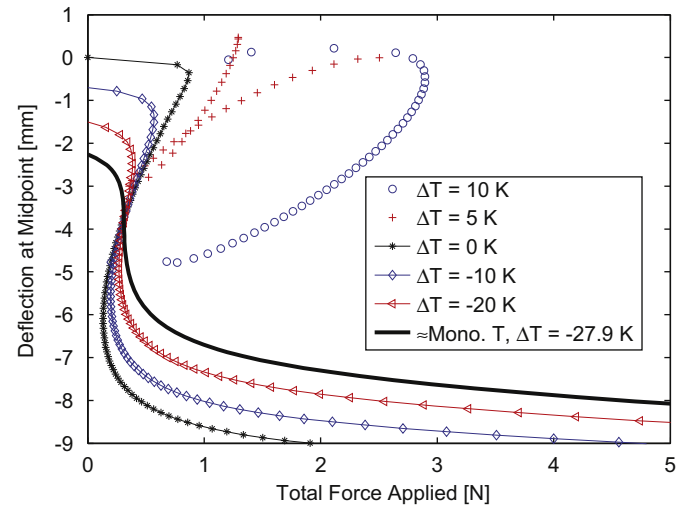


Fig. 18. Beam 5 ($R=2438.4$ mm). Load–deflection curves for distributed loads: no center point at elevated temperatures.

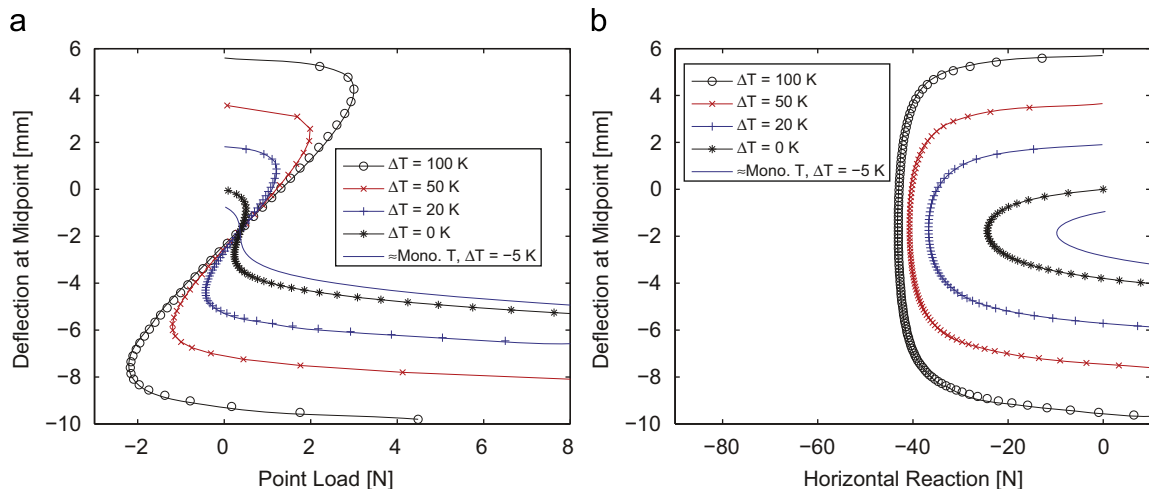


Fig. 17. Beam 8 ($R=5080$ mm). Maximum horizontal reaction occurs at center point: (a) load–deflection diagram and (b) beam horizontal reaction.

The distributed load case reinforces the earlier observation that the value of the monotonic temperature depends on the pattern of applied load: for the $R=2438.4$ mm beam, the symmetric point load leads to a monotonic temperature of $\Delta T = -22$ K, while for the distributed load case the monotonic temperature is approximately $\Delta T = -28$ K. The decreased monotonic temperature for the distributed load case indicates that it is possible to find a loading such that a “worst-case” monotonic temperature is obtained and a lower bound on the thermoelastic instability for all possible loadings of a system is established. This requires the solution of an inverse problem to determine the worst-case loading, which entails more complexity than is typically worth the effort,

especially if the actual load patterns a structure is subject to can be known in advance with reasonable certainty. This concept is not developed further in this paper, and all monotonic temperatures reported are limited to the specific load cases considered.

In all these examples, due to symmetry, the derivatives with respect to d (the midpoint deflection) provide clear information about the stability of the system. In general, there will not be a simple line of symmetry that will allow us to obtain meaningful information, as is apparent from the higher buckling mode load-deflection curves in Fig. 20. It would be preferable to develop an analytical test for the third derivative of energy that will let us circumvent the process of taking numerical derivatives entirely and allow us to determine the monotonic temperature for any given system.

Before assuming that the monotonic temperature obtained from static simulations is truly effective in eliminating snap-induced vibrations, we must first demonstrate that it eliminates snap-through in dynamic systems. The next section is devoted to establishing the validity of generalizing from the static, mechanical-only solution to the dynamic, thermomechanically coupled case. Then, we outline a test for establishing the monotonic temperature for arbitrary loading and member geometries in the final section.

4. Dynamic simulation of snap-through

In order to determine if the monotonic temperature estimated via static simulations successfully eliminates snap-through, dynamic simulations are conducted. We present here the results obtained for one beam only ($R=1828.8$ mm), with the same reference temperature $\Theta_{ref} = 300$ K used in the static simulations. Consequently, the beam number is no longer mentioned in the figure captions. This particular beam has a large initial curvature

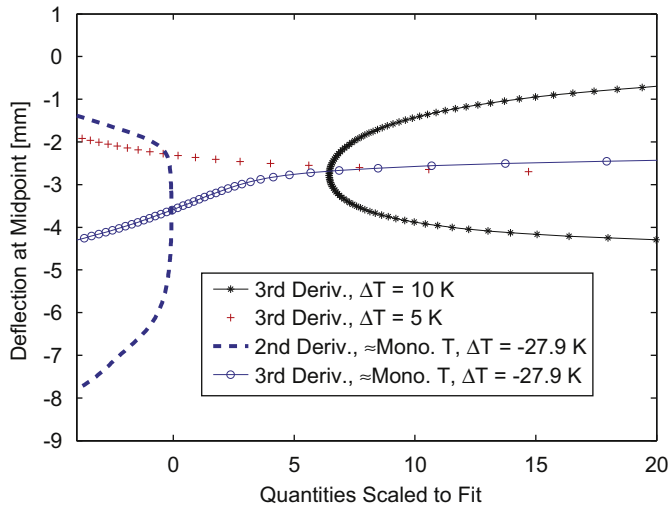


Fig. 19. Beam 5 ($R=2438.4$ mm). Energy derivatives are still zero at monotonic temperature despite the absence of a global center point.

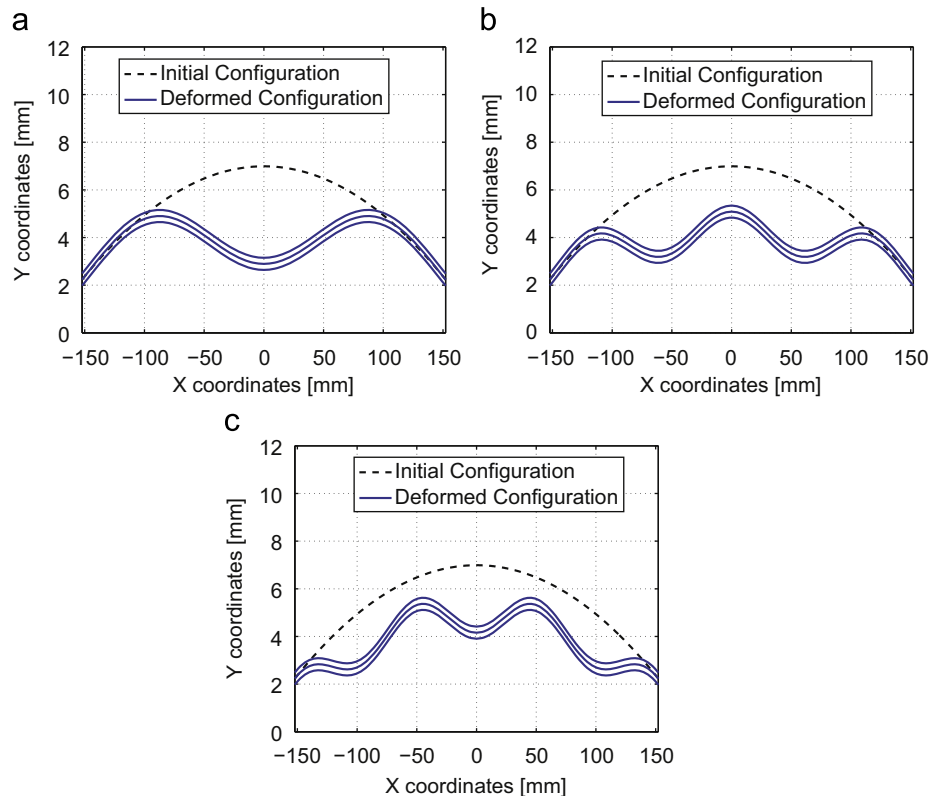


Fig. 20. Beam 5 ($R=2438.4$ mm) with distributed load: (a) $\Delta T = 0$ K, (b) $\Delta T = 5$ K and (c) $\Delta T = 10$ K.

but still possesses an estimated monotonic temperature that could be easily obtained in the laboratory ($\Delta T = -38$ K relative or $\Theta = -11$ °C/12 °F absolute). A concentrated force is applied at an effectively quasi-static rate at midspan and then held constant at a fixed target value greater than the static snap-through load P_s . The target load is $P = 2.0$ N for temperatures below $T = 30$ K, but the increase in snap-through load at increased temperature necessitated higher target loads of $P = 2.5$ and 3.0 N for $T = 50$ and 100 K respectively (Fig. 21).

Initial static simulations were conducted to obtain the thermally deformed initial configuration of the beam at each target temperature prior to dynamic simulation (Fig. 22). The initial temperature was applied as a perfectly uniform nodal initial condition and the surfaces of the beam were treated as perfectly insulated. Though this zero-heat-flux boundary condition is not feasible in an experimental setting, it allows us to isolate the temperature change due to thermomechanical coupling in our simulations. Purely mechanical dynamic simulations [20] had earlier indicated that a problem-specific critical time step of $\Delta t = 10^{-4}$ s or smaller must be used for accurate modeling of

snap-through. Values of Δt above this critical value could lead to spurious solutions that are clearly non-physical but nonetheless numerically converged.

The monotonic temperature estimated from static simulations successfully eliminated snap-through from dynamic simulations at quasi-static load rates. The maximum amplitude of displacement *does* clearly approach zero as the temperature approaches the monotonic temperature, and effectively reaches zero for $\Delta T = -50$ K (Fig. 23). The maximum displacement approaches a limit as the temperature increases; however, the maximum kinetic energy over all time values continues to increase linearly as the temperature increases (Fig. 24). This “excess” kinetic energy is present in *asymmetric* deformation modes not apparent from examination of the midpoint displacement alone.

Note that the ramp load continues to increase prior to reaching a constant value after snap-through, hence, the centerline of the vibrations moves downward on the plot prior to $t = 2.0$ s (Fig. 26).

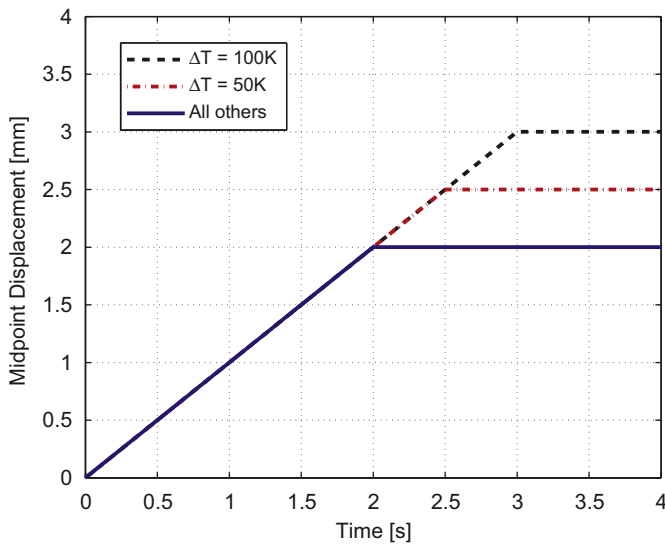


Fig. 21. Ramp load target values.

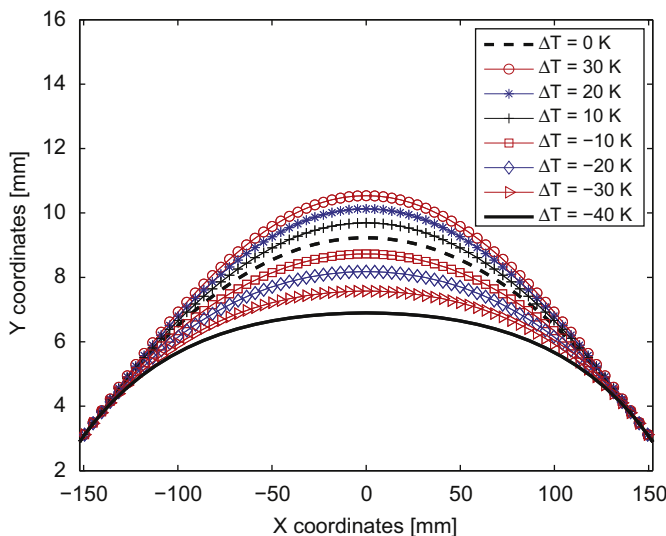


Fig. 22. Beam shapes at varied initial temperatures.

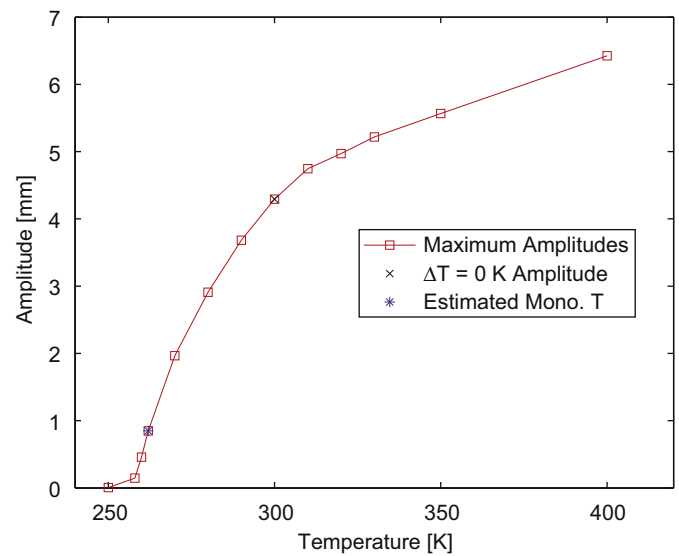


Fig. 23. Maximum amplitude of vibrations at various temperatures. Vibrations disappear near monotonic temperature and level off at elevated temperature.

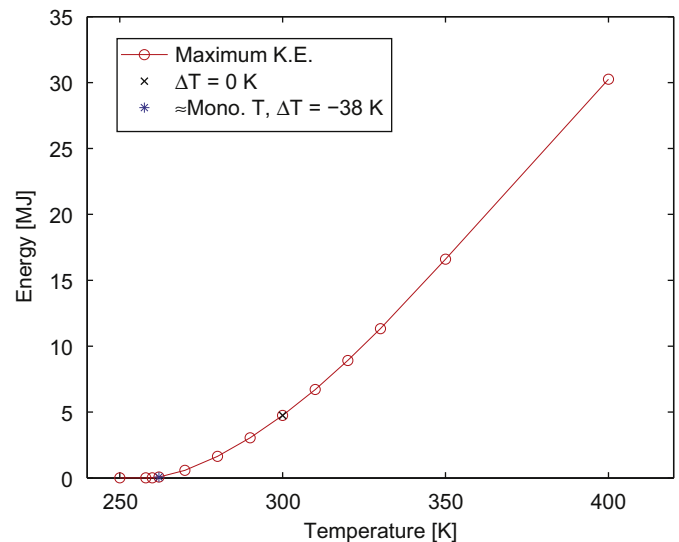


Fig. 24. Maximum kinetic energy at various temperatures. Kinetic energy disappears near monotonic temperature and increases linearly at elevated temperatures.

This component of the vibration must be filtered out in order to determine the amplitudes of vibration correctly. This was done by fitting a sixth-order polynomial to the post-snap midpoint displacement time history data and finding the value of the maximum difference between the smooth curve and the displacement.

The y-direction displacement at the midpoint is represented in Figs. 25–27 as a function of time for various initial temperatures and the static simulation results are superposed at the same scale. Thermoelastic damping is clearly apparent in these plots; by comparison, purely mechanical simulations of snap-through using the trapezoidal Newmark method showed *no* damping of the post-snap vibrations, as is expected for this energy-conserving time integration algorithm. Visual inspection of the graphs also indicates that the large-amplitude vibrations characteristic of snap-through are strongly attenuated below the monotonic temperature of $\Delta T = -38$ K (Fig. 26), dropping to nearly zero at $\Delta T = -50$ K (Fig. 27).

A measure of the asymmetry of vibration can be constructed by plotting the difference between the y-direction displacement

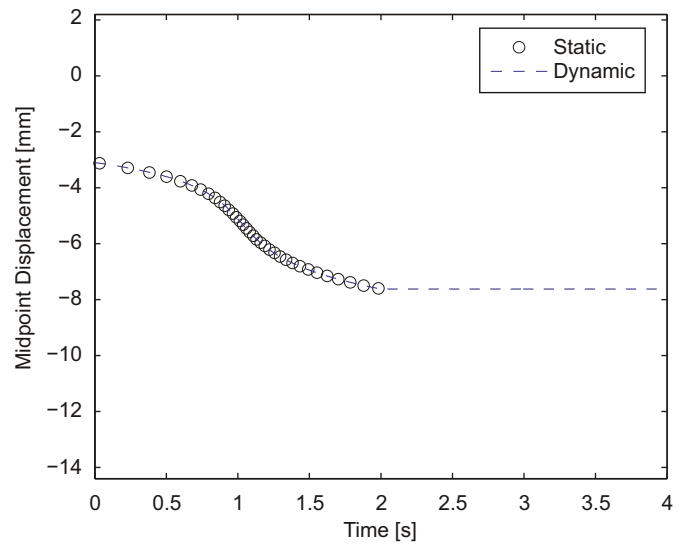


Fig. 27. Displacement at $\Delta T = -50$ K.

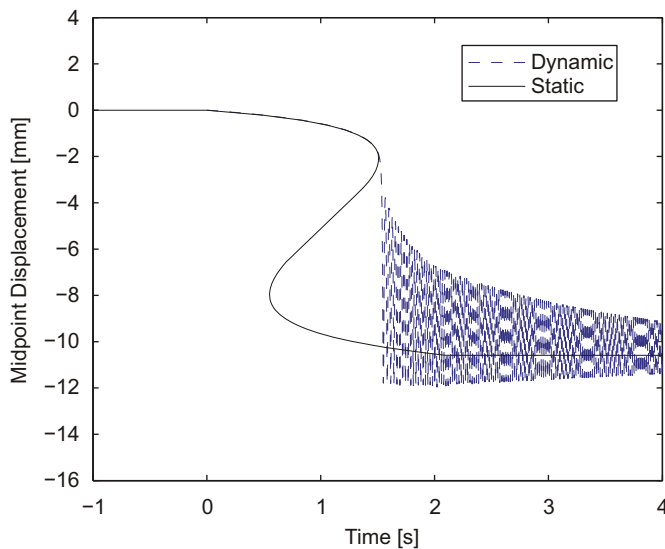


Fig. 25. Displacement at $\Delta T = 0$ K.

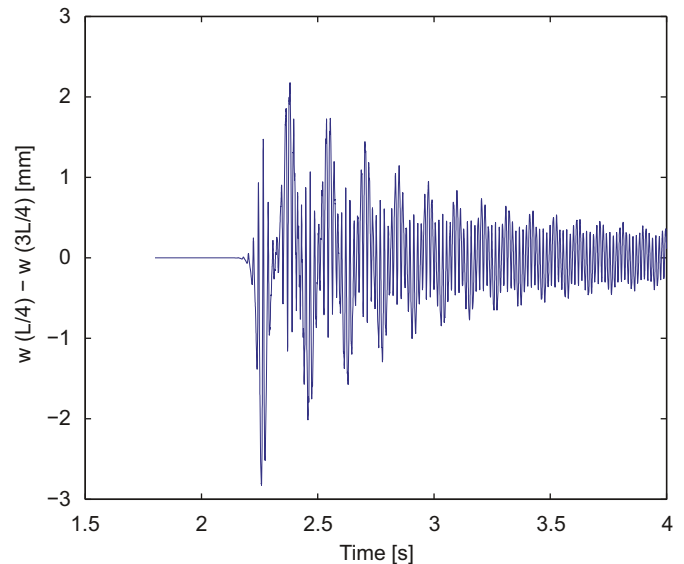


Fig. 28. Low-frequency asymmetric vibration damps out for $\Delta T = 30$ K.

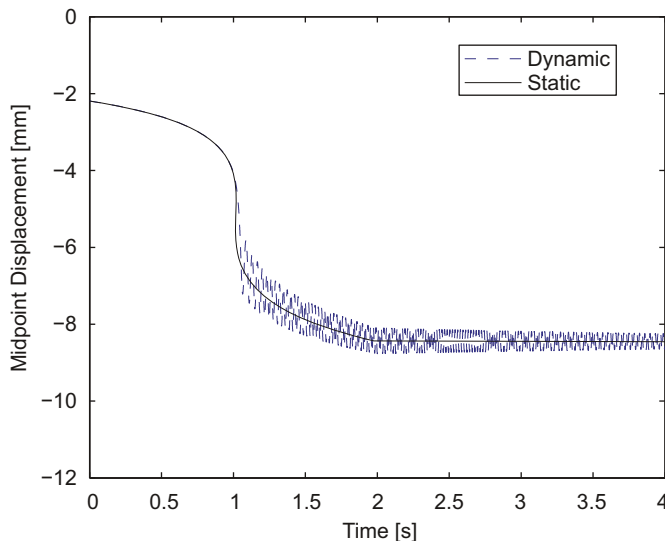


Fig. 26. Displacement at $\Delta T = -38$ K.

$w(x)$ at the points $x = L/4$ and $x = 3L/4$. This difference will be zero if the vibration is symmetric, or otherwise can give an estimate of the frequency and magnitude of the asymmetric vibration. For $\Delta T = 0$ K and below, the post-snap vibration remains perfectly symmetric for the beam considered. For $\Delta T = 30$ K, the post-snap vibration is initially symmetric, but after the load reaches a constant value the response develops an antisymmetric vibration (Fig. 28). This vibration damps out relatively quickly at $\Delta T = 30$ K, but at $\Delta T = 50$ K a similar mode of vibration is present at a higher amplitude and for a longer duration (Fig. 29). For $\Delta T = 100$ K, the beam buckles asymmetrically immediately prior to the static snap-through load and remains in a fully asymmetric mode after snap-through (Fig. 30).

Qualitatively, the $\Delta T = 30$ K and $\Delta T = 50$ K cases combine a symmetric mode (Fig. 31a) and an extremely low frequency asymmetric mode (Fig. 31b). The $\Delta T = 100$ K case buckles asymmetrically prior to snap-through (Fig. 32a) and remains in a high-frequency asymmetric mode that oscillates at an angle to the vertical following buckling (Fig. 32b). As this asymmetric mode is

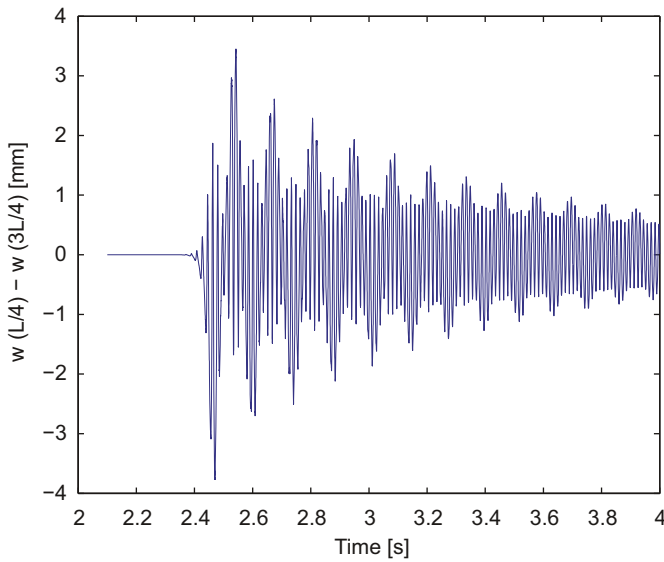


Fig. 29. Low-frequency asymmetric vibration sustains longer for $\Delta T = 50$ K.

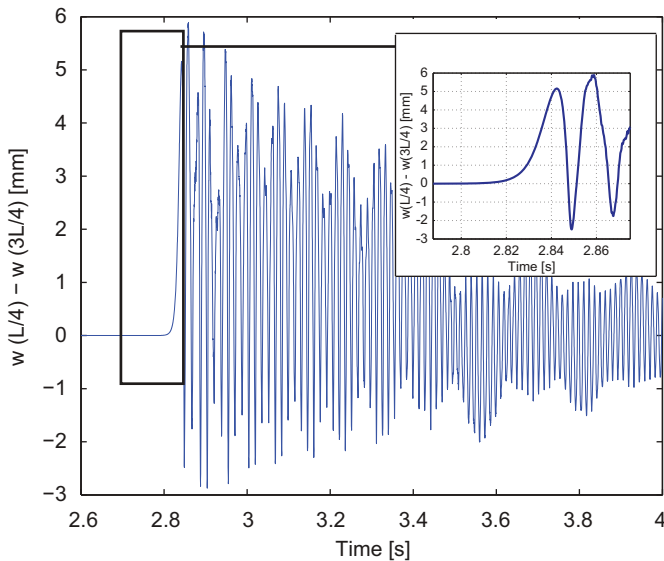


Fig. 30. Beam buckles asymmetrically prior to snap-through at $\Delta T = 100$ K.

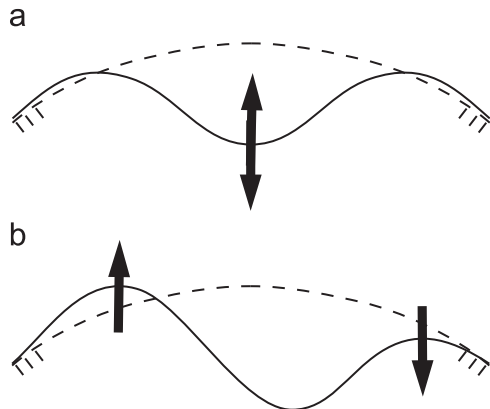


Fig. 31. Mode shapes for $\Delta T = 30$ and 50 K: (a) symmetric and (b) asymmetric.

damped, a new mode emerges (following $t=3.4$ s) similar to the low-frequency asymmetric mode encountered at $\Delta T = 30$ K and $\Delta T = 50$ K.

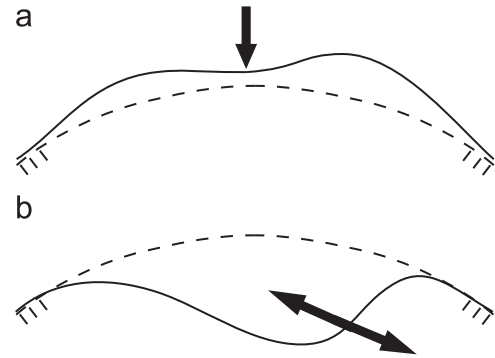


Fig. 32. $\Delta T = 100$ K: (a) initial asymmetric buckling and (b) asymmetric "side-ways" post-buckling mode.

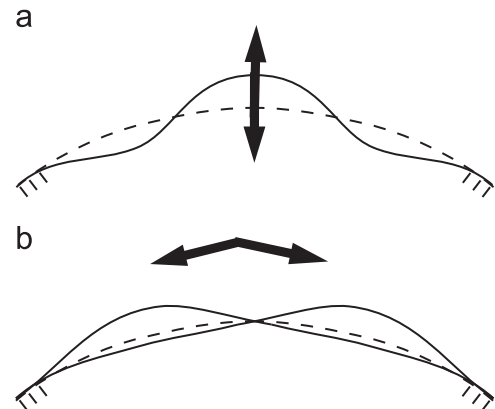


Fig. 33. Modes at unloading for $\Delta T = 0$ K: (a) symmetric and (b) traveling wave.

Unloading the beam from an initially stationary deformed configuration reveals that the vibration about the initial undeformed configuration is of significantly lower amplitude than the vibration about the deformed configuration. Although the initial post-snap unloading response begins as a symmetric vibration, it develops a small asymmetry that quickly grows in magnitude. While the initial transient mode shape is essentially similar to the low-order symmetric mode of the loading response (Fig. 33a), inspection of the deformed configurations reveals that the asymmetric mode behaves like a low-frequency "wave" reflecting back and forth between the supports (Fig. 33b). Fig. 34 shows the loading and unloading responses.

These various modes interact non-linearly in the finite-deformation model, and the resulting transient behavior can become difficult to quantify, especially as higher modes are activated and the post-snap motion increases in complexity. However, the higher modes diminish with decreasing temperature and eventually disappear at the monotonic temperature, making the monotonic temperature a solid point of reference in an otherwise convoluted post-buckling regime.

The monotonic temperature also holds for the distributed load case. The $R=2438.4$ mm beam displays the same sort of asymmetric buckling prior to the static snap-through load at $\Delta T = 0$ K under distributed loading that is seen at $\Delta T = 100$ K for the $R=1828.8$ mm beam under concentrated loading. At the estimated monotonic temperature nonetheless, post-snap vibrations are attenuated as effectively in the distributed load case as they are in the concentrated load case (Fig. 35).

There are some caveats on the generality of the monotonic temperature. The softening response seen in the static solution paths even for temperatures below the monotonic temperature

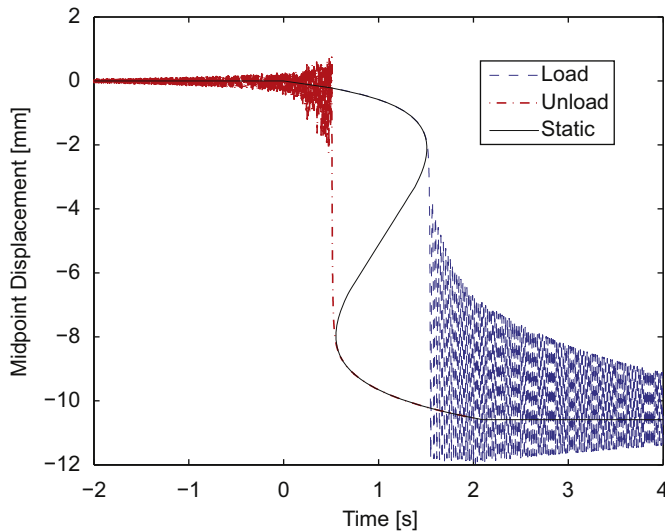


Fig. 34. Beam 3 ($R=1828.8$ mm). Asymmetry of loading and unloading response at $\Delta T = 0$ K.

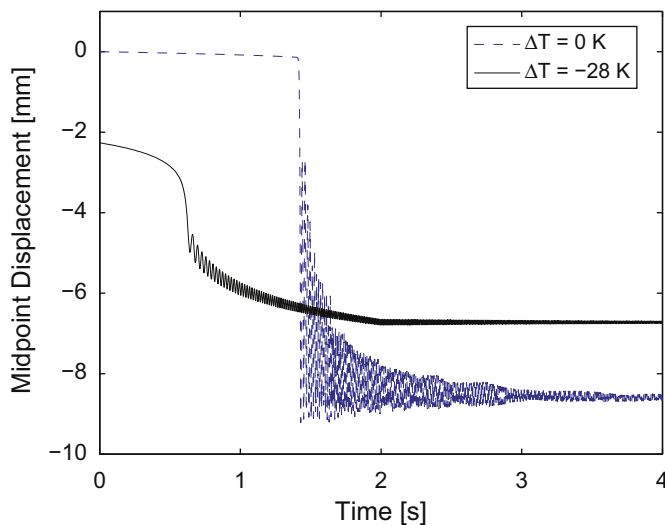


Fig. 35. Beam 5 ($R=2438.4$ mm). Static monotonic temperature estimate holds for distributed load case.

can still lead to snap-like behavior if the loading rate is high enough to force the system to dynamically jump off the static solution curve as the system softens with increasing load. More generally, the system must be dissipative for the temperature to remain below the monotonic temperature. This is true in our case, but it is no longer valid if body heat sources or applied surface heat fluxes are present. We are therefore limited to saying that the monotonic temperature provides a lower bound below which snap-through will *never* occur at any applied load level *if* the loading rate is effectively quasi-static *and* the system is dissipative.

The monotonic temperature estimated from static simulations is not perfectly precise; it does not completely eliminate the oscillations even for dynamic systems with effectively quasi-static loading. Some of these errors are due to the simple approach that was undertaken to find this temperature, where the monotonicity of the curve was determined only approximately. Another source for the discrepancy is due to the physical fact that the ramp loading can never be truly quasi-static in a dynamic simulation. The amplitude of vibration will go to zero *nearer* the monotonic temperature (refer to Fig. 23) if the loading

rate is decreased, but there will always exist *some* small dynamic jump as the system approaches the limit point on the static load-deflection curves.

One additional practical observation can be made. We have modeled the curved beam with an edge that is free to move in the z -direction (out-of-plane) between the fixed supports. In many practical engineering applications, such as stressed-skin monocoque aircraft construction, the z -direction will be restrained as well, and we expect this additional boundary condition to have a stabilizing effect. These additional boundary conditions increase the snap-through load (Fig. 36) as well as the monotonic temperature itself (Fig. 37). The monotonic temperatures obtained from the static simulations without these boundary conditions are therefore conservative values relative to systems that include such constraints.

Note that, in the static simulations, we have omitted heat conduction and treated temperature as a purely mechanical expansion or contraction of the material, which provided a valid estimate of the snap-free monotonic temperature for the dynamic thermomechanically coupled case. This analogy between mechanical strain and thermal strain indicates that an applied

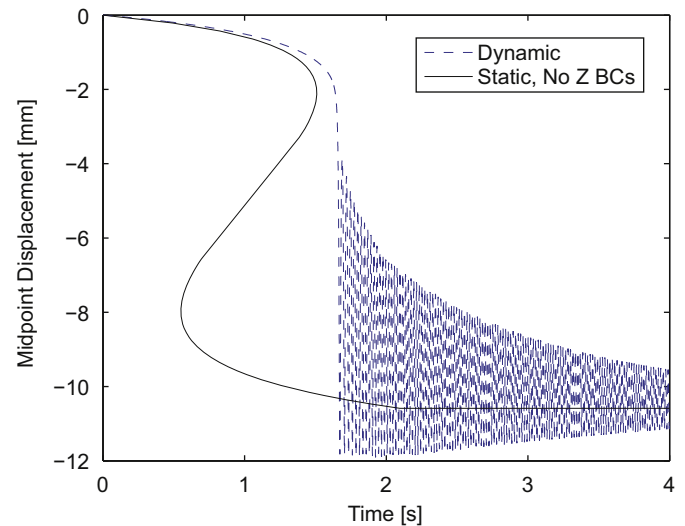


Fig. 36. Beam 3 ($R=1828.8$ mm). Full z -direction edge boundary condition increases snap-through load.

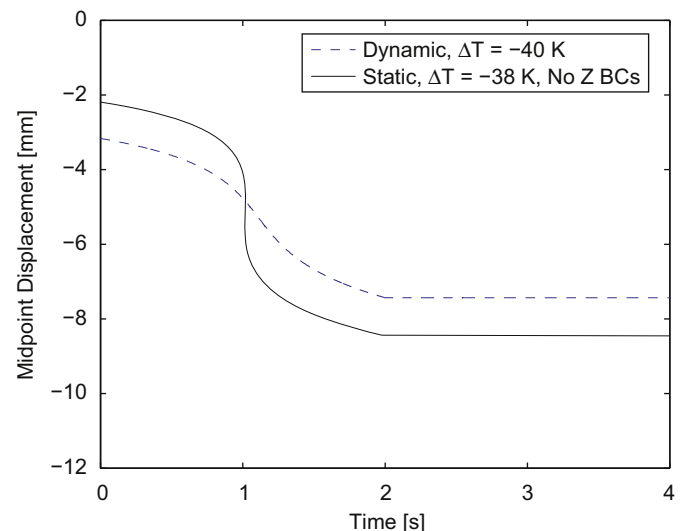


Fig. 37. Beam 3 ($R=1828.8$ mm). Full z -direction edge boundary condition increases monotonic temperature.

mechanical *prestress* will have a mechanical effect similar to lowering the temperature. For example, for the unloaded $R=1270$ mm beam, the reaction at the supports has no vertical component and has a horizontal component of $P_x = 9.42$ N at the monotonic temperature $\Delta T = -82$ K; the horizontal reaction is $P_x = 15.4$ N for $\Delta T = -100$ K. Given the out-of-plane depth of $d=28.7$ mm and beam thickness $t=1.27$ mm, and assuming a uniform stress over the cross-section, the axial stress in the beam is therefore 0.4225 MPa for $\Delta T = -100$ K, which is only a minute fraction of the yield stress of $\sigma_y = 250$ MPa for A36 structural steel. Although $\Delta T = -100$ K is clearly an unrealistic temperature, $\sigma = 0.4225$ MPa is a perfectly realistic prestress. Consequently, an applied mechanical *prestress* will have a mechanical effect similar to lowering the temperature, and therefore we could eliminate quasi-static snap-through by applying a purely mechanical pre-tension sufficient to achieve a tensile strain identical to or greater than that produced by the monotonic temperature. Moreover, it is also possible to apply *additional* initial strain sufficient to *cancel* the effects of thermal expansion, so that a heated beam can be “snap-proofed” for temperatures below a given elevated target temperature.

In practical aerospace applications, significant prestress is introduced to thin structural members to provide increased structural stiffness, independent of any thermal considerations. This prestress is sufficient to introduce tensile strains equivalent or greater than those introduced by the monotonic temperature, as is apparent from the above example. It is therefore unlikely that typical aerospace structures will experience snap-through under standard operating conditions. However, as the operating conditions of the structure become more severe, as in hypersonic flight, much larger thermal loads can be expected. Additional mechanical pre-tension could therefore prove useful in providing additional protection against snap-through in aerospace structures in extreme operating environments, although more research would be required to determine the effectiveness, applicability, and limitations of this approach.

5. Maximum instability and bounds on snap-through

In the previous sections, we have established that (1) the monotonic temperature represents a lower bound on static instability in curved beams subject to snap-through, and (2) for the simple symmetric beam with a concentrated load, the second and third derivatives of energy with respect to the midpoint displacement are both zero at the snap-through point at this temperature. We surmised that the unstable region shrinks as the temperature is lowered until it becomes a point at the monotonic temperature, and that at this point the minimally stable configuration ($\partial^2 E / \partial d^2 = 0$) and maximally unstable configuration ($\partial^3 E / \partial d^3 = 0$) are identical. This shrinkage of the unstable region to a point as temperature is lowered is illustrated conceptually in Fig. 38. We also observed that, although multiple modes may exist corresponding in some cases to multiple paths within the unstable region (Fig. 39), in static simulations these modes tend to disappear as the monotonic temperature is approached.

These observations suggest a mathematical definition of the monotonic temperature. We do not attempt to prove the following conjectures, but the simulation results support them. If we are able to shrink the unstable region along the equilibrium path of our system by altering some parameters (such as temperature), then the configuration where the critical parameters are such that snap-through no longer occurs is exactly the point where the minimally stable configurations at the boundaries of the unstable region coincide with the maximally unstable configuration. Such conditions should therefore give us a set of equations that provide

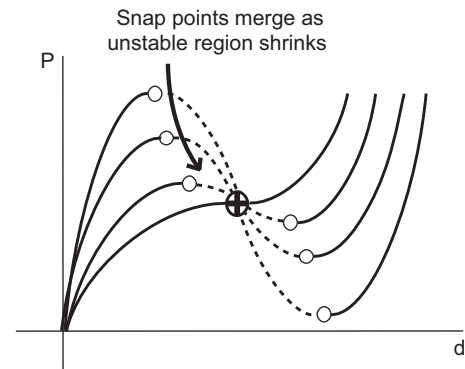


Fig. 38. Conceptual illustration of lower bound.

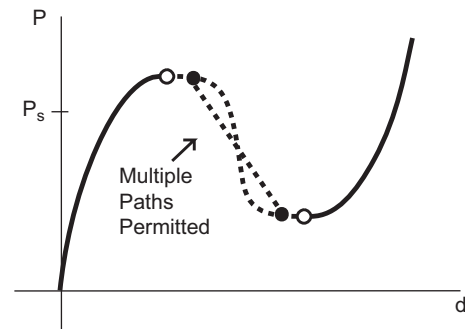


Fig. 39. Multiple paths within the unstable region.

a bound of the domain of unstable behavior. Without attempting to prove them, we state here these conditions.

Conjecture. Let d be the displacement field in a continuum, and let \mathbf{p} be a vector of bifurcation parameters, which control the size of the unstable region. Assume that the system under consideration has only one unstable region. Let G , A , B be the first, second and third derivatives of the energy. The unstable region ceases to exist for the particular configuration (d^*, \mathbf{p}^*) at which, for all virtual displacement fields δd , the functionals G , A and B are null: $G(d^*, \mathbf{p}^*, \delta d) = 0$, $A(d^*, \mathbf{p}^*, \delta d) = 0$, and $B(d^*, \mathbf{p}^*, \delta d) = 0$.

If we use a finite element approximation of the functionals from a continuum problem, we obtain the version of the above conditions in matrix form: $\mathbf{G}(d^*, \mathbf{p}^*) = 0$, $\det \mathbf{A}(d^*, \mathbf{p}^*) = 0$, and $\det \mathbf{B}(d^*, \mathbf{p}^*) = 0$. In this discretized form, \mathbf{G} is a vector (the residual vector in finite element methods), \mathbf{A} is a second-order tensor (the stiffness matrix), \mathbf{B} is a third-order tensor, and d^* is a vector (of nodal displacements).

A simple non-linear Timoshenko beam model demonstrates the utility of these conjectures and also demonstrates why limited-deflection models, such as the von Karmann equations, are a priori incapable of determining the monotonic temperature. The interested reader is referred to [26] for the detailed derivation corresponding to the beam model. Unlike the fully non-linear equilibrium equations, the third variational derivative of the linearized beam equations is identically zero. In taking the Taylor series approximation of the fully non-linear Timoshenko beam equilibrium equations we have *lost information*, and, as discussed in [26], the information we have lost from the third derivative of energy is exactly the information we require to be able to pinpoint the non-trivial snap-free configuration that exists at the monotonic temperature. The von Karmann equations therefore do not disclose the existence of the non-trivial solution precisely because the information that is needed to determine it has been omitted a priori.

6. Conclusions

We demonstrated the existence of a non-trivial curved beam configuration and a corresponding critical temperature, lowered with respect to the reference temperature, that eliminates the occurrence of dynamic snap-through under quasi-static loading rates. This *monotonic temperature* can be estimated from static solution paths with reasonable accuracy, even for beams of large initial curvature. An analytical test based on the third variational derivative of the energy that could be useful in determining the monotonic temperature for members of general geometry and load patterns is also suggested. The failure of limited-deformation thermal beam and plate models such as the von Karmann equations to disclose the existence of a non-trivial snap-free solution is shown to be a consequence of the omission of information about the third variational derivative of energy from these lower-order theories.

The analogy between purely mechanical contraction and thermal strain that holds for these numerical experiments suggests that an applied mechanical prestress that introduces an initial strain equivalent to the strain induced by the monotonic temperature eliminates the possibility of quasi-static snap-through in beams of large initial curvature. Increasing the initial prestress in thin-walled structures using values determined from this procedure could therefore provide a simple method of protecting against large amplitude snap-through vibrations encountered in by aircraft and spacecraft in extreme operating environments. Although this method would introduce additional stresses into the supporting members and therefore has limitations depending on the requirements of the structure, it is simpler than other methods that have been proposed in the literature [30]. Further research would be needed to determine the potential effectiveness and practical limitations of this proposed method of alleviating dynamic snap-through.

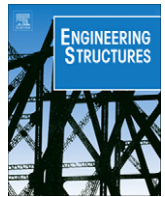
Acknowledgments

The authors would like to thank Professor Lawrence Virgin (Duke University) for his valuable comments and suggestions.

The work has been funded in part by AFOSR under the Grant no. FA9550-09-1-0201. This support is greatly appreciated.

References

- [1] K. Murphy, L. Virgin, S. Rizzi, Characterizing the dynamic response of a thermally loaded, acoustically excited plate, *Journal of Sound and Vibration* 196 (1996) 635–658.
- [2] W.Y. Tseng, J. Dugundji, Nonlinear vibrations of a beam under harmonic excitation, *Journal of Applied Mechanics, Transactions of the ASME Series E* 37 (2) (1970) 292–297.
- [3] W. Kreider, A. Nayfeh, Experimental investigation of single-mode responses in a fixed-fixed buckled beam, *Nonlinear Dynamics* 15 (2) (1998) 155–177.
- [4] K. Murphy, L. Virgin, S. Rizzi, Experimental snap-through boundaries for acoustically excited, thermally buckled plates, *Experimental Mechanics* 36 (4) (1996) 312–317.
- [5] H. Irschik, Large thermoelastic deflections and stability of simply supported polygonal panels, *Acta Mechanica* 59 (1) (1986) 31–46.
- [6] P. Ribeiro, E. Manoach, The effect of temperature on the large amplitude vibrations of curved beams, *Journal of Sound and Vibration* 285 (4–5) (2005) 1093–1107.
- [7] Y.-L. Yeh, Chaotic and bifurcation dynamic behavior of a simply supported rectangular orthotropic plate with thermo-mechanical coupling, *Chaos, Solitons and Fractals* 24 (5) (2005) 1243–1255.
- [8] D. Liaw, Nonlinear supersonic flutter of laminated composite plates under thermal loads, *Computers and Structures* 65 (5) (1997) 733–740.
- [9] M. Ganapathi, T. Prakash, Supersonic flutter characteristics of functionally graded flat panels including thermal effects, *Composite Structures* 72 (1) (2006) 10–18. doi:10.1016/j.compstruct.2004.10.007.
- [10] J.-M. Dhainaut, X. Guo, C. Mei, S.M. Spottswood, H.F. Wolfe, Nonlinear random response of panels in an elevated thermal-acoustic environment, *Journal of Aircraft* 40 (4) (2003) 683–691.
- [11] Y.-L. Yeh, C.-K. Chen, H.-Y. Lai, Chaotic and bifurcation dynamics for a simply supported rectangular plate of thermo-mechanical coupling in large deflection, *Chaos, Solitons and Fractals* 13 (7) (2002) 1493–1506.
- [12] L. Librescu, W. Lin, M. Nemeth, J. Starnes Jr., Vibration of geometrically imperfect panels subjected to thermal and mechanical loads, *Journal of Spacecraft and Rockets* 33 (2) (1996) 285–291.
- [13] J.-S. Park, J.-H. Kim, S.-H. Moon, Thermal post-buckling and flutter characteristics of composite plates embedded with shape memory alloy fibers, *Composites Part B: Engineering* 36 (8) (2005) 627–636.
- [14] I. Lee, D.-M. Lee, I.-K. Oh, Supersonic flutter analysis of stiffened laminated plates subject to thermal load, *Journal of Sound and Vibration* 224 (1) (1999) 49–67.
- [15] M. Vaz, R. Solano, Postbuckling analysis of slender elastic rods subjected to uniform thermal loads, *Journal of Thermal Stresses* 26 (9) (2003) 847–860.
- [16] S. Li, X. Song, Large thermal deflections of Timoshenko beams under transversely non-uniform temperature rise, *Mechanics Research Communications* 33 (1) (2006) 84–92.
- [17] S. Li, Y. Zhou, Geometrically nonlinear analysis of Timoshenko beams under thermomechanical loadings, *Journal of Thermal Stresses* 26 (9) (2003) 861–872.
- [18] L. Virgin, *Vibration of Axially Loaded Structures*, Cambridge University Press, 2007.
- [19] R. Plaut, L. Virgin, Vibration and snap-through of bent elastica strips subjected to end rotations, *Journal of Applied Mechanics* 76 (4) (2009) 041011 (7 pp.). doi:10.1115/1.3086783.
- [20] Y. Chandra, I. Stanciulescu, T. Eason, M. Spottswood, Numerical pathologies in snap-through simulations, *Engineering Structures*, in press, doi:10.1016/j.engstruct.2011.10.013.
- [21] R.L. Taylor, *FEAP A Finite Element Analysis Program*, version 8.3, user manual ed., Department of Civil and Environmental Engineering, University of California at Berkeley, Berkeley, California, 2011.
- [22] H. Chen, L. Virgin, Finite element analysis of postbuckling dynamics in plates: Part I: an asymptotic approach, *International Journal of Solids and Structures* 43 (2006) 3983–4007.
- [23] Y.-L. Yeh, C.-K. Chen, H.-Y. Lai, Chaotic and bifurcation dynamics of a simply-supported thermo-elastic circular plate with variable thickness in large deflection, *Chaos, Solitons and Fractals* 15 (5) (2003) 811–829.
- [24] F. Armero, J. Simo, A new unconditionally stable fractional step method for non-linear coupled thermomechanical problems, *International Journal for Numerical Methods in Engineering* 35 (4) (1992) 737–766.
- [25] J. Simo, C. Miehe, Associative coupled thermoplasticity at finite strains: formulation, numerical analysis and implementation, *Computer Methods in Applied Mechanics and Engineering* 98 (1) (1992) 41–104. doi:10.1016/0045-7825(92)90170-O.
- [26] T. Mitchell, A Lower Bound on Snap-through Instability in Thermomechanically Coupled Curved Beams, Master Thesis, University of Illinois at Urbana-Champaign, 2009.
- [27] W. Poon, C. Ng, Y. Lee, Dynamic stability of a curved beam under sinusoidal loading, *Proceedings of the Institution of Mechanical Engineers. Part G: Journal of Aerospace Engineering* 216 (4) (2002) 209–217.
- [28] H. Chen, L. Virgin, Finite element analysis of postbuckling dynamics in plates: Part II: a nonstationary analysis, *International Journal of Solids and Structures* 43 (2006) 4008–4027.
- [29] B. Moghaddasie, I. Stanciulescu, M. Rezaiee-Pajand, The Effect of Imperfections on Critical Load in Elastic Structures, under review.
- [30] J.-S. Park, J.-H. Kim, Suppression of aero-thermal large deflections and snap-through behaviors of composite panels using macro fiber composite actuators, *Smart Materials and Structures* 13 (6) (2004) 1448–1459.



Numerical pathologies in snap-through simulations

Yenny Chandra^a, Ilinca Stanciulescu^{a,*}, Thomas Eason^b, Michael Spottswood^b

^a Rice University, Department of Civil and Environmental Engineering, 6100 Main Street, Houston, TX 77005, USA

^b Air Force Research Laboratory, Structural Sciences Center, 2790 D. Street, WPAFB, OH, USA

ARTICLE INFO

Article history:

Received 11 September 2010

Revised 7 October 2011

Accepted 7 October 2011

Keywords:

Snap-through

Finite element

Curved beam

Solid (continuum) elements

Structural elements

Time integrators

Numerical pathologies

ABSTRACT

Aircraft structures operating in severe environments may experience snap-through, causing the curvature on part or all of the structure to invert inducing fatigue damage. This paper examines the performance of beam and continuum nonlinear finite element formulations in conjunction with several popular implicit time stepping algorithms to assess the accuracy and stability of numerical simulations of snap-through events. Limitations of the structural elements are identified and we provide examples of interaction between spatial and temporal discretizations that affect the robustness of the overall scheme and impose strict limits on the size of the time step. These limitations need to be addressed in future works in order to develop accurate, robust and efficient simulation methods for response prediction of structures encountering extreme environments.

© 2011 Elsevier Ltd. All rights reserved.

1. Introduction

Curved beams or panels can often be found as components of complex structures in civil, mechanical, and aerospace applications. They may experience snap-through causing the curvature on part or all of the structure to invert due to a large inward loading (Fig. 1(a)) caused by extreme loading conditions [1]. When snap-through happens, the load–deflection diagram presents a jump, e.g., from point B to point C, as shown in Fig. 1(b). In some cases, when the load is reduced, *hysteresis* is observed: the structure will snap-back to its original configuration but on a different path (represented by the jump from point D to point A in the same figure).

Snap-through is characterized by large nonlinear deformations, changes in the system stability and large stress reversals, which accelerate fatigue damage. Since no analytical solutions for general systems with snap-through exist, numerical models that can capture these phenomena are needed in order to predict the fatigue life of the structure. Among the numerical techniques, the Finite Element Method (FEM) provides the most generality and can be applied to systems with arbitrarily complex geometries. This paper analyzes the performance of several finite element formulations (2D and 3D) and the stability of the time-stepping schemes in simulating a curved beam undergoing snap-through: we identify the important features that affect the numerical accuracy and robustness and the region where the schemes are stable for such simulations.

The snap-through of curved beams or shallow arches has been studied analytically for particular cases by numerous authors, including Murphy et al. [2], Virgin [3], Bradford et al. [4], and Plaut and Virgin [5]. Snap-through can also be studied qualitatively using a truss system [6]. Simplifying assumptions are usually needed in finding the analytical estimates. While we are paying the price of the lack of physical intuition by using the complex FEM, we often need to do so in order to use more general analysis techniques that allow for complex effects to be captured. Therefore, we test here the performance of this method when applied to a simple curved beam structure (geometry and properties introduced in Section 2). This structure is representative since it exhibits the type of phenomena we wish to study (snap-through) but simple enough to allow for comparisons with solutions obtained with analytical methods as well.

In this paper, the numerical simulations are performed with the Finite Element Analysis Program (FEAP), a research code that includes most commonly used finite elements and solvers and provides a reliable framework for developing and implementing new user formulations [7]. The factors taken into consideration in this study are (1) the time-stepping algorithm, (2) the element type, and (3) the size of the time step. The element formulations and the time-stepping algorithms discussed are either available from the standard FEAP distribution or implemented as user subroutines. The main criterion used to verify the robustness of the results is the energy conservation throughout the simulation.

For discretization, 2D straight beam elements and 3D solid linear and quadratic elements are used. All formulations account

* Corresponding author. Tel.: +1 713 348 4704; fax: +1 713 348 5268.

E-mail address: ilinc@rice.edu (I. Stanciulescu).

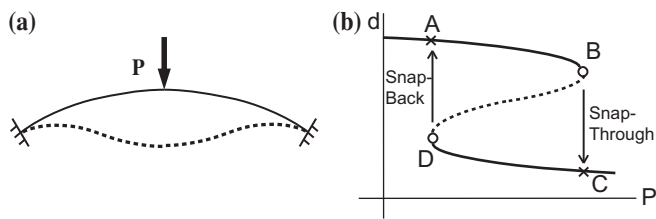


Fig. 1. Snap-through buckling of shallow structures: (a) initial and post-snap configuration, (b) load-deflection curve.

for large deformations. The 2D beam elements utilized are (1) beam elements without shear deformation with *large displacement* and small rotation (2nd order theory) with cubic interpolation, and (2) beam elements with shear deformation formulation and *large displacement* and *large rotation* that can consider inelastic behavior for bending and axial effects but retain linear elastic response in the transverse shear terms [7]. The 3D solid elements used are linear (8-nodes) elements with displacement, mixed (B-bar), and enhanced formulations and quadratic (27-nodes) elements with displacement formulation. Unlike the *structural* elements, e.g., beams, the continuum (3D solid) elements do not include a built in kinematic assumption. *This characteristic makes them suitable for consistent incorporation of other effects, such as thermomechanical coupling in future studies.* Note that in the current study, no coupling, and no material or boundary nonlinearities are included.

Conventional approaches in the stability analysis of structures often make use of static considerations, but in fact, even when the loads are applied statically, buckling and snap-through are inherently dynamic processes and a full description of the structural behavior can be obtained only through a dynamic analysis [3]. Numerical simulations of such phenomena require access to stable time-stepping schemes and in general to robust simulation environments.

Unfortunately, due to the kinematic assumptions incorporated in the structural elements, the use of these elements coupled with the time-stepping integrators is prone to numerical difficulties that affect the accuracy of the results as shown in Section 4. Numerical instabilities mask the true physical behavior rendering the structural response prediction inaccurate.

An important component of the simulation environment is the time-stepping scheme. We examine here the common choices for structural mechanics simulations: (1) the traditional Newmark integrator [8] and (2) energy-momentum conserving algorithms. The Newmark method is the most widely used time integrator in the area of structural analysis. For certain combinations of parameters, it is unconditionally stable for linear problems. However, its stability is not guaranteed for nonlinear problems. The traditional time-stepping algorithms developed for structural dynamics applications usually perform well for linear problems. In the nonlinear regime, however, numerical instabilities appear due to the energy increase of the discrete system. Hence, energy-momentum schemes were developed to overcome the lack of conservation [9]. These schemes belong to a class of algorithms designed to satisfy various conservation laws by construction. The energy-momentum algorithms used are (1) the algorithm based on the work by Simo and Tarnow [10], Simo et al. [11], and Gonzalez [12] and (2) a composite algorithm based on the trapezoidal rule and the three point backward Euler proposed by Bathe [13] that is stable for large time steps. These algorithms will be referred as conserving A and conserving B, respectively, in the rest of this paper. Many authors used conserving A to solve various types of problems [14]. In a recent work, Garikipati et al. [15] used this algorithm to model growth in biological tissue. Bathe [13] showed that the conserving B algorithm, which is incorporated in the

commercial FEM software ADINA 8.7, is able to solve a specific type of problem where the Newmark algorithm is unstable and does not conserve energy and momentum. Although the conserving B scheme allows us to use larger time steps, interactions between the time-stepping schemes and the spatial discretizations might still occur when structural elements are used.

This paper is organized as follows. Section 2 describes the representative structure used throughout the paper. Section 3 compares the results of the static analyses obtained using different element types and formulations. Section 4 analyzes the numerical results of the nonlinear dynamic simulations of a curved beam undergoing snap-through. Various time integrators and element types and formulations are used. A summary of our findings is presented in the concluding section.

2. Representative structure

The representative system discussed in this paper is a curved beam that undergoes snap-through under a concentrated load. The geometry of the beam is shown in Fig. 2. The beam is symmetrical with an angle $\theta = 5.674^\circ$ at the supports. The thicker lines in the figure represent the parts of the beam that are clamped; their horizontal length is L_c . The free portion of the beam has a horizontal projection L_h . The total horizontal projection of the beam, including the clamped parts is $L = 362.204$ mm. The beam can be considered as a thin beam and has a rectangular cross section with depth d much larger than the thickness t . Fig. 3 shows the 3D representation of the beam.

The dimensions of the beam are listed in Table 1 and Table 2 lists the material properties of the structure. Without loss of generality, the type of load used throughout this paper is a point load applied at the center of the beam.

3. Static analysis

In this section we study the effect of the type of elements and formulations on the accuracy of the results in quasistatic simulations. Based on these preliminary results, the options that are less accurate in the static analysis are eliminated, and as a result a decision regarding the best elements to be used in the dynamic analysis can be made.

All simulations presented later in this paper are performed with meshes that ensure spatial convergence. Fig. 4 shows a mesh

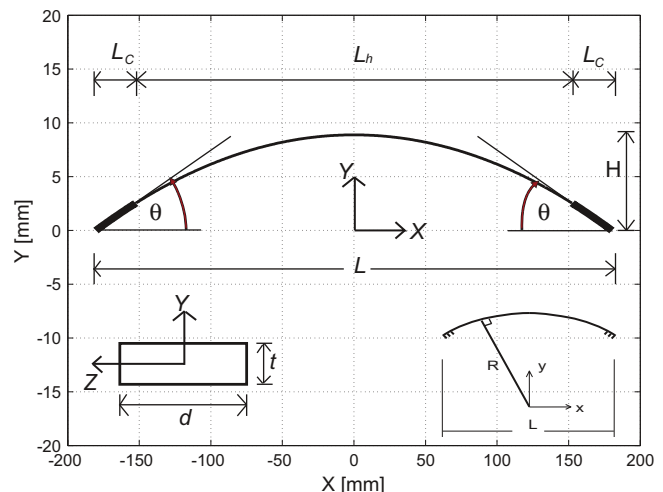


Fig. 2. Geometry of the structure. A curved beam clamped at the supports.

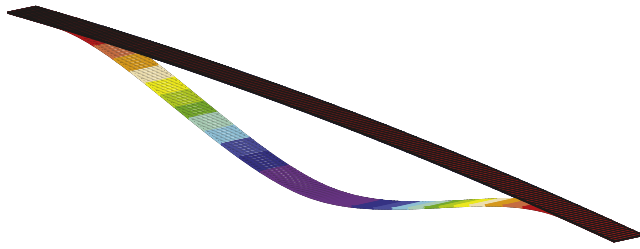


Fig. 3. 3D representation of the geometry of the structure (undeformed and post-snap configurations).

Table 1
Normalized dimensions of the curved beam.

Normalized dimensions	Values
Bottom radius/ L	5.058
Free horizontal length (L_h)/ L	0.8415
Clamp horizontal length (L_c)/ L	0.07925
Depth (d)/ L	0.035
Thickness (t)/ L	0.0014
Rise-to-thickness (H/t)	17.67

Table 2
Material properties.

Properties	Values
Young's modulus (N/mm^2)	206,843
Poisson's ratio	0.28
Density ($\text{N s}^2/\text{mm}^4$)	7.83×10^{-9}

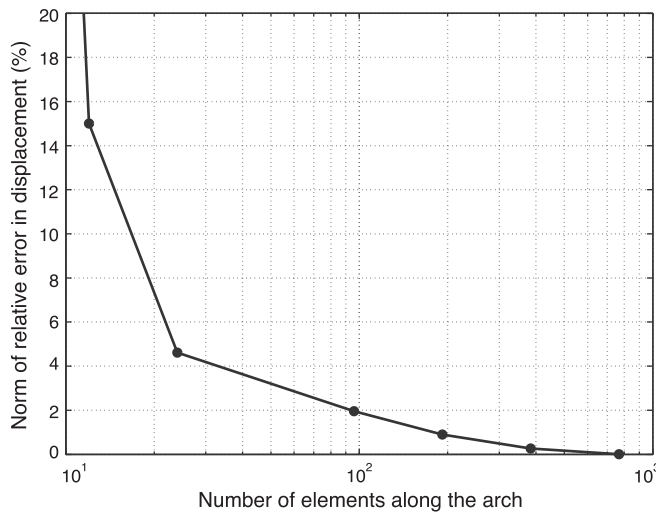


Fig. 4. Mesh refinement study for 3D solid quadratic elements.

convergence study for 3D solid quadratic elements (27 nodes). The reference number of elements is taken to be 3072 elements along the arch. The coarsest mesh utilized has 6 elements along the arch and gives a relative error of 98.2% in estimating the displacement after snap-through. Based on this study, we use a mesh of 200 elements along the arch to ensure less than 1% relative error. A similar study was performed for discretization with beam elements [16].

The structure is symmetrical, but since nonsymmetrical configurations after bifurcation exist under certain conditions, all simulations were performed on the full beam.

3.1. Incremental loading using the Newton–Raphson scheme

The first static analysis is performed with a load control algorithm and uses the Newton–Raphson iterative method. An increasing point load is applied at the midspan of the beam.

The load–displacement curves for the static analyses show that the 2D beam elements with and without shear deformation, the 3D solid linear elements with enhanced formulation, and the 3D solid quadratic elements estimate similar snap-through loads (Fig. 5), $P_{crit} = 1.51 \text{ N}$. However, the 3D solid linear elements with displacement and mixed (B-bar) formulations experience locking; enhanced strain formulations can be used instead to avoid this problem while keeping the elements linear, but the use of higher order elements provides the same algorithmic improvement without the added computational burden (the enhanced elements require a static condensation step and inversion in every element) and without the increased storage requirements (additional local variables inside every element). Therefore, the 2D beam elements and 3D solid quadratic (27 nodes) elements will be the elements used in the transient analysis. Note that there is no warping observed in the simulation that uses 3D solid quadratic elements. Therefore the use of beam elements is acceptable even though they cannot capture warping. Also note that no torsional deformation is observed when the discretization uses 3D solid quadratic elements.

We compared the values of the buckling load and the displacement after buckling obtained from the static analysis with the analytical approximation proposed in Bradford et al. [4]. They have shown that these values provide reasonable approximations for the symmetric buckling of fixed arches. From the comparison, we obtained a relative difference of 4.93% for the buckling load and a relative difference of 5.47% for the displacement after buckling.

Simpler models (link systems) were also used for qualitative comparisons [17] and an extensive investigation of the post snap-through behavior of the curved beam including identification of solutions with non-symmetric deformation response and transient responses under a variety of forcing patterns is presented in [18].

3.2. Hysteresis analysis

The hysteresis analysis illustrates the path-dependence behavior. The structure is loaded with a concentrated force (at the middle of the beam) increased up to a value slightly larger than the snap-through value and then it is unloaded with the same rate. The results under a load controlled scenario confirm that the

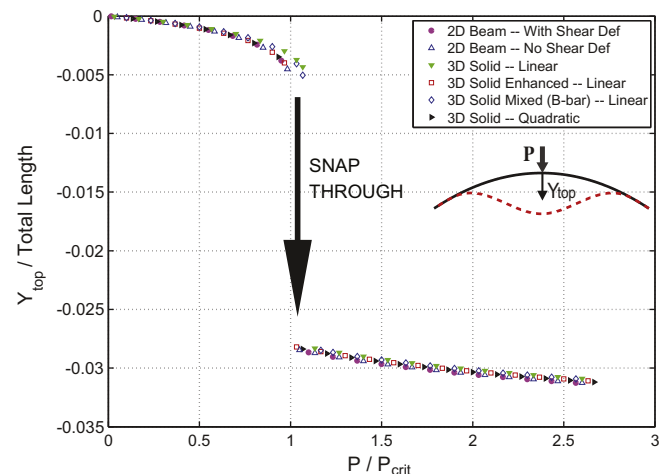


Fig. 5. Load–displacement curve from static analysis with Newton–Raphson.

structure experiences hysteresis causing the equilibrium path to be dependent on the history (Fig. 6).

3.3. Path following analysis using an arclength method

In order to obtain the whole equilibrium path, including the unstable configurations, an arclength algorithm based on Schweizerhof and Wriggers [19] is used. The method controls neither the load nor the displacement but traces the equilibrium configurations, both stable and unstable (Fig. 7), with increments in the length of an arc on this curve. Even though unstable paths are hard to capture experimentally, having access to the whole solution space provides significant insight into the system behavior. If incremental loading is used, the system advances to point 1 then snaps through to point 2. If the load is increased, it will travel to point 3. When the unloading starts, the system will travel back from point 3 to point 2 then to point 4 before snapping back to point 5 and then returning to the original (undeformed) position.

Static analyses provide some information, such as the load level at which snap-through and snap-back occur for specific material properties and geometry. However, a dynamic analysis is required to capture the transient behavior after the snap-through occurs.

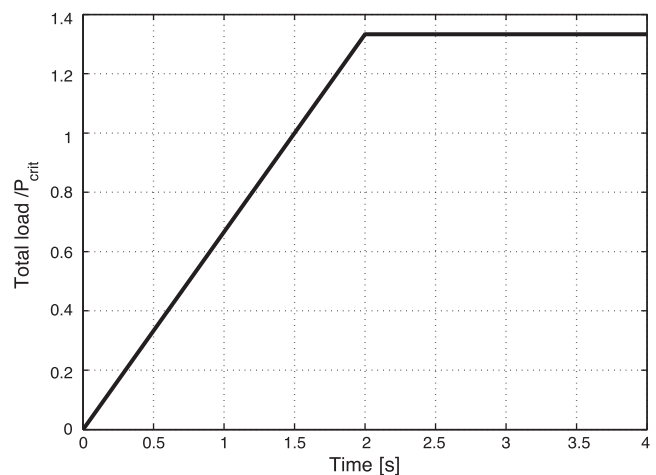


Fig. 8. Load for transient analysis.

4. Transient analysis

This section analyzes the performance of time integrators when applied to transient problems involving snap-through, i.e., the dynamic jump of the system from a “quasi static” configuration to oscillations about a remote equilibrium configuration.

The concentrated force applied at the midspan of the curved beam ramps-up to some value above the snap-through load and then remains constant (Fig. 8).

In the following simulations, the choice of finite elements used to discretize the system is based on the preliminary results of the previous section: 2D beam elements with and without shear deformation and 3D solid quadratic (27 nodes) elements.¹

Due to the snap-through phenomenon, the structure undergoes changes in the stability behavior. The study of the accuracy and robustness of the numerical methods for transient simulations of structures that are likely to traverse unstable regimes raises the following issues: (1) the existence of a critical time step for the stability of the numerical integrator, (2) the introduction of unwanted artificial numerical damping, and (3) the lack of exact energy conservation and other numerical pathologies. These issues are discussed in detail in the rest of this section.

To quantify the robustness of the numerical method, one of the measures used is the total energy. The values of the algorithmic parameters utilized for the Newmark and the energy–momentum schemes ensure energy conservation for linear problems. We will use the deviation from this norm as a measure of the loss of numerical robustness and of the increase in the likelihood of the numerical nature of the instability (if instability is encountered).

4.1. Critical time step

We first present the numerical studies performed in order to identify the critical time steps for both the Newmark method and the conserving A algorithm for different finite element formulations (2D beams and 3D solids). The critical time steps are identified by systematic numerical experimentations. We also present simulation results obtained using the conserving B algorithm, where we will show that there is no critical time step (the simulation does not “blow up”) but accurate results can be obtained only for small time steps.

Simulations with 2D beam elements without shear may converge even for Δt larger than the critical time step. However, for each Δt , a different structural behavior is identified. This

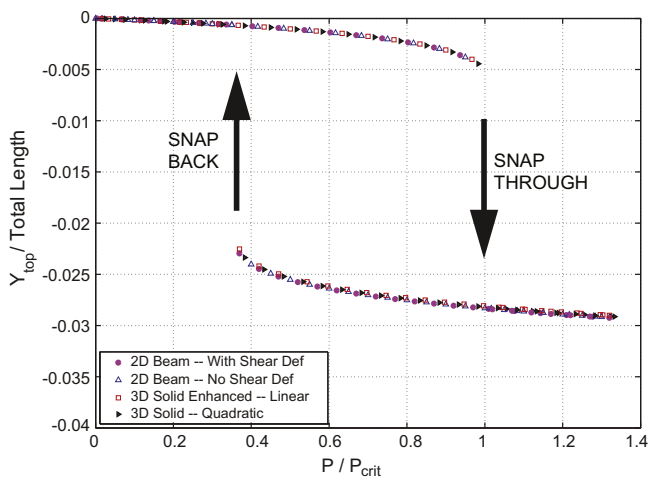


Fig. 6. Load–displacement curve from hysteresis analysis.

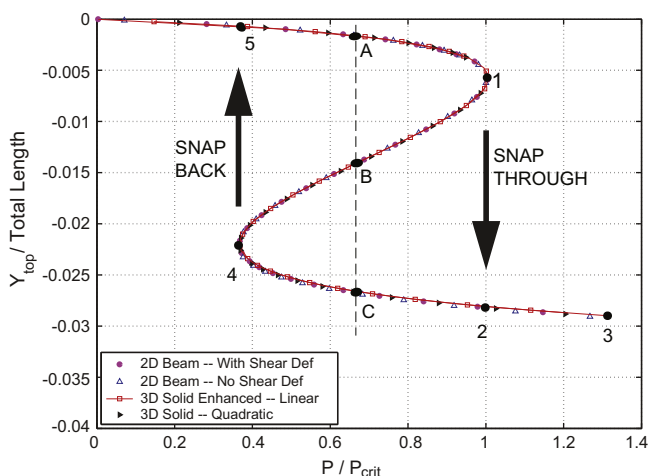


Fig. 7. Load–displacement curve from static analysis with arclength method.

¹ All elements account for large deformation.

observation clearly suggests that even though the nonlinear solver converges, this is not necessarily a solution of the physical system but rather a numerical artifact. An example of such unstable solution ($\Delta t = 10^{-2}$ s) suggests that the structure undergoes intermittent snap-through before it settles into periodic oscillations around an intermediate point that is neither the original configuration nor the snap-through configuration (Fig. 9(a)). The total energy plot for this simulation shows that the energy is not conserved; it increases significantly when the response settles into oscillations about this intermediate configuration (Fig. 9(b)).

The simulations using the 2D beam elements without shear deformations are repeated with the conserving A algorithm (Fig. 10(a)). The energy plot for an unstable time step also shows that the energy increases rapidly at a certain point in the simulation that corresponds to the time increment where the response becomes unphysical (Fig. 10(b)). The total energy obtained in simulations that converge to nonphysical solutions is much larger when the conserving A scheme is used than when using the Newmark method. This makes the identification of the unphysical solutions much easier.

The result of a stable simulation shows that the structure experiences periodic oscillations, which begin right after snap-through occurs (Fig. 11(a)). Even though a stable numerical behavior is exhibited, we observe that the numerical analysis provides a damped response. This response is obtained from the Newmark method with a combination of parameters that should have precluded numerical dissipation, so clearly this damping is a numerical artifact, as will be discussed in more detail in the next subsection.

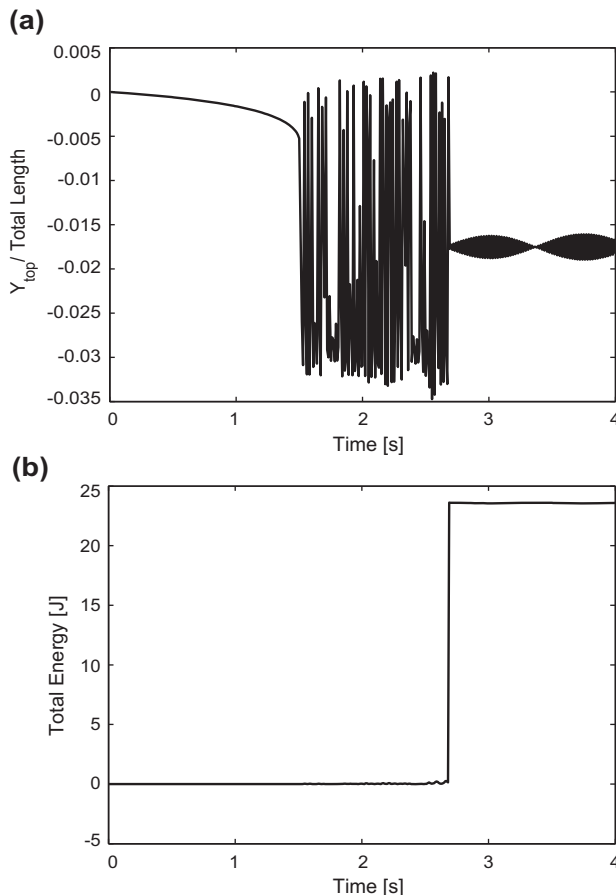


Fig. 9. 2D beam without shear deformation; Newmark method; $\Delta t = 10^{-2}$ s (a) displacement, (b) total energy.

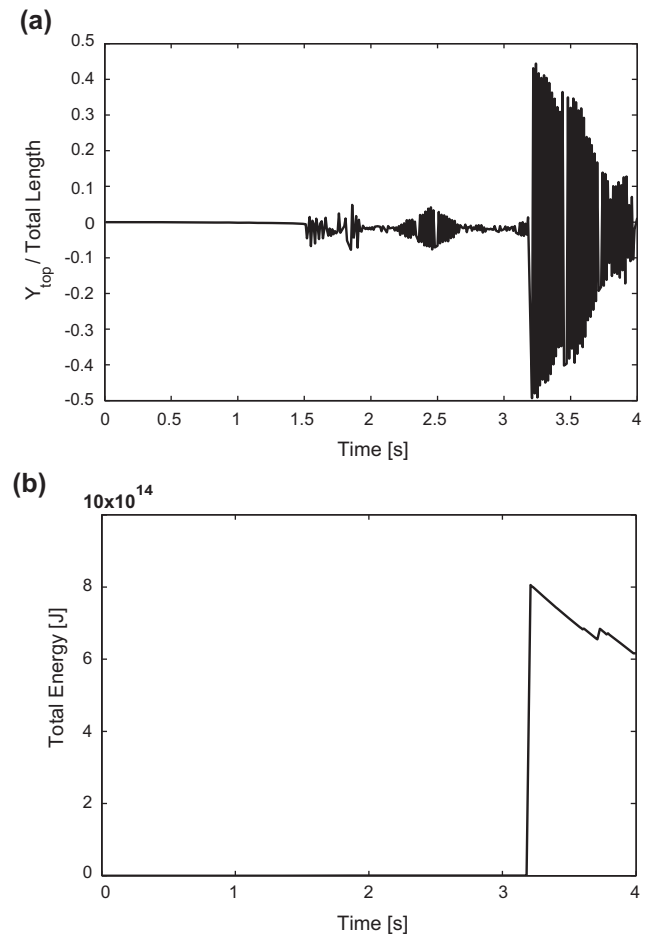


Fig. 10. 2D beam without shear deformation; conserving A scheme; $\Delta t = 10^{-2}$ s (a) displacement, (b) total energy.

The transient simulation performed with 3D solid quadratic elements and a stable time step shows periodic oscillations in the post-snap response of the structure; the amplitude of oscillations stays constant in the region of constant load (Fig. 11(b)), not showing the dissipation that appears when the 2D beam elements without shear deformation are used in the simulation.

The critical time step obtained from systematic numerical experimentations is summarized in Table 3. The preceding study shows that the critical time step depends on the type of elements used to discretize the structure. Studies performed using other loading patterns show that these bounds also depend on the load pattern used (results are not shown here).

Simulations performed using the conserving B scheme [20] are numerically stable at large time steps. However, this scheme introduces numerical damping, which affects the accuracy of the solutions greatly when a large time step is used (Fig. 12(a)). When small time steps are used (Fig. 12(b)), the solution matches the results obtained using the Newmark method and the conserving A algorithm.

4.2. Unwanted artificial numerical damping

The discussion presented in the previous section shows that the 2D beam element without shear deformation introduces artificial numerical dissipation in the transient analysis of structures undergoing changes in stability for time steps smaller than the Δt_{cr} . This behavior is observed even though the algorithm used is supposed to conserve energy, which suggests that there exists some

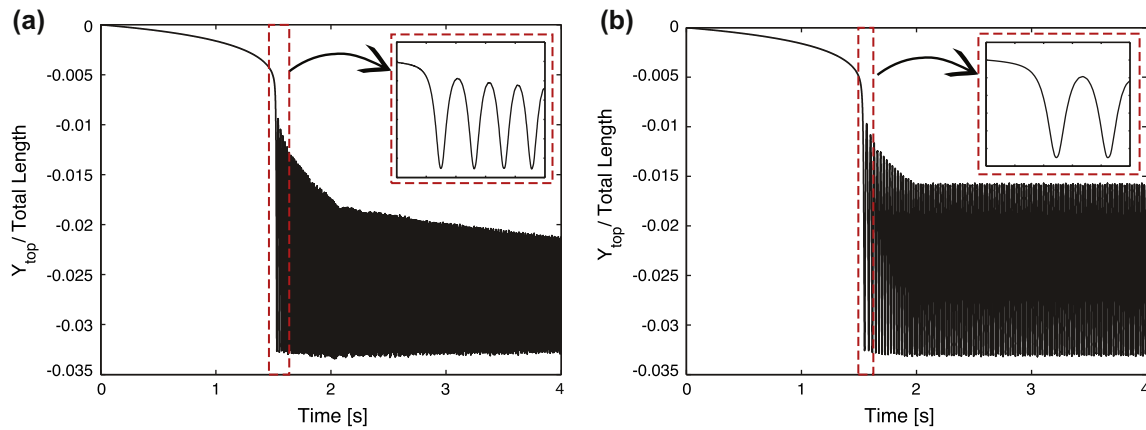


Fig. 11. Displacement vs. time; Newmark method (a) 2D beam with no shear ($\Delta t = 5 \cdot 10^{-5}$ s), (b) 3D solid quadratic ($\Delta t = 10^{-4}$ s).

Table 3
Bounds of the critical time step for different finite elements.

Element type and formulation	Critical time step
2D beam element with shear deformation	$\Delta t_{cr} \approx 10^{-4}$ s
2D beam element without shear deformation	$\Delta t_{cr} \approx 5 \cdot 10^{-5}$ s
3D solid quadratic (27 nodes) element	$\Delta t_{cr} \approx 10^{-4}$ s

correlation between the kinematic assumptions built into a “structural” finite element and the numerical stability and conservation properties in the transient simulation when the problem is highly nonlinear. (Note that the energy conservation property is proven to hold in the discretized system for linear problems, but does not hold for nonlinear problems.)

The transient analyses using 2D beam elements without shear deformation exhibit more numerical damping for smaller time steps for both the Newmark method and the conserving A algorithm (Fig. 13). The responses obtained with the Newmark method show more dissipation than those obtained with the conserving A scheme. Therefore, in addition to the time step size, the amount of dissipation also depends on the time integrator used in the analysis. The relationship between dissipation and $\log \Delta t$ is approximately linear (Fig. 13 with log scale representation on the horizontal axis). The dissipation might be due to the fact that the use of no-shear beam formulations for dynamic problems leads to a discretized system that is parabolic and consequently inadequate for wave

propagation studies [21]. It is therefore expected that the Newmark method that is designed for hyperbolic and hyperbolic-parabolic problems may encounter difficulties in the parabolic case.

To isolate the possible cause of the artificial numerical damping in analyses with 2D beam elements with shear deformation, simulation of one other transient problem is performed; a curved cantilever beam, essentially representing half of the representative structure described in Fig. 2 that has the same properties and is loaded at the free end with a concentrated force increased in the first two seconds and then decreased to zero rapidly (Fig. 14). Notice that snap-through is not exhibited here, reducing the problem to nonlinear deformation/vibration only. In this problem, the beam is discretized with 2D beam elements (with and without shear deformation).

When the beam is discretized with 2D beam elements without shear deformation, damping is also present in the case of the curved cantilever beam. However, the damping is only noticeable when the simulation time is long. Therefore, we can conclude that snap-through aggravates the amount of the damping.

Comparison of the responses for $\Delta t = 10^{-4}$ s obtained with 2D beam elements with and without shear deformation shows that the beam element with small rotation assumption and no shear is clearly more rigid than the beam element with large rotation and shear, both in the initial quasi-static loading phase and in the amplitudes of the oscillations in the transient regime (Fig. 15). Since the beam is very thin and flexible, the inclusion of

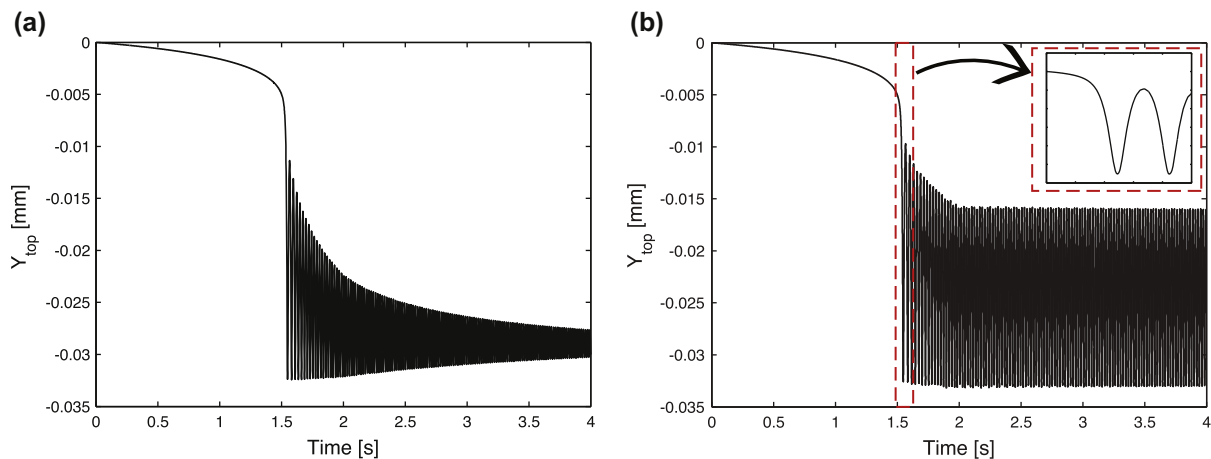


Fig. 12. Displacement vs. time; 3D solid quadratic; conserving B method (a) $\Delta t = 10^{-3}$ s, (b) $\Delta t = 10^{-4}$ s.

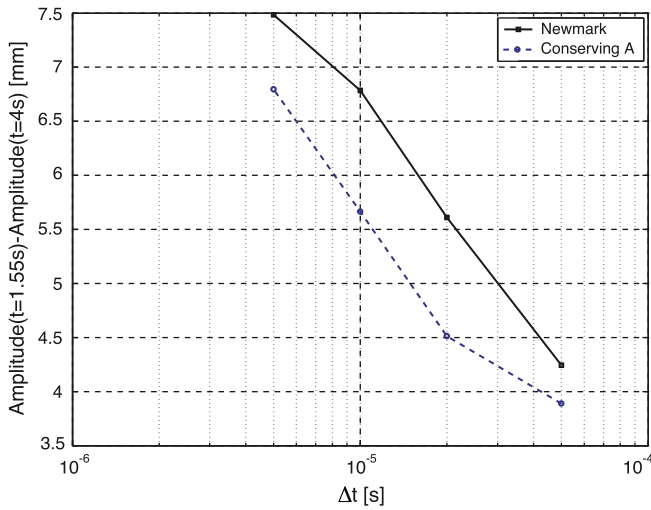


Fig. 13. Decrease in amplitude in the simulations using 2D beam elements without shear deformation.

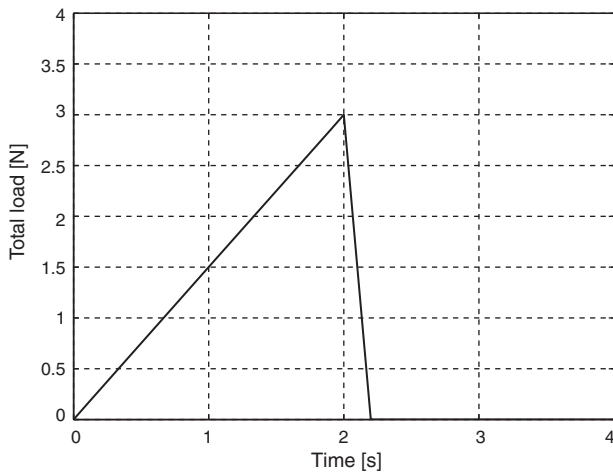


Fig. 14. Load for transient analysis of the curved cantilever beam.

the shear effects should not bring significant changes to the results and we suspect that the cause of this more rigid behavior is the limiting assumption of small rotation.

4.3. Algorithmic conservation of energy

In addition to the existence of a critical time step and the introduction of artificial numerical damping, the transient analysis of a curved beam experiencing snap-through also raises several issues concerning the conservation of energy of the system.

The analysis using 2D beam elements shows that the energy conservation is not satisfied throughout the simulation. The total energy plot for 2D beam elements without shear deformation shows that the total energy is significantly larger (Fig. 16(a)) than the total energy in the analysis with 3D solid quadratic elements (Fig. 16(b)). The total energy includes the kinetic energy, strain energy, and the work applied. Under the energy conservation measure, the conserving A algorithm performs better than the Newmark method. Simulations performed using the conserving B algorithm clearly do not satisfy the conservation of energy; artificial numerical damping is introduced into the system [20]; the larger the time step, the larger the decrease in energy (Fig. 17).

Pathologies in the variation of energy also appear when 2D beam elements with shear deformation are used for the spatial discretization of the system. The results obtained from analyses performed with the Newmark method ($\Delta t = 10^{-4}$ s) for a system discretized with 2D beam elements with shear deformation show that the refinement of the mesh increases the energy of the system (Fig. 18). Note that the energy does not change when a smaller time step is used, showing that the increase in energy depends only on the mesh refinement.

Further examination shows that as the mesh is refined, it is the kinetic energy that changes significantly in magnitude while the strain energy remains the same. This phenomenon is observed only when the 2D beam elements with shear deformation capabilities are used in the analysis. The analyses using 2D beam elements without shear deformation and 3D solid quadratic elements show no dependence of the kinetic energy on the level of mesh refinement.

Several attempts were made to understand this behavior. A closed-form solution based on the assumptions of negligible displacement in the X direction and small rotation shows that the kinetic energy for one element with length h and two elements with length $h/2$ in one time step is the same, but once again, such results no longer hold for large deformation [16].

Simulations performed on the curved cantilever beam used in the previous subsection examined whether the increase in energy appears in other transient problems solved with 2D beam elements with shear deformation capabilities. Recall that this formulation also accounts for large deformation and large rotation. The geometry represents half of the representative structure described in

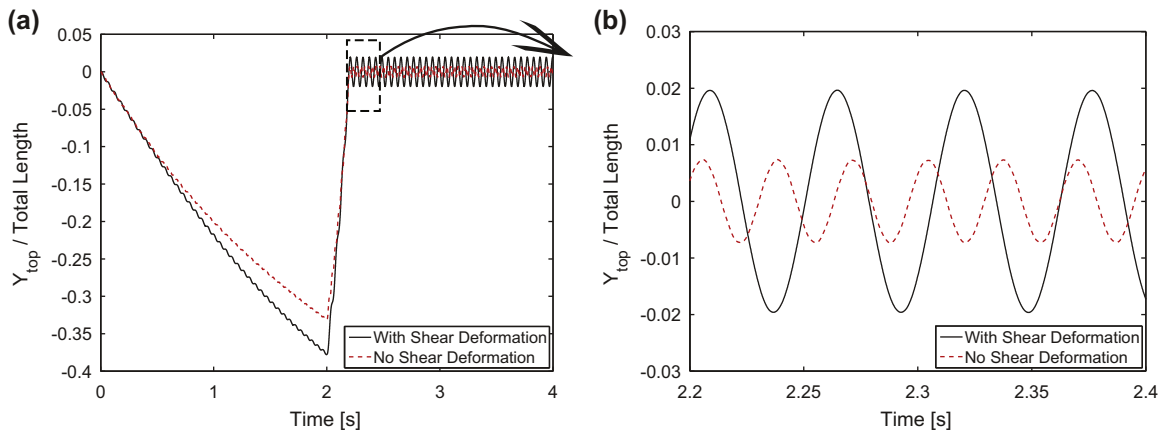


Fig. 15. Curved cantilever beam; Newmark; $\Delta t = 10^{-4}$ s; various 2D beam elements (a) displacement vs. time, (b) zoom in.

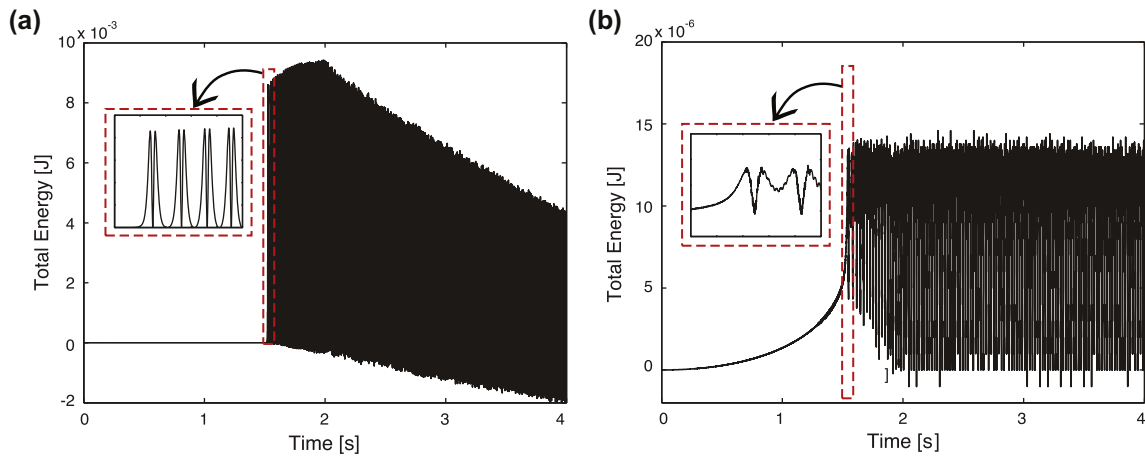


Fig. 16. Total energy vs. time; Newmark method (a) 2D beam with no shear ($\Delta t = 5 \cdot 10^{-5}$ s), (b) 3D solid quadratic ($\Delta t = 10^{-4}$ s).

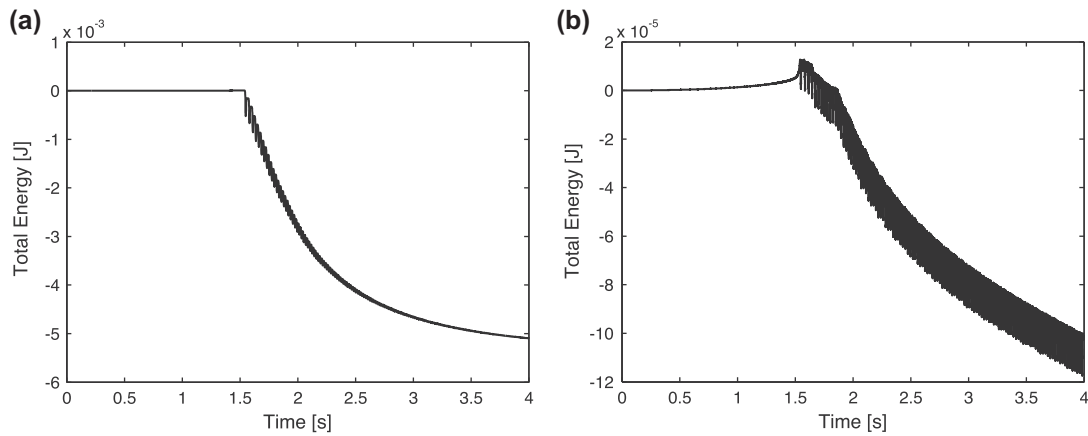


Fig. 17. Total energy vs. time; 3D solid quadratic; conserving B method (a) $\Delta t = 10^{-3}$ s, (b) $\Delta t = 10^{-4}$ s.

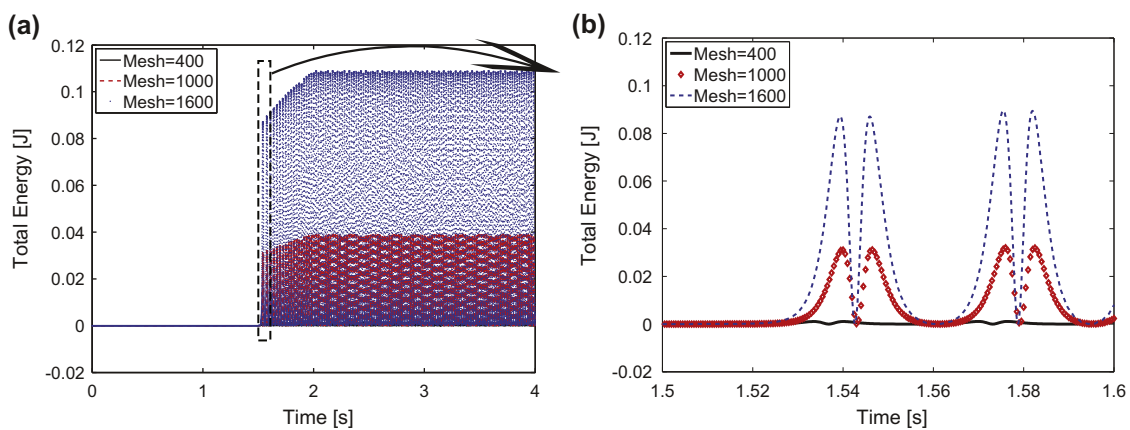


Fig. 18. Arch fixed at both ends; 2D beam with shear; Newmark method; $\Delta t = 10^{-4}$ s; various meshes (a) total energy vs. time, (b) zoom in.

Fig. 2 and the loading is shown in Fig. 14. The kinetic energy plots show that there is an increase in the kinetic energy when the mesh is refined (Fig. 19) for this case as well. Therefore, we can conclude that the dependency of the kinetic energy on the mesh refinement is a feature of the 2D beam with shear elements and not necessarily induced by the type of the problem (e.g., snap-through).

5. Conclusions

This paper analyzes the performance of several finite element formulations (2D and 3D) and the stability of the time-stepping schemes in simulating a curved beam undergoing snap-through by identifying the important features that affect the numerical

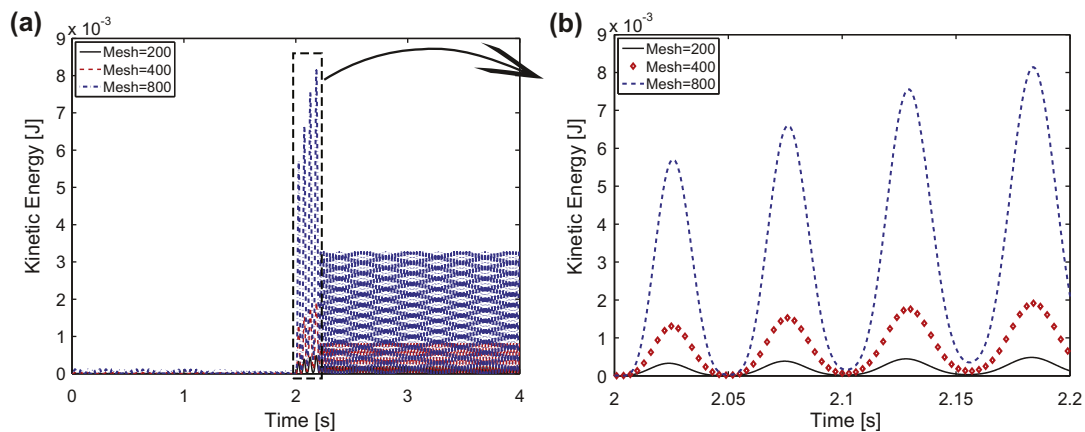


Fig. 19. Curved cantilever beam; Newmark; 2D with shear; $\Delta t = 10^{-4}$ s; various meshes (a) kinetic energy vs. time, (b) zoom in.

accuracy and robustness and the region where the schemes are stable for such simulations. We examine the interaction between the two most important components of the finite element analysis applied to structural dynamics problems: (1) the time-stepping schemes and (2) the finite element formulations used to spatially discretize the structure. The integrators studied are (1) the Newmark method, (2) a conserving integrator (referred as conserving A) [10–12], and (3) a composite integrator (referred as conserving B) proposed by Bathe [13]. The finite element formulations used are the 2D beam elements with and without shear deformation capabilities and the 3D solid elements.

The study shows that the Newmark method and the conserving A scheme have a restrictive bound on the size of the time step to ensure numerical stability. The critical time step depends on the finite element formulations used to discretize the structure and on the loading pattern. Simulations performed using the conserving B algorithm do not have this restriction. However the numerical damping introduced by this algorithm increases with the increase in the time step and greatly affects the accuracy of the solution when large time steps are used.

The study also shows that the spatial and temporal discretizations may interact and such interactions may induce unwanted numerical effects such as artificial damping, lack of energy conservation, and most importantly, misleading numerical results that seem to indicate a chaotic response when in fact the simulation simply converged to non-physical solutions. These issues are very severe when structural elements are used to discretize the beam while the use of 3D solid elements has less severe effects. Therefore, we recommend the use of 3D solid elements in solving snap-through problems.

Due to the nonlinearity of the problem, the conservation of energy is sometimes lost when structural elements (e.g., beams) introduce kinematic assumptions in the discretization of the structure. The total energy is approximately conserved when 3D solid quadratic elements are used with the Newmark method and conserving A algorithm. When the conserving B algorithm is used, the conservation of energy is not satisfied because numerical damping is introduced to the system. The inspection of energy plots for the analyses performed with beam formulation with shear deformation also shows another numerical artifact: the kinetic energy is mesh dependent (increases as the number of elements increases; reducing the time step does not eliminate this unwanted behavior).

In conclusion, we have shown that several of the currently available finite element formulations are not robust or accurate enough to simulate snap-through. In particular, assumptions

built into the formulation of structural elements (e.g., beam elements) lead to unwanted numerical behavior that is often times amplified by the presence of the snap-through phenomenon in the system.

Acknowledgements

The authors would like to thank Professor Lawrence Virgin (Duke University) for his valuable comments and suggestions.

The work has been funded in part by AFOSR under the Grant No. FA9550-09-1-0201. This support is greatly appreciated.

References

- [1] Jennings A. Structures: from theory to practice. Spon Press; 2004, ISBN 978-0415268431.
- [2] Murphy K, Virgin L, Rizzi S. Experimental snap-through boundaries for acoustically excited, thermally buckled plates. *Exp Mech* 1996;36:312–7.
- [3] Virgin LN. Vibration of axially loaded structures. 1st ed. Cambridge University Press; 2007, ISBN 978-0521880428.
- [4] Bradford MA, Uy B, Pi YL. In-plane elastic stability of arches under a central concentrated load. *J Eng Mech ASCE* 2002;128(7):710–9.
- [5] Plaut R, Virgin L. Vibration and snap-through of bent elastica strips subjected to end rotations. *J Appl Mech Trans ASME*, 00218936 2009;76(4):1–7. URL: Available from: <<http://dx.doi.org/10.1115/1.3086783>>.
- [6] Pecknold D, Ghaboussi J, Healey T. Snap-through and bifurcation in a simple structure. *J Eng Mech ASCE* 1985;111:902–22.
- [7] Taylor RL. FEAP a finite element analysis program. Version 8.3 user manual ed. Berkeley, California: Department of Civil and Environmental Engineering, University of California at Berkeley; 2011.
- [8] Newmark N. A method of computation for structural dynamics. *J Eng Mech ASCE* 1959;85:67–94.
- [9] Armero F, Romero I. On the formulation of high-frequency dissipative time-stepping algorithms for nonlinear dynamics. Part I: low-order methods for two model problems and nonlinear elastodynamics. *Comput Methods Appl Mech Eng* 2001;190(20–21):2603–49.
- [10] Simo J, Tarnow N. The discrete energy-momentum method. Conserving algorithms for nonlinear elastodynamics. *Z Angew Math Phys* 1992;43(5):757–92.
- [11] Simo J, Tarnow N, Wong K. Exact energy-momentum conserving algorithms and symplectic schemes for nonlinear dynamics. *Comput Methods Appl Mech Eng* 1992;100(1):63–116.
- [12] Gonzalez O. Design and analysis of conserving integrators for nonlinear Hamiltonian systems with symmetry. Ph.D. thesis. Stanford University; 1996.
- [13] Bathe K-J. Conserving energy and momentum in nonlinear dynamics: a simple implicit time integration scheme. *Comput Struct* 2007;85(7–8):437–45.
- [14] Kuhl D, Crisfield M. Energy-conserving and decaying algorithms in non-linear structural dynamics. *Int J Numer Methods Eng* 1999;45(5):569–99.
- [15] Garikipati K, Arruda EM, Grosh K, Narayanan H, Calve S. A continuum treatment of growth in biological tissue: the coupling of mass transport and mechanics. *J Mech Phys Solids* 2004;52(7):1595–625.
- [16] Chandra Y. Snap through of curved beam. Master thesis. University of Illinois at Urbana-Champaign; 2009.

- [17] Wiebe R, Virgin LN, Stanciulescu I, Spottswood S. On snap-through buckling. In: Collection of technical papers – AIAA/ASME/ASCE/AHS/ASC structures, structural dynamics and materials conference, Denver, Colorado; 2011.
- [18] Stanciulescu I, Chandra Y, Eason T. Boundaries of snap-through buckling of curved beams. In: Collection of technical papers – AIAA/ASME/ASCE/AHS/ASC structures, structural dynamics and materials conference, Denver, Colorado; 2011.
- [19] Schweizerhof K, Wriggers P. Consistent linearization for path following methods in nonlinear FE analysis. *Comput Methods Appl Mech Eng* 1986;59(3):261–79.
- [20] Bathe K-J, Baig MML. On a composite implicit time integration procedure for nonlinear dynamics. *Comput Struct* 2005;83:2513–24.
- [21] Felippa CA. Class notes: introduction to finite element methods, <<http://www.colorado.edu/engineering/CAS/courses.d/IFEM.d/Home.html>>; 2009.